

**EXAMINATION OF BONDING BETWEEN
SUCCESSIVE LIFTS OF CONCRETES HAVING
DIFFERENT THIXOTROPY LEVELS BY
SURFACE SCANNING**

**A Thesis Submitted to
the Graduate School of
İzmir Institute of Technology
in Partial Fulfilment of the Requirements for the Degree of**

**DOCTOR OF PHILOSOPHY
in Civil Engineering**

**by
Hasan Yavuz ERSÖZ**

**December 2020
İZMİR**

ACKNOWLEDGEMENTS

I would like to say my gratitude to all those who gave me the possibility to complete this thesis. I wish to thank my advisor, Assoc. Prof. Dr. Tahir Kemal Erdem for his support, guide, and assistance. I also want to thank Prof. Dr. Ali Topal, Assoc. Prof. Dr. Şevket Gümüştekin and Mehmet Çalı for all their assistance on digital image processing and computer vision.

The members of the thesis monitoring committee, Assoc. Prof. Dr. Engin Aktaş and Prof. Dr. Ali Topal also helped with their valuable recommendations and reviews.

A special thanks to Prof. Dr. Mustafa Şahmaran and Asst. Prof. Dr. Selçuk Saatçı for their contribution during the thesis defense exam as jury members.

Many thanks to Yakup Şanal, Muhammed Mustafa Özer and Cemal Kılıç for their great support for experiments at the laboratory. I appreciate the help from ÇİMSA cement factory in Mersin and IZTECH Center For Materials for the determination of the cement properties.

Especially, I would like to give my special thanks to my family for their great support during this long duration of study.

ABSTRACT

EXAMINATION OF BONDING BETWEEN SUCCESSIVE LIFTS OF CONCRETES HAVING DIFFERENT THIXOTROPY LEVELS BY SURFACE SCANNING

Unexpected delays in casting can result in strength losses and should be examined considering the thixotropy of the concrete. The effects of thixotropy and delays in casting (0, 45, and 90 min) on concrete bonding strength and on the surface properties were examined. Firstly, 15 self-consolidating concretes (SCC) having different compositions with three different water/cement ratios (0.36, 0.41 and 0.46) three different fine/all aggregate ratios (0.45, 0.50 and 0.55) and two slump flow diameters (60 cm and 70 cm) were produced. Slump flow, visual stability index, T50, V-funnel, static sieve segregation, rheology, and thixotropy tests were carried out on fresh concrete. Considering the results obtained so far, three mixtures were selected to have high, low, and moderate thixotropy for subsequent tests on hardened concrete specimens. Five different roughening patterns were applied on the concrete specimens' interlayer zones by using wooden frames. Slant shear, bi-surface shear, and pull-off tests were conducted on the cylindrical, cubic and drilled specimens to assess bond strength, respectively. Slant shear test gave the highest bonding test results. The lowest results were obtained for the pull-off test. Lateral surfaces of the specimens were scanned with two different lenses. 2D and 3D scanning procedures were adapted with those lenses. Pattern and thixotropy effect was investigated. Lowest void area was obtained for high thixotropy. Highest compressive strengths were obtained for mid thixotropy and high thixotropy for slant shear and pull-off tests respectively. Image J and Matlab were used to analyze images of the surfaces. Ultrasonic pulse velocity test was conducted on all specimens, moderate thixotropy gave the highest results for Ultrasonic Pulse Velocity test.

ÖZET

FARKLI TİKSOTROPIYE SAHİP BETONLARIN ARDIŞIK TABAKALAR HALİNDE DÖKÜLMESİ SONUCU OLUŞAN ADERANSIN YÜZEY TARAMA İLE BELİRLENMESİ

Betonun dökülmesi sırasında meydana gelen beklenmeyen duraksamalar mukavemet kayıplarına neden olabilir ve betonun tiksotropisi dikkate alınarak incelenmelidir. Tiksotropi ve dökümdeki gecikmelerin (0, 45 ve 90 dk) beton bağ kuvvetine ve yüzey özelliklerine etkileri incelenmiştir. Öncelikle, üç farklı su / çimento oranı (0,36, 0,41 ve 0,46), üç farklı ince agrega/ toplam agrega oranı (0,45 0,50 ve 0,55) ve iki farklı yayılma çapı (60 cm ve 70 cm) ile 15 çeşit kendiliğinden yerleşen beton (KYB) üretildi. Taze beton üzerinde yayılma çapı, görsel stabilite indeksi, T50, V-hunisi, elek segregasyon deneyi, reoloji ve tiksotropi testleri yapılmıştır. Şimdiye kadar elde edilen sonuçlar dikkate alınarak, sertleşmiş beton testleri için yüksek, düşük ve orta tiksotropiye sahip üç karışım seçilmiştir. Beton numunelerin ara katman bölgelerine ahşap şekiller kullanılarak beş farklı pürüzlendirme deseni uygulanmıştır. Bağ kuvvetini değerlendirmek için sırasıyla silindirik, kübik ve kısmi delinmiş numuneler üzerinde eğimli kesme, çift yüzeyli kesme ve (kabuk) çekme testleri yapılmıştır. Eğimli kesme testi, en yüksek bağ kuvveti testi sonuçlarını vermiştir. En düşük sonuçlar çekme testi için elde edildi. Örneklerin yan yüzeyleri iki farklı lens ile tarandı. Bu lenslerle 2D ve 3D tarama prosedürleri uyarlandı. Ara yüzeye uygulanan şekillerin ve tiksotropinin etkisi araştırıldı. Testlerde en düşük boşluk alanı yüksek tiksotropi için elde edilmiştir. En yüksek basınç dayanımı eğimli kesme metodu için orta tiksotropi ile ve (kabuk) çekme testi için yüksek tiksotropi ile elde edilmiştir. Yüzeylerin görüntülerini analiz etmek için Image J ve Matlab kullanıldı. Tüm örneklerde ultrasonik test cihazı ile ölçüm yapıldı, orta tiksotropi ile üretilen numunelerde UPV için en yüksek sonuçlar elde edildi.

TABLE OF CONTENTS

LIST OF FIGURES	ix
LIST OF TABLES	xiii
CHAPTER 1. INTRODUCTION	1
1.1. Objective	1
1.2. Scope.....	1
CHAPTER 2. GENERAL INFORMATION.....	3
2.1. Self-consolidating Concrete.....	3
2.2. Delays in Casting.....	3
2.3. Rheology of SCC.....	5
2.4. Thixotropy of SCC.....	5
2.5. Superplasticizers	7
2.6. SCC Interlayer Bonding.....	8
2.7. Air Void Characteristics of Hardened Concrete	8
2.8. Digital Image Processing and Applications.....	9
2.9. Theory of Image Acquisition.....	11
2.10. Enhancement and Segmentation of the Images	12
2.11. Previous Studies	14
CHAPTER 3. TEST METHODS AND EXPERIMENTAL PROGRAM	20
3.1. Materials	23
3.1.1. Cement.....	23
3.1.2. Aggregate	23
3.1.2.1. Sieve Analysis	24
3.1.2.2. Bulk Density.....	25
3.1.2.3. Specific Gravity and Absorption Capacity.....	25
3.1.2.4. Void Content of Fine and Coarse aggregate.....	26
3.1.3. Superplasticizer	26

3.2. Test Methods for Fresh SCC.....	27
3.2.1. Slump Flow Test and T50	27
3.2.2. Visual Stability Index (VSI).....	28
3.2.3. V-Funnel Test.....	29
3.2.4. Sieve Segregation Resistance Test.....	29
3.2.5. Setting Time of Concrete	30
3.2.6. Rheology	31
3.2.7. Thixotropy.....	33
3.3. Test Methods for Hardened SCC	35
3.3.1. Image Processing & Analysing	35
3.3.1.1. Image Acquisition System	35
3.3.1.2. 2D Image Analysis with Image J	37
3.3.1.3. 3D Image Analysis with Matlab.....	42
3.3.2. Bi-surface Shear Test	48
3.3.3. Slant Shear Test.....	48
3.3.4. Ultrasonic Pulse Velocity Test.....	49
3.3.5. Pull-off Testing	52
3.3.6. Compressive Strength	54
3.3.7. Preparation of the specimens.....	54
3.3.8. Surface Properties	58
3.3.9. Surface Scanning Procedure.....	58
 CHAPTER 4. RESULTS AND DISCUSSION.....	 60
4.1. Fresh Concrete Tests	60
4.1.1. V- funnel and T50 Durations	60
4.1.2. VSI	63
4.1.3. Sieve Segregation Resistance.....	64
4.1.4. Thixotropy.....	64
4.1.5. Rheology	68
4.2. Hardened Concrete Tests	71
4.2.1. Compressive Strength	73
4.2.2. Slant Shear.....	76
4.2.3. Bi-surface Shear	78

4.2.4. Pull-off	79
4.2.5. UPV Results	82
4.3. Surface Properties	87
4.3.1. Cubic Specimens	88
4.3.1.1 Area Fraction and Void Count	88
4.3.1.2. Average Area of Ten Largest Points	91
4.3.2. Cylindrical Specimens.....	93
4.3.3. Beam Specimens and Bi-Surface Shear Specimens.....	94
4.3.4. Extracting Volumetric Information	96
 CHAPTER 5. CONCLUSION ..	 99
5.1. Summary	99
5.2. Recommendations.....	101
 REFERENCES	 102
 APPENDICES	
APPENDIX A. 2D SURFACE ANALYSIS EXAMPLES	
IMAGES.....	109
APPENDIX B. 2D IMAGE ANAYLSIS RESULTS	
TABLE OF RESULTS.....	125
APPENDIX C. 3D DEPTH MAP EXAMPLES	
IMAGES.....	133
APPENDIX D. SLANT SHEAR SPECIMEN EXAMPLES	
IMAGES.....	137
APPENDIX E. BI-SURFACE SHEAR SPECIMEN EXAMPLES	
IMAGES.....	139
APPENDIX F. PULL-OFF TEST PHOTOS	
IMAGES.....	140

LIST OF FIGURES

<u>Figure</u>	<u>Page</u>
Figure 2.1 Successive casting problems	4
Figure 2.2 Rheological behaviors	5
Figure 2.3 Behaviour of the cement paste (Roussel, 2006)	6
Figure 2.4 Yield stress behavior of cementitious particle (Roussel, 2006)	7
Figure 2.5 Mechanism of action (Aicha, 2020)	7
Figure 2.6 Stereomicroscope images	8
Figure 2.7 Pixel values of the selected region	10
Figure 2.8 Explanation of acquisition of the images (Jähne, 2005)	11
Figure 2.9 a) Example image, b) Histogram of the image.....	13
Figure 3.1 Workflow.....	22
Figure 3.2 Fuller curve with three ratios of F.A/T.A.....	25
Figure 3.3 Slump Flow Test	27
Figure 3.4 VSI = 2 for the left SCC and VSI = 0 for the right SCC.....	28
Figure 3.5 V-funnel Test (Erdem et. al., 2012).....	29
Figure 3.6 An example for setting time determination	30
Figure 3.7 Contec 4SCC rheometer	31
Figure 3.8 An example rheogram	32
Figure 3.9 Rheometer software.....	32
Figure 3.10 Yield value at rest.....	33
Figure 3.11. Time-dependent change of torque at four different speeds	34
Figure 3.12 Structural breakdown	34
Figure 3.13 Operation illumination and camera controls	36
Figure 3.14 Led lamps	36
Figure 3.15 (Left) 2D macro lens (Right) 3D macro stereo lens	37
Figure 3.16 Different illumination cases as obtained images from 1 to 4	37
Figure 3.16a Different illumination cases as obtained images from 4 to 8	38
Figure 3.17 Illumination from up, down, left, and right (D5MID454).....	38
Figure 3.18 Extracting depth information.....	39
Figure 3.19 Max and min.....	39
Figure 3.20 Binary image for min and max.....	40

<u>Figure</u>	<u>Page</u>
Figure 3.21 Analyze particles	40
Figure 3.22 Summary of Image-j analysis results	41
Figure 3.23 Area labelled voids of binary image.....	41
Figure 3.24 Results window	42
Figure 3.25 Unrectified stereo image for D4LO45 3rd illumination case.....	43
Figure 3.26 Third illumination case left and right view	43
Figure 3.27 Rectified images	44
Figure 3.28 1 st illumination case disparity map (surface of D4LO45)	45
Figure 3.29 Points 3D (surface of D4LO45)	45
Figure 3.30 3D Cavities (for so-called D4LO45 concrete)	46
Figure 3.31 3D background (for so-called D4LO45 concrete).....	46
Figure 3.33 2D depth map (for so-called D4LO45 concrete).....	47
Figure 3.34 Flow chart for Matlab analysis	47
Figure 3.35 Bi-surface Shear loading	48
Figure 3.36 Slant Shear Test.....	49
Figure 3.36 Different cases of pulse transmission (CNS Farnell, n.d.)	50
Figure 3.38 UPV testing (left), transducer positions (right).....	51
Figure 3.39 Partially drilled specimens and locations	52
Figure 3.39 Illustration of Failure Modes (ASTM C1583, 2013)	53
Figure 3.41 Experimental steps	53
Figure 3.42 Applied patterns	54
Figure 3.43 Dimension of patterns in cm	55
Figure 3.44 First layer of the cubic samples (for mid-thixotropy level).....	55
Figure 3.45 Slant Shear specimens	56
Figure 3.46 Bi-surface Shear specimens.....	57
Figure 3.47 (a) beam specimens (b) cylinder specimens.....	59
Figure 3.47 Specimen Scanning Procedure	59
Figure 4.1 Change of V-funnel with w/c and FA/TA for 60 cm slump flow	61
Figure 4.2 Change of V-funnel with w/c and FA/TA for 70 cm slump flow	62
Figure 4.3 Change of T50 with w/c and FA/TA for 60 cm slump flow	62
Figure 4.4 Change of T50 with w/c and FA/TA for 70 cm slump flow	63
Figure 4.5 Change of thixotropy with w/c and FA/TA for 60 cm slump flow.....	65
Figure 4.6 Change of thixotropy with w/c and FA/TA for 70 cm slump flow	65

<u>Figure</u>	<u>Page</u>
Figure 4.7 Box -whisker graph for YVR	67
Figure 4.8 Change of thixotropy with duration (60 cm slump flow).....	67
Figure 4.9 Change of thixotropy with duration (70 cm slump flow).....	68
Figure 4.10 Change of A.Y.S. with w/c and FA/TA for 70 cm slump flow.....	69
Figure 4.11 Change of T.P.V. with w/c and FA/TA for 60 cm slump flow	70
Figure 4.12 Change of T.P.V. with w/c and FA/TA for 70 cm slump flow	71
Figure 4.13 Compressive strength (for low thixotropy)	74
Figure 4.14 Compressive strength (for medium thixotropy)	75
Figure 4.15 Compressive strength (for high thixotropy)	75
Figure 4.16 Slant Shear specimens bond strength change	77
Figure 4.17 Bi-surface shear results	79
Figure 4.18 Pull-off test results.....	80
Figure 4.19 Bonding tests comparison	81
Figure 4.20 UPV results of cubes with patterns for low thixotropy	83
Figure 4.21 UPV results of cubes with patterns for mid thixotropy.....	84
Figure 4.22 UPV results of cubes with patterns for high thixotropy	84
Figure 4.23 UPV results of the beam specimens	85
Figure 4.24 UPV for Cylinder specimens.....	86
Figure 4.25 UPV for Bi-surface Shear specimens	86
Figure 4.26 Relationship between UPV and E for cubic specimens	87
Figure 4.27 Low Level for all patterns	89
Figure 4.28 Mid level for all patterns	90
Figure 4.29 High level for all patterns	90
Figure 4.30 Average of 10 largest void area.....	92
Figure 4.31 Surface analysis results of cylinders	93
Figure 4.32 Results for the beam specimens	94
Figure 4.33 Bi surface shear specimens surface results.....	95
Figure 4.34 Void volume change with the Low thixotropy.....	97
Figure 4.35 Void volume change with the mid thixotropy	98
Figure 4.36 Void volume change with high thixotropy	98

LIST OF TABLES

<u>Table</u>	<u>Page</u>
Table 2.1 Sample operations.....	10
Table 3.1 Mixture proportions	20
Table 3.2 Properties of cement	23
Table 3.3 Sieve analysis results of the aggregates.....	24
Table 3.4 HRWRA properties	26
Table 3.5 VSI values (EFNARC, 2005)	28
Table 3.6 Classification of concrete (Neville, 1995).....	51
Table 3.7 Specimen counts and dimensions	57
Table 4.1 V-funnel and T50 durations.....	60
Table 4.2 VSI values.....	63
Table 4.3 Static Sieve Segregation results.....	64
Table 4.4 Thixotropy values	66
Table 4.5 Rheology test results.....	68
Table 4.6 Compressive strength test results.....	72
Table 4.7 Compressive Strength results (cubic)	73
Table 4.8 Slant Shear results.....	76
Table 4.9 Bi-surface test results.....	78
Table 4.10 Pull-off test results	80
Table 4.11 UPV results (km/s)	82
Table 4.12 Results for average of 10 largest void area.....	92
Table 4.13 Cylinder surface analysis	93
Table 4.14 Volumetric info of the specimens.....	96

CHAPTER 1

INTRODUCTION

1.1. Objective

Delays between layers during fresh concrete casting is an area of interest for the concrete industry. Critical time to prevent the damage due to delays depends on concrete mixture design, placement procedure, weather conditions, and formwork geometry. Moreover, the roughness or the surface properties of the underlying layer affects the interlocking at the interlayer zone.

Self-consolidating concrete (SCC) is a flowable concrete and classifying the surface roughness and determining the time-dependent behavior of concrete are crucial for interlayer properties in relation to specific delays during casting.

Image-based detection of the surface properties is an innovative and indirect way to access information about concrete specimens. Detecting and analyzing a surface line originated from the casting process can be a cheap and a reliable method to estimate the damage and to reduce the repair costs (Megid and Khayat, 2017; Volz et al., 1997).

In this thesis, it is aimed to investigate the interlayer properties of several SCC mixtures having different thixotropy levels and having different surface roughness patterns by several methods such as mechanical tests, non-destructive tests and image analysis of the concrete lateral surfaces.

1.2. Scope

In order to achieve the above-mentioned objectives, 15 different SCC mixtures were designed by varying water-to-cement ratio (w/c), slump flow diameter and aggregate grading. The fresh properties of the mixtures were determined by performing slump flow, t₅₀, V-funnel, segregation resistance, visual stability index (VSI) and rheology tests. Moreover, thixotropy was measured by the method from the literature immediately after mixing, after 45 min resting, and after 90 minute resting. According to

the results of the 15 mixtures; three mixtures with low, medium and high thixotropy were selected for further studies.

With the selected three SCC mixtures, cylinder, cube, and beam specimens were cast monolithically and with 2 layers. In the case of layered casting, the second layer was placed on the underlying layer with 45 minutes or 90 minutes delays. In the case of cubic specimens, wooden frames with different shapes were allowed to rest on the first layer until the casting of the second layer in order to simulate different surface roughness patterns.

In addition to the compressive strength tests on the monolithic and layered specimens, bi-surface shear, slant shear, pull-off and non-destructive tests were applied on the hardened specimens.

Images were captured with an automatically illuminated and running system by using an electrical circuit. Lateral surfaces of the hardened SCC specimens were scanned. For image capturing, two different lenses were used. The images taken by a macro lens were examined with Image-J to take the 2D surface data and a stereo lens was used for a group of cubic specimens produced with different patterns. Matlab was used to construct a 3D point cloud, and volumetric information was obtained.

CHAPTER 2

GENERAL INFORMATION

2.1. Self-consolidating Concrete

Self-Consolidating Concrete (SCC) is a new type of concrete and has been developed as a flowable concrete in Japan in the 1980s. Previously, SCC was a product of technological developments in the field of underwater concrete technology where the high fluidity, high resistance to water dilution, and segregation is crucial. SCC is able to place rapidly into the formwork and flow under its own weight. SCC is appropriate for heavily reinforced designs where the section between reinforcement bars is limited. Demand for SCC has increased market recognition and acceptance in the field. Demand was connected to the casting of congested elements and placing of concrete in restricted areas where external vibration could not be possible. SCC shortens construction time, reduces noise, labor cost, and faults generated from workmanship. The purpose of SCC concentrates on high performance, compact, and uniform structure. SCC provides all of concrete's general mechanical and durability aspects. Moreover, it is possible to ensure better surface texture, achieve higher strength, and have shorter construction time. (EFNARC, 2005; Erdem et al., 2009; Ersöz, 2012; Gaimster & Dixon, 2003; Khayat, 1999; Ouchi et al., 2003).

2.2. Delays in Casting

When transportation of concrete to the site or placement of it to the formworks is interrupted, delays in casting are inevitable. This situation leads to cold joints and visible surface lines. However, similar surface lines in appearance may only be a pour line that can occur during regular casting, and the flaw can be dismissed as structurally unimportant (Volz et al., 1997). To even a trained eye, the distinction between these two conditions is usually not apparent at the concrete surface. Cold joint lines indicate the existence of joints where the first layer of concrete had hardened before the successive layer was placed. Figure 2.1 shows visible pour lines and two distinct layers.



Figure 2.1 Successive casting problems

Adding a new layer of concrete to an existing structure may create weak zones, and these vulnerable zones may need to be repaired by demolishing the new layer (Volz et al., 1997).

The casting of SCC structuration rates has to be considered. If a thixotropic SCC has a short time to rest and build structure before the second layer of concrete is placed above it, two layers don't mix, and a weak interlayer zone may appear as an outcome. Researchers also reported strength loss of up to 40%. Durability is another problem for the interlayer zone since this vulnerable interface has more porosity and permeability (Roussel and Cussigh, 2008).

The time limit between layers for casting is given in British standard (BS 8500-1:2006) as follows: Concrete should be cast before it loses its workability. Prolonged breaks in casting can lead to a significant loss of consistency with time making it impossible to place with satisfactory compaction. Extended delay layers, may result a cold joint in interlayer zone. For this to occur, the delay should not be enough for the first layer to develop an initial set. The time for the occurrence of interlayers depends on concrete temperature, cement type, mix proportions, the use of admixtures such as set regulating and/or plasticizing admixtures. Generally, a delay duration of 2 hours is accepted as the maximum time between placing successive layers (Cold Joints, 2020).

2.3. Rheology of SCC

Rheological properties of concrete are related to mixing, handling, transportation, pumping, casting, consolidation, finishing, and surface quality after hardening. Thus, the rheological properties have to be examined to ensure both fresh state and long-term performance (Yahia et al., 2016).

Rheology can be described as the science of the flow of matter and the science of deformation under the effect of shear stresses (Yahia et al., 2016; Banfill, 1991). Liquid materials flow by the action of shear stress causing a sliding motion between subsequent neighboring layers. Several equations were recommended to define the flow of materials. The proposed flow equations for non-Newtonian liquids use at least two parameters to describe the flow (Figure 2.2). Linear Bingham and the non-linear Herschel-Bulkley models shown in this figure are the examples to describe the rheological behavior of cementitious systems such as SCC (Ferraris, 1999). For the Bingham model, shear stress needed to start the flow is shown as yield stress. The slope of the graph gives the plastic viscosity.

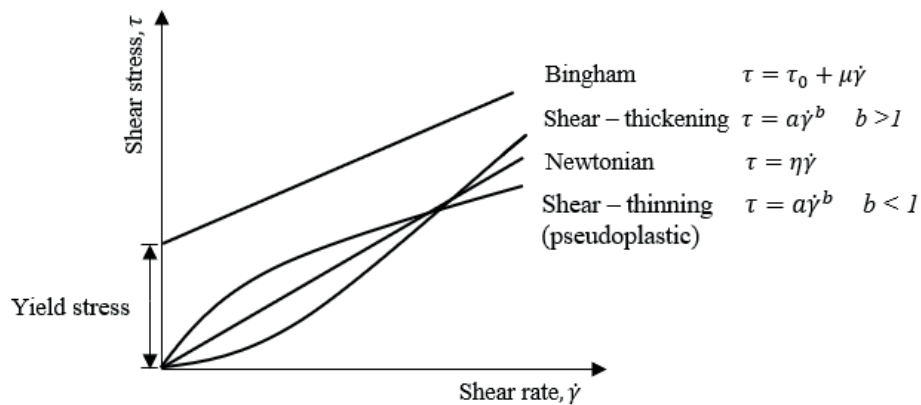


Figure 2.2 Rheological behaviors

2.4. Thixotropy of SCC

Thixotropy definition is given in the literature in various ways (Khayat et al., 2002): The resistance to the flow of a liquid and the degree to reform its matrix is a measurement of its thixotropy level. Basically, a thixotropic concrete has to flocculate

rather rapidly when there is no torque applied; it becomes fluid when the torque is applied (Roussel 2006). According to another definition, thixotropy is continuous decrease of viscosity with time when flow applied to a sample previously at rest and following recovery of viscosity in time when the flow is stopped (Barnes 1997; McNaught and Wilkinson, 2014). Figure 2.3 shows the hysteresis cycle for cement paste.

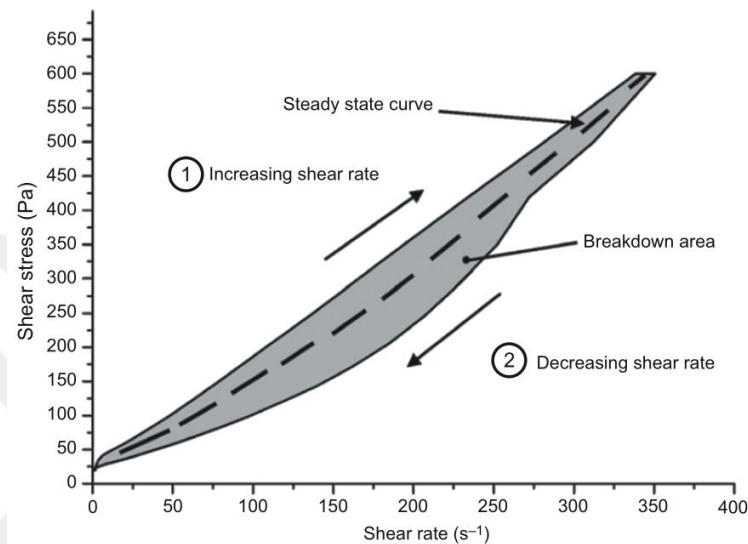


Figure 2.3 Behaviour of the cement paste (Roussel, 2006)

Moreover, it is considered that the difference between rate of “natural” structuration of the material and a rate of de-structuration due to flow is equal to the rate of change of the structuration state, which is proportional to the rate of shear (Roussel e, Le Roy, and Coussot 2004). Ultimately, it is concluded that the yield stress at rest increases as a linear function of time.

In Figure 2.4, it can be seen that a simple physical explanation of the thixotropic yield stress behavior of cementitious materials is given in four steps. Possible colloidal interactions (a) and the energy for the particle is needed to move out from its well (b), and the flow occurs (c).

If the energy is lower than required, the particle comes to its initial position after applied force stops (d) (Roussel, 2006).

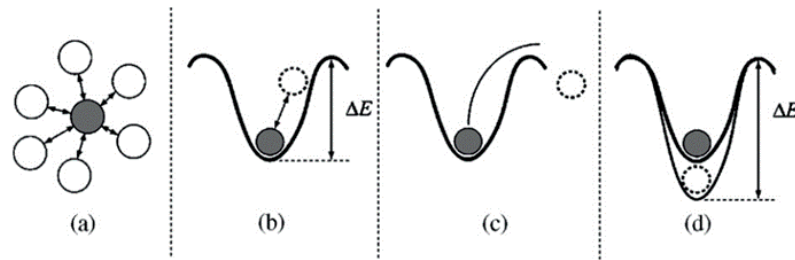


Figure 2.4 Thixotropic yield stress behavior of cementitious particle (Roussel, 2006)

2.5. Superplasticizers

Use of high-range water-reducing admixtures provides high deformability despite very low values of the water-powder ratio (Ouchi et al., 2003). Electrostatic repulsion and steric hindrance are the two mechanisms of action for this type of chemical admixtures. HRWRA molecules adsorb on cement particles, avoid blockage of water molecules, and prevent flocculation of cement particles by repelling each other. The mechanism of action is shown in Figure 2.5. Mechanism of steric repulsion is given, a) adsorption of the polymer on cement particle, b) steric effect of the adsorbed polymer. The second other way of action for the superplasticizer molecules is the electrostatic repulsion (Mehta and Monteiro, 2006).

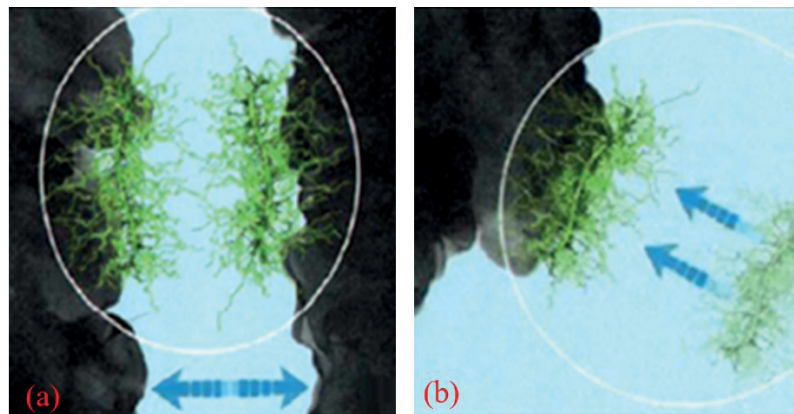


Figure 2.5 Mechanism of action (Aicha, 2020)

2.6. SCC Interlayer Bonding

The bonding between SCC layers is significantly related with the surface roughness of the first layer (Santos et al., 2007). Surface retarders, brushing, or surface roughening increases the strength of the interface layer (EFNARC 2005). The smoothness of the underlying SCC may lower the shear force capacity between layers. Whereas, some researchers (Roussel & Cussigh, 2008) indicated roughness of the first layer has a negative impact on establishing a connection between layers. The interlocking of the layers due to the roughness may be possible; however, the energy needed for the flow of the second layer will increase accordingly. A weak zone may occur between two layers if the stress cannot be eliminated at the interface.

2.7. Air void characteristics of Hardened concrete

Several researchers (Fonseca and Scherer 2015; Zalocha and Kasperkiewicz 2005; Mayercsik et al. 2014; Jakobsen et al. 2006; KW Peterson and Swartz 2001; Kevern et al., 2009) investigated air-void characteristic of hardened concrete cut surfaces. The majority of the studies were focused on cut surfaces and carried out according to the standard (ASTM C 457, 2013).

The earliest study goes to 1977 in which Chatterji and Gudmundsson (Chatterji and Gudmundsson, 1977) implemented an automated procedure for air-void characterization.

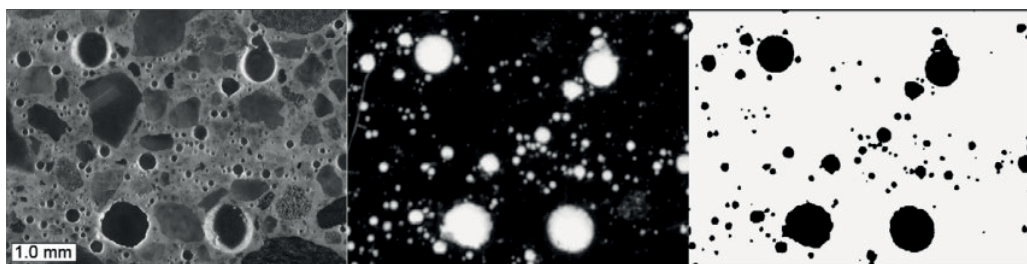


Figure 2.6 Stereomicroscope images

The first step in analyzing a digital image is to segment or classify the pixels corresponding to non-air and air zones in the concrete or mortar matrix. Black and white contrast enhancement and threshold selection were made to distinguish pixels, whether

void or concrete paste and aggregate (Peterson et al., 2009). A flatbed scanner or microscope was used to obtain images from the polished cut surfaces. An example is shown in Figure 2.6 which illustrates the images from a prepared sample (left) and corresponding flatbed scanner image and obtained binary image (right).

2.8. Digital Image Processing and Applications

The development of digital image processing techniques has begun between the late 1960s and early 1970s. At first, it was used in medical applications, astronomy, and earth resources observation. Digital image processing is mostly related to solving the problem by using machine perception (Young et al., 2009).

From 1960's till today, digital image processing has been progressed convincingly. It is used in many applications; firstly medicine and space program. Pollution observations from the images was done by geographers. Moreover, some photos were restored by blurring for archeologists. Successful applications of image processing concepts can be found in astronomy, biology, nuclear medicine, and industrial applications. Machine perception is mainly used to solve problems via 2D image analysis. The main subject of digital image processing is machine perception used to solve problems. Image processing and image analysis try to focus on 2D images, how to convert one image to another, e.g., by pixel-wise operations such as contrast enhancement, local procedures such as edge removal or noise removal, or geometrical transformations such as rotating the image. Image processing/analysis does not deal with assumptions or interpretations of image content (R. Gonzalez and Woods, 2002).

An image can be count as a two-dimensional function $f(x,y)$, where x and y are plane coordinates. The magnitude of any set of coordinates is called the intensity of the image at that point.

A digital image can be identified as finite and discrete points that their magnitude and x,y coordinates are definite. In other words, a digital image consists of multiple pixels with different intensity values (0-255 for an 8-bit image) at various locations. Figure 2.7 is an example for matrix representation of the digital images as pixel intensity values for the selected region in the white square.

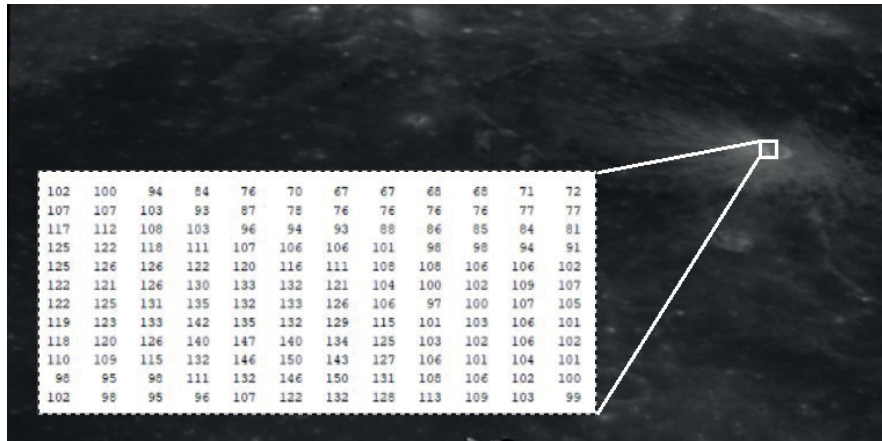


Figure 2.7 Pixel values of the selected region

Basic image processing operations include noise reduction, contrast enhancement, and image sharpening. Usually, input and outputs are images when a low-level process is considered. More complex processing consists of operators like segmentation, description of those objects to lower them to a form proper for computer processing, and classification of individual objects (Young et al., 2009). Basic operations are given in Table 2.1 (a) (b) and (c); after those, some examples of threshold filters are shown from (d) to (f). Thresholding filters performance varies for different pictures and different histogram for the pixel intensity values.

Table 2.1 Sample operations

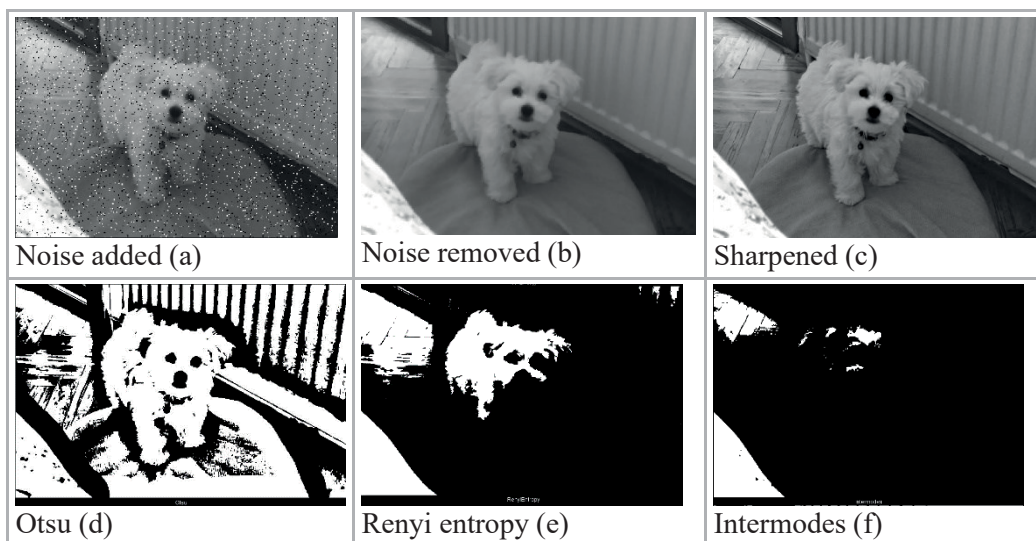
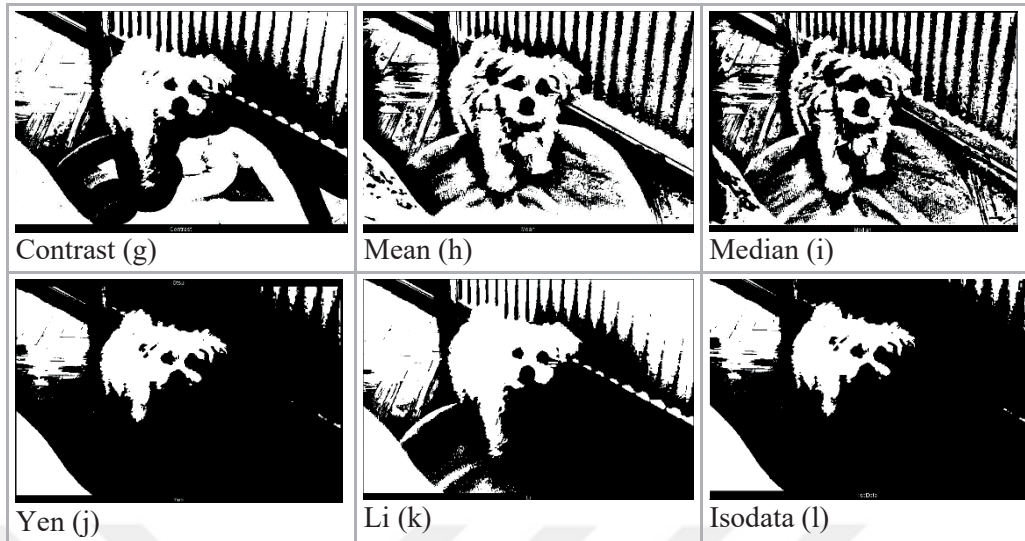


Table 2.1-a Sample operations (continue)



2.9. Theory of Image Acquisition

The image plane and lens are the components of the CCD (charge-coupled device) camera, which holds tiny solid cells that transform light energy into electrical charge. The system gives an analog image as an output. An electric signal is converted from the camera into a digital image by the frame grabber. The digital image is obtained in this manner. Digital images can be seen by a computer (Gonzalez & Woods, 2007; Jähne, 2005) (Figure 2.8).

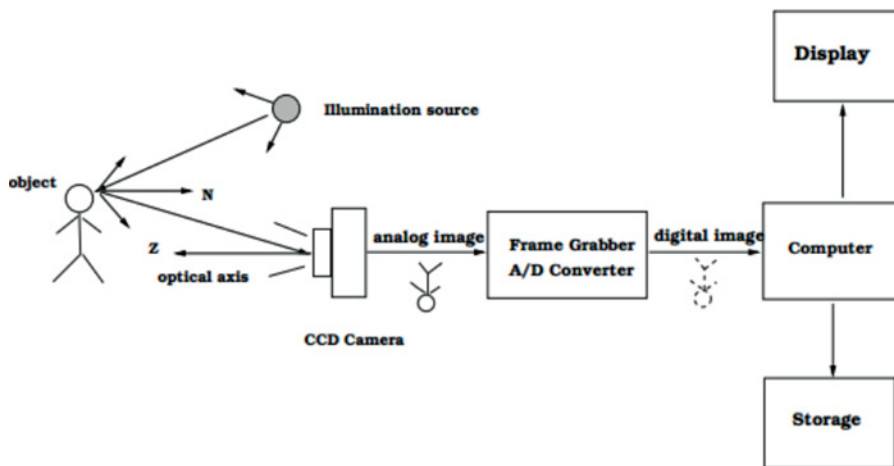


Figure 2.8 Explanation of acquisition of the images (Jähne, 2005)

The first function done by the system is collecting energy and focusing it on an image plane. Light from a source (sun or artificial source) is transferred by the front lens to the focal plane. The response of each sensor, which is made by the sensor array output sensor, is related to the integral of the light energy projected onto the surface of the sensor. Digital and analog mechanisms take these outputs and transform them to a video signal; After this operation, another part of the imaging system digitize it as a digital image (Young et al., 2009; Jähne, 2005; R. C. Gonzalez and Woods, 2007)

2.10. Enhancement and Segmentation of The Images

Repeating steps of the image acquisition inadvertently result in image degradation. Due to mechanical issues, human errors, out-of-focus, blur, motion, noise, insufficient and incorrect lighting, can be lower the condition of the digital image when compared to the original. If the $c[m,n]$ is recorded image, enhanced image will be $\hat{a}[m,n]$, and original image can be thought as $a[m,n]$ (Young, Gerbrands, and van Vliet 2009a). Image enhancement is the group of processes adjusting the deterministic aspects over the initial image.

Image enhancement operates by modifying pixel locations and adjusts the quality of images. Also, image enhancement helps to produce raw data, which is related to the shape, area, and boundaries of the object. Image enhancement is divided into two groups as contrast enhancement methods and spatial filtering methods that sharpen edges and remove much of the image blur (Ersöz, 2012). Contrast enhancement processes modify the relative brightness and darkness of objects in the view to improve their visibility.

To recognize the objects in images, it is crucial that it can be distinguished between objects and the background. A digital image consists of multiple pixels with varying intensity values. A thresholding process is needed to obtain a binary image.

A parameter is expressed as “ θ ” brightness threshold is picked and employed to the image $a[m,n]$ as follows (Young et al., 2009). The algorithm shows a procedure to distinguish dark objects on a light background.

$$\begin{array}{ll} \text{If } a[m,n] < \theta & a[m,n] = \text{object} = 1 \\ \text{Else} & a[m,n] = \text{background} = 0 \end{array}$$

When “ θ ” is a uniform value over the whole image, the process is called global thresholding. When “ θ ” varies over an image, this is called variable thresholding (Gonzalez & Woods, 2002).

Usually, objects are in black, and the background is in white in the binary image. That process is achieved by segmentation techniques – segmenting the foreground from the background. Air voids, surface defects, other changes in surface topography are represented by pixels with different illumination.

While evaluating concrete surfaces, threshold choice is important for the accurate segmentation process. Pixels darker than a threshold level are classified as the surface with voids or defects. Pixels lighter than the threshold level are classified as background for this study. An example image and its histogram are shown in

Figure 2.9. Example histogram consists of pixel values from 0-255. Darker pixels are shown with a number close to zero. The lightest points have the highest number. From

Figure 2.9 b, object and background are illustrated. Uniform gray values make the segmentation process easy. At the same time, thresholding may not be so simple for all images, different techniques may be needed.

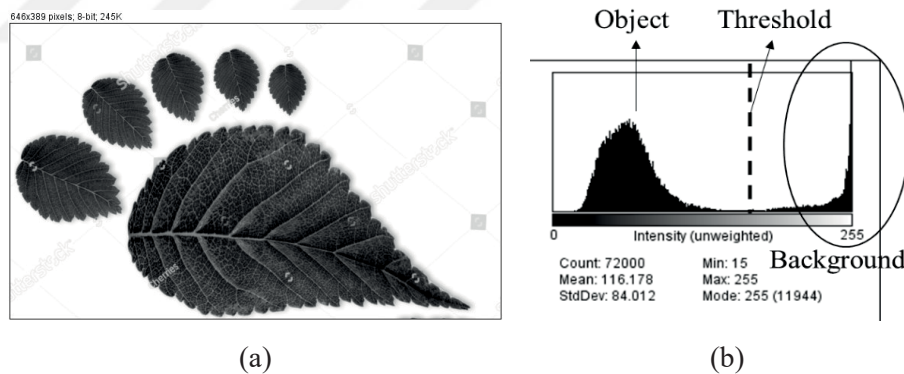


Figure 2.9 a) Example image, b) Histogram of the image

Edge-based segmentation inhibits the segmented object from the change in size without using a complex mechanism. This algorithm searches for local maxima in the edge strength and to follow the maximum along the boundary of the object. Algorithm searches for local maxima in the magnitude of the gradient. When a “maximum” come across, a tracing algorithm tries to track the maximum gradient around the object until it comes to the beginning.

The process repeats for the next maximum, and region-based segmentation works with the adjacent pixels. Region-based segmentation depends on object connectivity status. Iterative functions are used to compute and segmentation. A simple explanation is, to begin with, a set of “seed” points, and from these growing regions by checking neighbouring pixels met the criteria or not (Gonzalez & Woods, 2007).

In this study, a multilevel threshold method called “Yen” was used for the majority of the surfaces (Yen and Chang, 1995). Since the surface conditions are not the same for all concrete specimens, different techniques were implemented for a group of surfaces with insufficient illumination and unexpected surface coloring.

2.11.Previous Studies

In 2011, Billberg P. H. investigated the structural behavior of SCC at rest. Four series of concrete were produced with varying powder, VMA types and content. The CONTEC 4 viscometer was used, torque was applied to the samples previously at rest. Shear stress-shear rate diagram and a change in the static yield stress/time at rest diagram were obtained. It has been reported that 1) increased particle concentration and reduced water to powder ratio increases the rate of structural build-up 2) Increased filler material and fineness affected the interparticle distance. This situation resulted in a narrower system and easy flocculation or coagulation of the mixture (Billberg, 2011).

Roussel N. stated that there exists an intermediate period, say around 30 minutes, which irreversible effects have not yet become significant. If SCC structures too much and its apparent yield stress increases above a critical value, then the two layers do not mix at all and, and as vibrating is prohibited in the case of SCC, a weak interface between the concrete layers may appear in the final structure. The weak interface between layers can be detected visually, and losses of mechanical strength of more than 40% is recorded. Moreover, porosity and permeability to aggressive substances locally increase at this interface zone (Roussel, 2007).

Momayez et al. researched the effect of different tests on bond strength between the concrete substrate and the repair material. Pull-off, Slant Shear, Splitting Prism, and Bi-surface Shear tests were conducted. Two different surface roughness and three different bonding agents were used. One hundred sixty-four specimens were tested. Bond strength decreased with the test method in the following order: slant shear, bi-surface

shear, splitting, and pull-off. Surface roughness increased the bond strength (Momayez et al. 2005).

In 2005, to see the effect of roughness on the concrete-to-concrete bond strength, the authors described a successive study performed to investigate the possibility of quantifying the roughness of the substrate surface and correlate this with the equivalent interface bond strength. The substrate surfaces of the specimens were with prepared with various roughening methods (blasting, wire brushing). The roughness profile of the substrate surface was obtained with digital image processing steps. Different roughness parameters left-as-cast wire-brushed and sandblasted were assessed based on this profile and were correlated with the corresponding bond strength, both in shear and in tension, measured with Slant Shear and Pull-off Tests, respectively. Bond strength was increased with the determined surface roughness for both tensile and compressive strength (Santos et al., 2007).

Wan Z. studied the interfacial shear bond strength between old and new concretes. The researcher changed some of the conditions as water-cement ratio, moisture content of the specimens and tried to see the effect of these factors on bonding strength. Two different moisture conditions (air dry, saturated surface dry: SSD) were used for the twelve old concrete cubes at the interface. Silica fume addition significantly increased both the compressive strength of new concrete and shear bond strength at the interface. New concrete with a w/c ratio of 0.45 resulted in higher compressive strength but lowered shear bond strength. It was found that SSD resulted in higher bond strength. For cylinder specimens, usage of fly ash lowered the bond strength (Wan, 2011).

Mohamadien H. A. investigated the impact of the time when casting the second layer of concrete on the mechanical properties of concrete. The effect of delay in a time period when casting the second layer after 4, 9, and 16 hours for two types of concrete with compressive strength 250 kg/cm² and 300 kg/cm² was studied. Beam, cylinder and cube specimens were used. Compressive strength, splitting tensile strength, and flexural strength were measured. Grout's influence on compressive strength seemed more significant for 300 kg/cm² concrete. Usage of grout coating material in forced separation showed a positive impact on improving mechanical properties. Higher durations like 9 and 16 hours decreased the splitting tensile and flexural strength significantly (Mohamadien et al., 2013).

The effect of cold joint to the strength of concrete was investigated by V. R. Rathi and P. K. Kolase. Compressive strength, split tensile strength, flexural strength was

determined for 3, 7, and 28 days. The bond between old and new concrete with and without retarder (% 0.1 sugar) for 45 min 75 min 120 min and 180 min casting times were studied. Joints were created in three different planes for the specimens. As a result, the horizontal failure plane performed better than other planes (vertical failure plane and diagonal plane). Compressive strength decreased with the time lag between casting times and initial setting time. Lags greater than 75 min showed a drop in both flexural compressive and split tensile strength. Increasing the setting time was proposed as a solution by adding a retarder (Rathi and Kolase, 2013).

Bond strength in multilayer casting of SCC was investigated. Eight SCC mixtures were prepared with an initial slump flow of 63 cm to 70 cm. Concretes having different mix designs; therefore, different thixotropy levels were used. Slump flow, J-ring, T50 tests were conducted. Molds were filled with a single layer, and this operation was repeated after 34 mins and 52 mins. Slant shear and direct shear tests were conducted. Three SCC categories were introduced, and the mixture with low structural build-up developed higher bond strength between layers. The results show that both residual bond strength test values decreased with longer delay times. The highest drop in the bond strength occurred at the highest structural build-up at rest level. Concrete with low thixotropy levels showed a residual bond strength greater than 90% for the resting time of 55 minutes. This value was recorded as 5 minutes for the SCC with high level structural build-up (Megid and Khayat, 2017).

Overlay SCC compressive strength and the ratio between new and old concrete compressive strength were reported as the factors that affects the bond strength. The roughness of substrate concrete had a significant effect on bonding. As a result of using the same type of coarse aggregate for repairing works, improves bond strength by 15%. Adding latex of 5% and 10% by weight of cement to overlay SCC raised bonding strength. Usage of SCC as a repair concrete adjusted with latex (10% of cement weight) or with fibers (with 0.2 % of the volume) was proposed. The usage of overlay concrete strength higher than the substrate was also recommended. This situation can result in a 40% increase in bond strength. Prism specimens represented more reliable results for Slant Shear Test than cylinder specimens. (Diab et al., 2017).

Bond characterization between the concrete substrate and repairing SFRC using Pull-off Test was investigated by Bonaldo et al. By using an adhesive compound, a layer of steel fiber reinforced concrete (SFRC) can be bonded to the existing concrete at the compression surface. Different strength classes of concretes were prepared for substrate

and overlay concrete. It was reported that with the increase in substrate compressive strength, Pull-off strength increased significantly, regardless of the coating material. Tensile test results of the six series of concretes showed that the test data are quite variable. This could be originated from not only the accuracy of the test method but also due to the natural heterogeneity of the concrete material (Bonaldo et al., 2005).

In 2016 Han-Seung Lee et al. investigated the evaluation of bonding shear performance of ultra-high-performance concrete (UHPC) with increase in delay in formation of cold joints. To assess the influence on the bonding shear performance, direct shear tests were made. Delays were set to 0 min, 15 min, 30 min, and 60 min with and without application of tamping. For the normal-strength concrete (NSC), it is thought that a monolithicity of around 95% can be attained with a cold joint formation delay up to 60 min. In contrast, a dramatic degradation in the bonding shear performance was observed after 15 minutes for UHPC (Lee et al., 2016).

In 2008, Roussel and Cusing researched “Distinct layer casting of SCC.” Researchers produced four different types of concrete with slump flow varying from 630 mm to 700 mm. Four different SCC with various structuration rates were prepared. During the study, with changing mix proportions and increasing the powder amount, three times more thixotropic mixture was obtained. Specimens were prepared with 30 mins and 180 mins delay between layers. No visible distinction was detected up to 60 min between layers. A decrease in mechanical strength with a delay between layers was recorded. Most thixotropic mixtures did not show a reduction in mechanical strength with time when compared to mixtures with less thixotropy. Smooth interface between layers was reported as a reason for distinct layer casting. Interlocking decreased with a decrease in coarser particles amount.

Roussel and Cussigh (Roussel & Cussigh, 2008) stated that there's no strong correlation between structuration rate and mix proportioning. Measuring thixotropic loops does not have a contribution to the distinction between structuration and de-structuration abilities of the studied material. However, in this study, authors claimed that both from literature and experimental work, following five factors may affect the structuration rate:

An increase of the Powder content and granular skeleton (sand and gravel) affects the structuration rate.

The structuration rate should increase when the water /powder ratio decreases.

Colloidal effect originated from powder materials increases with the fineness. Structuration rate should thus increase with the specific surface of the powders in the mixture and temperature.

Structuration rate decreases when the superplasticizer content in the mixture increases.

The VMA amount affects and increases the structuration rate.

Accordingly, by increasing the powder amount and powder fineness (addition of F.A. and VMA), an SCC three times more thixotropic than reference SCC was achieved.

Higher roughness resulted in lower drops in long-term bond strength. The authors stated that there is no strong relationship between roughness and thixotropy for early times but for the delays higher than 60 min, a strong correlation was observed. Early stages of the negative role of thixotropy were recorded. For longer durations, the positive effect of roughness is more significant on the bond strength. It was stated that the thixotropy effect on bond strength is more significant in a short time. For longer delays, the impact of roughness was increased.

In another study, a photogrammetric method was introduced to study the relationship between the thixotropy, the roughness of the first layer, and the bond strength of multi-layers. 300*200*200 mm molds were filled in layers. The second layers were placed on the first layers after different delay durations (15, 30, 60, 90, 150 min). Cylindrical cores were drilled in a way to contain both layers horizontally for the mechanical tests. Shear strength in the bond area was calculated. Moreover, the surface roughness index was calculated via MATLAB. Those results were compared with the volumetric test method, according to the ASTM E965 sand coating method. As a result, computer-generated 3D surface topography was counted as a better alternative to the sand coating method since the computer analysis doesn't need hardened concrete (Akbar et al. 2019).

C. Fang and S. Labi investigated the Static Segregation Index on SCC cylinder samples. by developing and implementing a methodology for automatically evaluating SCC stability. A cut surface with various shades was studied by digital image processing. A specially designed chemical solution was sprayed on the cut surface to distinguish the aggregate phase from the cement paste. Light colors were estimated as aggregates, and dark colors were estimated as cement paste. Hardened Visual Stability Index (HVSI) was compared with the results from the static segregation index test results. Results were

obtained with a strong correlation between these two methods with a regression coefficient of 0.9 (Fang and Labi, 2007).

Research about near-surface properties affecting bond strength in concrete repair showed that with increased surface roughness of the first layer, mechanical interlocking can be promoted. Three different types of concrete and four types of surface treatment techniques were used to obtain different surface roughness. Polishing, dry-sandblasting, jackhammering, and high-pressure water jetting were used. After surface treatment, concrete slabs were covered by cement repair mortar (PCC). It was reported that near-surface cracks are crucial for concrete to concrete bonding and for the substrate layer that may affect the adhesion of overlay concrete. Moreover, heavyweight surface treatments like jack-hammering and hydro-demolition influenced microcracking two times higher than other polishing and sandblasting surface treatments, and 50% of cracks developed in the superficial zone. As a result, less aggressive treatment was recommended for concrete substrate with strength class lower than C30/37. It was also reported that surface treatment techniques and surface roughness are key parameters that influence the adhesion (Courard et al., 2014).

According to Beushausen and Alexander (Beushausen and Alexander 2008), concrete with higher fluidity gave better bond properties as it makes the second layer concrete penetration to the open surface pores of the first layer easier. Moreover, second layer was affected the short-term bond strength significantly. If the compressive strength of the overlay concrete is lower than the substrate, failure mostly occurs in the overlay zone. Another bond failure was reported at the interface. Low macro-roughness decreased the bond strength with time at the interface. Smallest bond resistance values were obtained for the interlayer zone.

Pigeon and Saucier (Pigeon and Saucier, 1992) reported that the interface between layers as old and new concrete at different ages is similar to the interfacial transition zone (ITZ). Between substrate and overlay concrete, a wall effect existed and created a weak transition zone.

Delatte et al. (Delatte et al., 2000) reported that the maturity of the second layer of the concrete and bond strength are related to each other. Bond strength was predicted in connection with the strength of overlay concrete.

CHAPTER 3

TEST METHODS AND EXPERIMENTAL PROGRAM

This study consists of several parts, including fresh concrete tests, hardened concrete tests, and analysis of the images captured by an automated system with artificial illumination.

The mixtures were designed to have a total cement content of 446 kg/m³. Three different w/c was selected as 0.36, 0.41, and 0.46. For each w/c, slump flow was adjusted to 60 or 70 cm ±2 cm by varying the superplasticizer content. For a certain w/c and slump flow value, the Fine Aggregate / Total Aggregate ratio (FA/TA) was changed as 0.45, 0.50 and 0.55. Mixture proportions of 15 different concrete mixtures can be seen in Table 3.1. The labeling was done in the order of w/c, FA/TA, and slump flow diameter in cm.

Table 3.1 Mixture proportions

Mix ID	w/c	Slump flow (cm)	Fine /total aggregate	Water (kg/m ³)	0/5 aggregate (kg/m ³)	5/15 aggregate (kg/m ³)	Superplasticizer (l) amount for 1 m ³	Total (kg/m ³)
36/45/60	0.36	60	0.45	160.6	734	902	3	2242.6
36/55/60			0.55	160.6	917	736	4	2259.6
36/45/70		70	0.45	160.6	734	902	4.5	2242.6
36/50/70			0.5	160.6	821.67	821.9	3.3	2250.1
36/55/70			0.55	160.6	917	736	3.9	2259.6
41/45/60	0.41	60	0.45	183	712	871	2.3	2212
41/50/60			0.5	183	795	795	1.7	2219
41/55/60			0.55	183	871	712	3.1	2212
41/45/70		70	0.45	183	712	871	1.5	2212
41/50/70			0.5	183	795	795	2.4	2219
46/50/60	0.46	60	0.5	205.2	768.9	768.7	1.2	2188.7
46/55/60			0.55	205.2	849	695	2.4	2195.2
46/45/70		70	0.45	205.2	688.6	841.8	1.6	2181.6
46/50/70			0.5	205.16	768.9	768.7	2.2	2188.7
46/55/70			0.55	205.2	849	695	2.5	2195.2

Following the mixing operation, the slump flow test was performed immediately. If the target slump flow was not reached, the mixture was discarded and a new mixture was prepared. When the target slump flow was obtained, a sample was placed into the rheometer for rheology and thixotropy tests. The remaining part of the mixture was used for the other fresh state tests. Specimens were taken to determine compressive strength, as well.

According to the fresh state test results, three concrete mixtures having low, high and medium values of thixotropy were selected for the further parts of the study. This selection will be explained in the results section. Then, several types of specimens were prepared for different types of the hardened concrete tests. The summary of the work program can be seen in Figure 3.1.



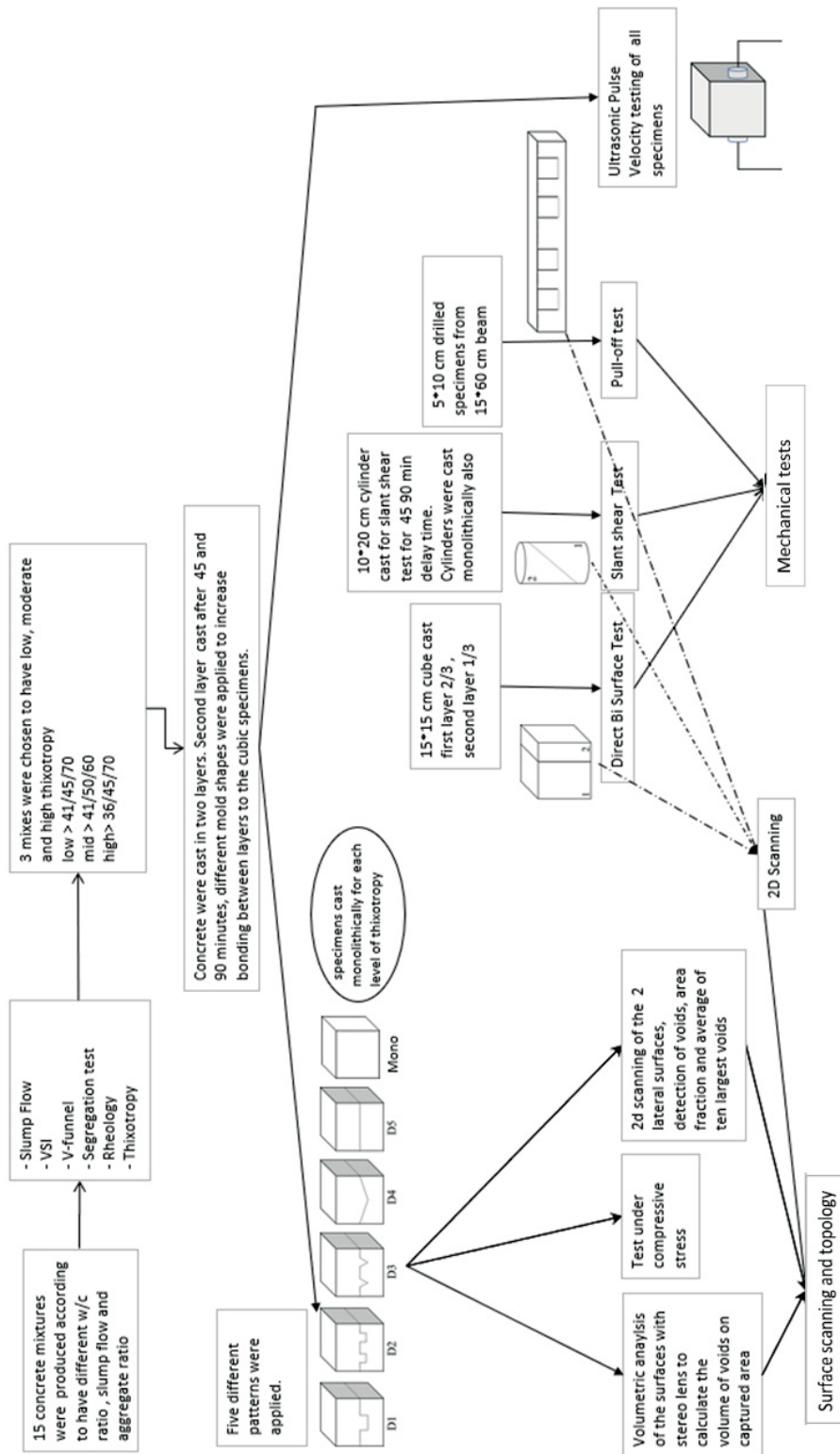


Figure 3.1 Work Flow

3.1. Materials

3.1.1. Cement

In this study, a pozzolanic type cement, CEM IV / B (P) 32.5 R, was used. A pozzolanic cement was preferred because of its market recognition. The chemical analysis of the cement was determined by XRF in IZTECH Materials Research Center. Results can be seen in Table 3.2.

Table 3.2 Properties of cement

Oxides	% by weight
CaO	54.2
SiO ₂	17.7
Al ₂ O ₃	11.6
Fe ₂ O ₃	2.8
SO ₃	1.6
MgO	3.1
Na ₂ O	7.3
K ₂ O	0.9
Loss on ignition	5.0

Normal Consistency and setting time were determined according to ASTM C 191 (ASTM, 2008). Initial setting time and final setting time were found as 60 minutes and 203 minutes, respectively.

The fineness of the cement was found as 4611 cm²/gr in Çimsa Mersin Cement factory laboratory. The specific gravity of the cement which was determined according to ASTM C 188 (ASTM, 2016) was 3.03.

3.1.2. Aggregate

3.1.2.1. Sieve Analysis

Mixed limestone aggregate with 16 mm Dmax was received from a local supplier. Firstly, all of the aggregate was sieved through 5-mm sieve to separate the aggregates

into two different sizes as 0-5 mm and 5-15 mm. Then sieve analysis test was conducted on both aggregate sizes according to ASTM C 136 (ASTM International 2010) using a mechanical sieve shaker. Table 3.3 shows the sieve analysis of the 0-5 mm and 5-15 mm aggregates. The sieve analysis of the as-received aggregate is also shown in the same table. The fineness modulus was calculated as 5.76.

Table 3.3 Sieve analysis results of the aggregates

Sieve opening (mm)	0-5 mm (% passing)	5-15 mm (% passing)	As-received aggregate (% passing)
16	100	100	100
8	100	34.73	74.24
4	98.56	2.06	53.65
2	72.49	2.06	42.14
1	44.97	2.06	26.56
0.5	26.36	2.06	15.60
0.25	16.35	2.06	9.24
0.125	3.56	2.06	3.12
0.063	1.81	2.06	0.22

In this study, three different aggregate grading were employed by mixing the 0-5 mm and 5-15 mm aggregates in certain proportions. After mixing, aggregates which have fine aggregate / total aggregate ratios of 0.45, 0.50 and 0.55 were obtained for making the concrete mixtures.

Fuller curve is an empirical curve that has been proposed by Fuller in 1907 (W.B. and Thompson, 1907). Fuller equation can be seen in equation (3.1) .

$$p_i = \left(\frac{d_i}{D}\right)^{0.5} \quad (3.1)$$

p_i = percent passing i^{th} sieve

d_i = opening size of i^{th} sieve

D = maximum particle size

Figure 3.2 shows the comparison of Fuller curve with the newly formed aggregates with FA/TA of 0.45, 0.50 and 0.55.

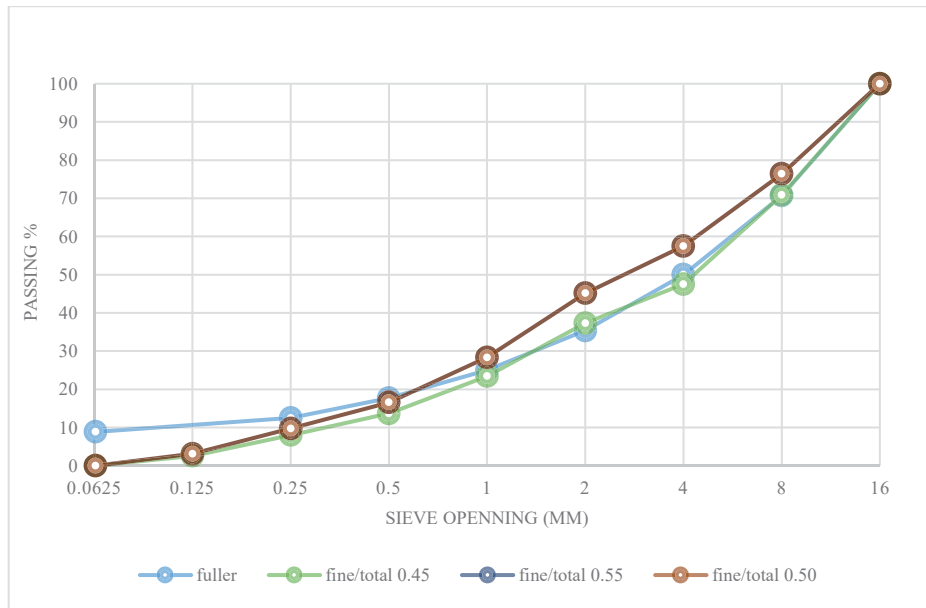


Figure 3.2 Fuller curve with three ratios of F.A/T.A

3.1.2.2. Bulk Density

Bulk density was determined according to the ASTM C29 (ASTM, 2017). To determine bulk density, 3 liter, and 15-liter containers were used for fine and coarse aggregate, respectively. Bulk density of 0-5 mm and 5-15 mm aggregate sizes was found as 1810 kg/m^3 and 1510 kg/m^3 , respectively.

3.1.2.3. Specific Gravity and Absorption Capacity

The specific gravity and absorption capacity of 0-5 mm aggregate was conducted according to ASTM C128 (ASTM, 2015). Accordingly, SSD specific gravity and absorption capacity was determined as 2.54 and 2.28%, respectively.

For the 5-15 mm aggregate, ASTM C127 (ASTM, 2015) was used. SSD Specific gravity was 2.27 and absorption capacity was 3.03%.

3.1.2.4. Void Content Of Fine and Coarse Aggregate

Void content can be calculated using the formula in equation (3.2)

$$\text{Void Content, \%} = 100 * \frac{[(S * W) - M]}{S * W} \quad (3.2)$$

M= Bulk density of the aggregate

S=Specific Gravity

W=Density of water, 998kg/m³

Accordingly, void content of 0-5 mm and 5-15 mm aggregate sizes was determined as 34 % and 29.1 % respectively.

3.1.3. Superplasticizer

A polycarboxylic ether type superplasticizer (Glenium SKY 608) confirming the specifications in ASTM C 494 (ASTM, 2013) was used. Properties of the superplasticizer provided by the manufacturer can be seen in Table 3.4 .

Table 3.4 HRWRA properties

Type	Modified Polycarboxylic Ether Based
Appearance	Brown
Density	1.069 – 1.109 kg/lt
pH-value	5-7
Chlorine content	< 0.1 (by mass)
Alkali content	< 3.00 (by mass)
Recommended dosage	0.8-1.5 in 100 kg binder

3.2. Test Methods for Fresh SCC

3.2.1. Slump Flow Test and T₅₀

The slump flow test is a test method to assess the flowability of SCC. It gives information about SCC's consistency, and it is a single factor test with limited capability for all SCC. Slump flow value is a measure of yield stress of concrete. As stated in (Domone, 1998) and (Tattersall and Banfill, 1977), workability tests measure a single but different value; such tests measure apparent viscosity at an arbitrary shear rate.

Slump flow test was performed following the procedure described in EFNARC. Briefly, after the concrete is placed to the slump cone without compaction, the cone is removed vertically. When the flow is stopped, the diameter of the spread is measured Figure 3.3 At the end of the test, the presence of any segregation was checked visually (EFNARC 2005). For an additional measure of flowability, the time required for the concrete to spread to a diameter of 500 mm can be measured and recorded as T₅₀ time (EFNARC 2005).

In this study, two diameters of slump flow, 60 ± 2 cm and 70 ± 2 cm, were aimed. Target slump flow was achieved by changing the superplasticizer content of the mixtures.



Figure 3.3 Slump Flow Test

3.2.2. Visual stability index (VSI)

It is possible to qualitatively assess the stability of SCC after performing the slump flow test. A visual stability index (VSI) has been developed to determine the stability, as shown in Figure 3.4. On a scale of zero to three, a numerical score is assigned based on a visual evaluation of the segregation and bleeding in the concrete sample (Table 3.5). Typically, SCC with a rating of 0 or 1 could be considered acceptable. For example, the picture at the left side of Figure 3.4 has a VSI of 2 while the right-hand side picture has a VSI of 0.



Figure 3.4 VSI = 2 for the left SCC and VSI = 0 for the right SCC

Table 3.5 VSI values (EFNARC, 2005)

VSI value	Criteria
0 = highly stable	No evidence of segregation or stable
1 = stable	No evidence of segregation and slight bleeding observed as a sheen on the concrete mass
2 = unstable	A slight mortar halo ≤ 0.5 in. (10 mm) or aggregate pile in the center of the concrete mass, or both
3 = highly unstable	Segregating by evidence of a larger mortar halo >0.5 in. (10 mm), or a large aggregate pile in the center of the concrete mass, or both

3.2.3. V-Funnel Test

According to EFNARC (EFNARC 2005), the V-funnel test is used to determine the viscosity and filling ability of SCC. It is connected to the viscosity by describing the rate of flow but it is not a direct measurement of viscosity.

V-funnel test was carried out following the procedure given in EFNARC guidelines. The test apparatus is a V-shaped funnel with the dimensions given in

Figure 3.5. The concrete is filled to a V-shaped funnel. At the bottom, concrete is blocked with a door and a hinge. When the funnel is fully filled, the door at the bottom is opened. The time between the door opening and the instant when the light is visible from the top is recorded as (V-funnel time).

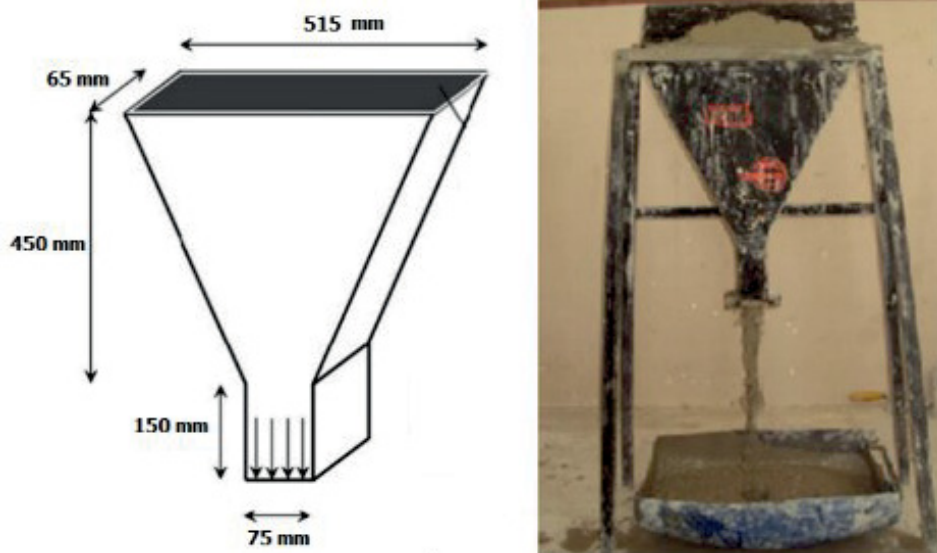


Figure 3.5 V-funnel Test (Erdem et. al., 2012)

3.2.4. Sieve Segregation Resistance Test

The sieve segregation resistance test in the EFNARC is described as follow: Concrete is poured into a bucket and left to stand for 15 minutes (EFNARC 2005). Hereafter, the upper 5 kg of concrete is poured onto a 5 mm sieve, and the amount of

concrete passing the sieve in 2 minutes is recorded. Segregation ratio is obtained from the ratio of the passing material to all weighted material.

3.2.5. Setting Time of Concrete

The test was carried out according to ASTM C 403 (ASTM, 2008). A mortar from fresh concrete was sampled by sieving. The sample was placed in a container, covered with wet burlap, and kept at a certain temperature. At regular time intervals (30 minutes for this experiment), the resistance of the mortar to penetration was determined. 32 mm² tip concrete mortar penetrometer was used. The measured force is divided to the tip cross-sectional area to find the penetration stress. Then the penetration stress vs. time curve is drawn. Initial and final setting time correspond to the penetration stress of 3.5 and 27.8 MPa respectively. For the mixture 41/50/60 (0.41 w/c ratio, 0.50 Fine/All aggregate ratio and 60 cm of slump flow), initial and final setting time were determined as 272 min and 433 min, respectively, as can be seen from the Figure 3.6.

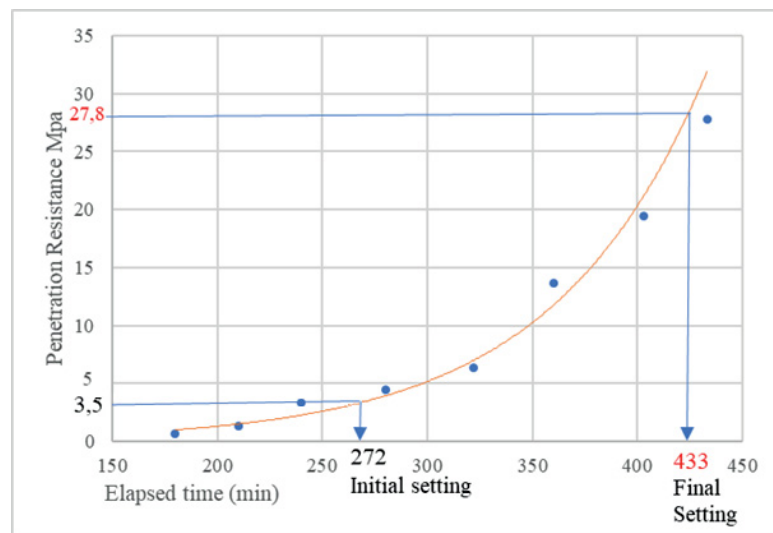


Figure 3.6 An example for setting time determination

3.2.6. Rheology

Concrete rheometer Contec 4SCC with a Tattersall type pallet (Figure 3.7) was used for the rheology tests. According to previous experience (Assaad, 2004) and literature search (ACI Committee 238 2008), the impeller is rotated at six different speeds (0.8, 0.70, 0.55, 0.40, 0.25, and 0.10 rps). The measuring sequence started from the highest speed to the lowest speed. Each speed was applied for 8 seconds. The torque values are obtained during the last 6 seconds. Those data are used in calculating the average torque value corresponding to that speed. 4 torque data per 1 second were recorded, and therefore, $6 \times 4 = 24$ data were averaged. The torque-rotation speed chart (rheogram) is generated for each concrete mixture. An example rheogram can be seen in Figure 3.7. In this chart, the torque value corresponding to each speed can be seen. Bingham model is constructed by adding a linear trendline to the data. The intersection point of the trend line with the torque axis corresponds to apparent yield (g), and the slope of the trendline is defined as torque plastic viscosity (h) (Ersöz 2012). From Figure 3.8 , which belongs to one of the mixtures of this study, $g = 113.6$ N.mm and $h = 3532.6$ N.mm.s. Rheological parameters for each mixture were also determined 45 and 90 minutes after casting.



Figure 3.7 Contec 4SCC rheometer

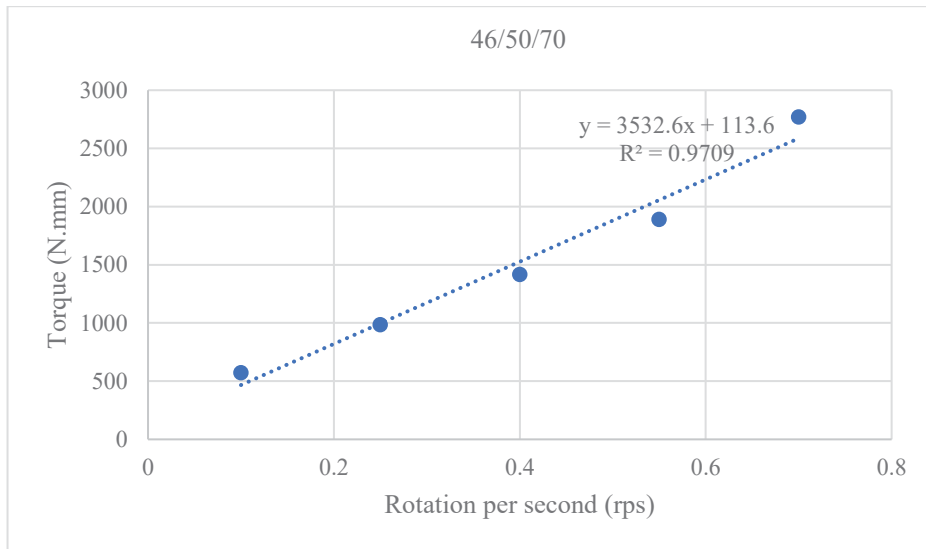


Figure 3.8 An example rheogram

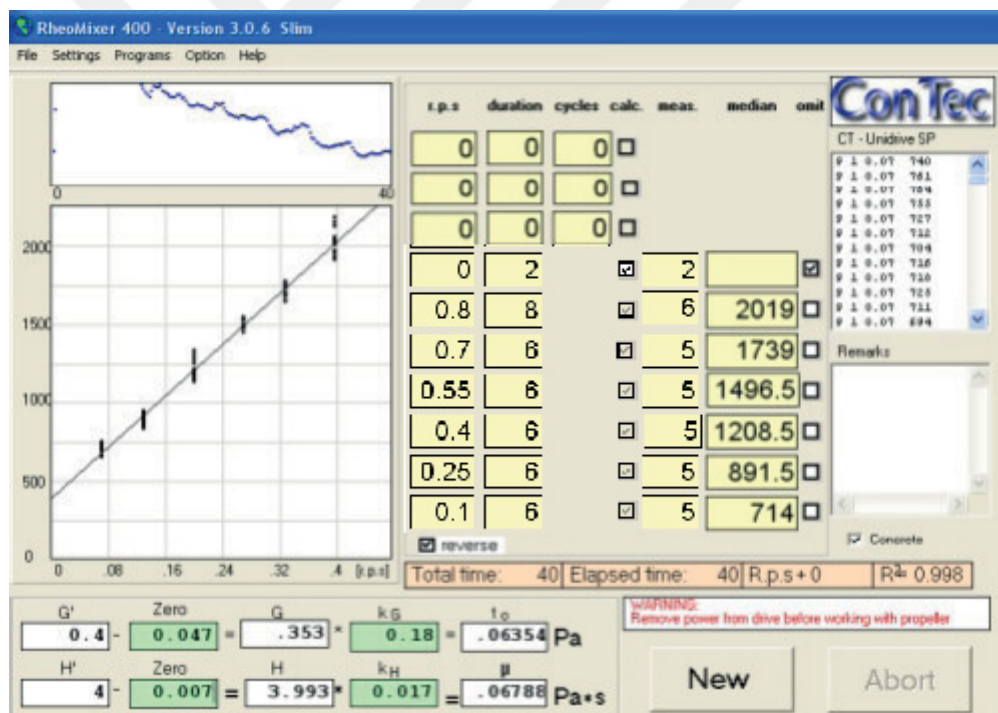


Figure 3.9 Rheometer software

The rheometer used in this study is controlled with a software with a graphical interface. The main controls of the program can be seen in Figure 3.9. Start and stop button, a menu to adjust the rotation speed and duration, a graph that displays the measured resistance at each rotation speed are the elements of the program window. The

software is programmed to log the measurement value from the drive four times per second. The rate and duration of the rotational speed can be determined by the user, and the corresponding torque values are displayed in real-time on the measurement graph. The measurement graph has rotation speed on the x-axis and torque on the y-axis. The oblong graph above the measurement graph displays the measured torque as a function of time. All of the data can be saved to a CSV file at the end of the test (Ersöz 2012).

3.2.7. Thixotropy

Thixotropy was calculated by four different methods stated in the literature (Assaad 2004; Dzuy and Boger 1985; Lapasin et al., 1983):

1. Yield value at rest
2. Structural break-down area
3. Breakdown percentage
4. Drop in apparent viscosity

These are explained below:

1) Yield value at rest: A very low constant rotational speed (0.03 rps) is applied to a sample rested previously for a predefined duration of 5 minutes in a container. Torque-time profile is obtained. Maximum torque is recorded as an index of thixotropy (Figure 3.10).

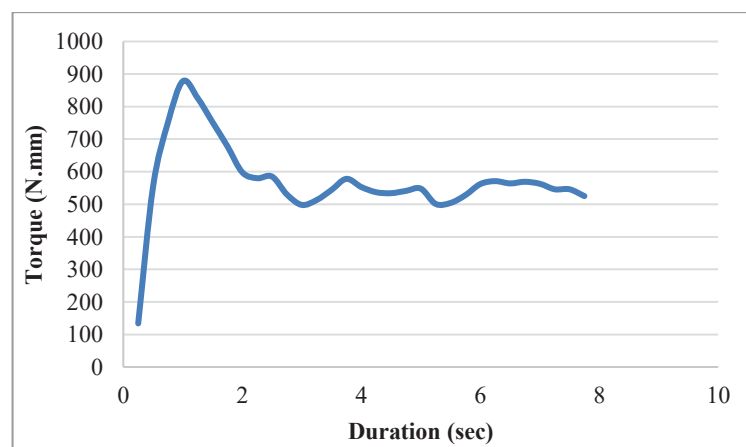


Figure 3.10 Yield value at rest

2) Structural break-down area: Constant rotational speeds of 0.2 rps, 0.4 rps, 0.6 rps, and 0.8 rps were applied to the concrete for 10 seconds and the torque values were recorded as a function of time as shown in Figure 3.11. Before the application of each speed, the concrete was allowed to rest 5 min in the rheometer container. The maximum torque value for each speed is recorded as the initial torque value (Ti) required to breakdown the structure. Four data were recorded for each second, and the average of last 3 seconds (or last 12 torque data) for each rotational speed was taken as equilibrium torque value (Te). Then, initial torque values and equilibrium torque were plotted against speed values (Figure 3.12). Second-degree polynomial equations were fitted to the data and the area between the curves is calculated by integration. The area between the curves, which is called structural breakdown area, is an index of thixotropy.

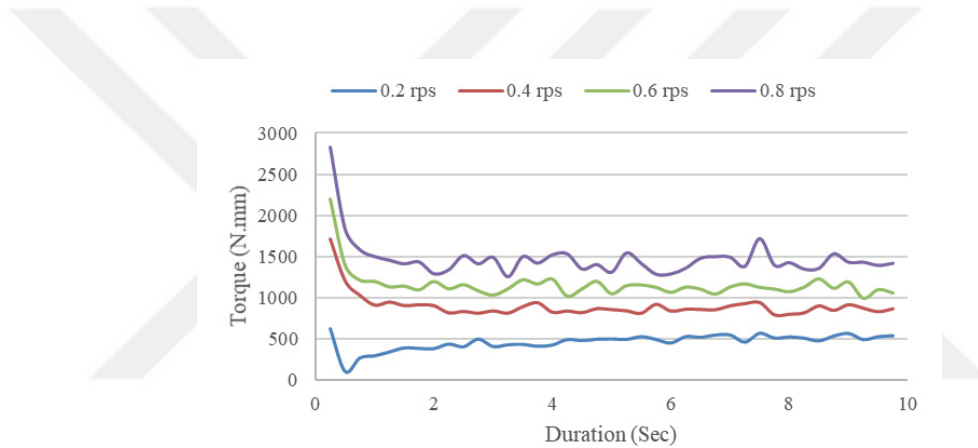


Figure 3.11. Time-dependent change of torque at four different speeds

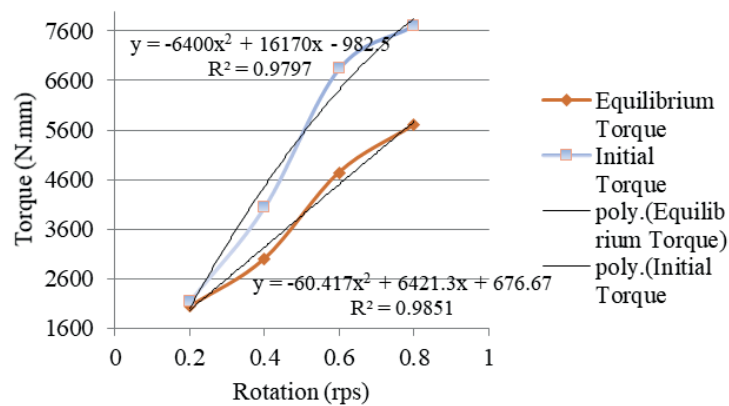


Figure 3.12 Structural breakdown

3) Breakdown percentage: Only the torque-time curve for 0.4 rps, obtained during the structural break-down area method, was used for this method, and therefore it did not require extra tests. Breakdown percentage, which is an index of thixotropy, is calculated from equation (3.3):

$$\text{Breakdown percentage} = (\text{Initial torque} - \text{Equilibrium torque}) / \text{Initial torque} \quad (3.3)$$

4) Drop in Apparent Viscosity: Again, only the torque-time curve for 0.4 rps, obtained during the structural break-down area method, was used for this method, and therefore it did not require extra tests. Drop in apparent viscosity, which is an index of thixotropy, is calculated from the difference between the initial and equilibrium torques divided by 0.4 rps as seen in equation(3.4).

$$\text{Drop in apparent viscosity} = (\text{Initial torque} - \text{Equilibrium torque})/0.4 \quad (3.4)$$

3.3. Test Methods for Hardened SCC

3.3.1. Image Processing & Analyzing

3.3.1.1 Image Acquisition System

Acquiring the images from a system was carried through sensors that are arranged in the form of a 2-D array. CCD (charge-coupled device) cameras consist of this type of 2-D arrays. Each sensor's response is proportional to the light energy integral projected on the sensor surface. A complete 2-D image can be obtained by focusing the energy pattern onto the surface of the array. Digital circuitry gathers these outputs and transforms them into a video signal, which is then digitized by another part of the imaging capturing device (Fang and Labi, 2007).

A superficial profile was obtained for specimens by using an imaging system prototype. The system consists of a digital SLR camera (Canon 500D Sigma 50mm f/2.8

EX DG Macro Autofocus Lens) and an illumination system that ran in different combinations and created different shadow lengths.



Figure 3.13 Operation illumination and camera controls

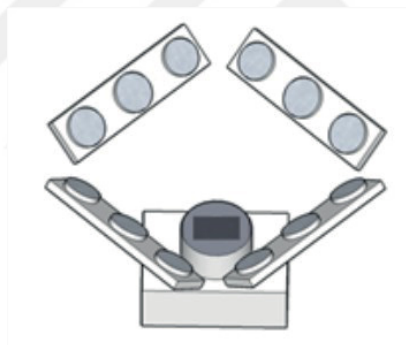


Figure 3.14 Led lamps

The scanning procedure can be seen in Figure 3.13. On the left, illumination from 12 Led lights is seen. Those lights ran in different combinations and created different shadow lengths on the concrete surface. An automated process captures eight images in a row. Only 4 of them are used. In the right picture, controls are shown. The illumination system can be seen in Figure 3.14.

In the second part of the image capturing process, the lens of the camera was changed, and the 3D macro stereo lens was mounted to the system. Lenses can be seen in Figure 3.15.



Figure 3.15 (Left) 2D macro lens (Right) 3D macro stereo lens

3.3.1.2 2D Image Analysis with Image J

An open-source software, Image j, is used to calculate area and count voids on the concrete surface. Images were analyzed using a macro. Image processing steps were followed, and those steps will be explained in this section. Eight images were obtained per surface (images of the surface of D4MID45 was chosen). An example of these eight images is shown below in the image (Figure 3.16).

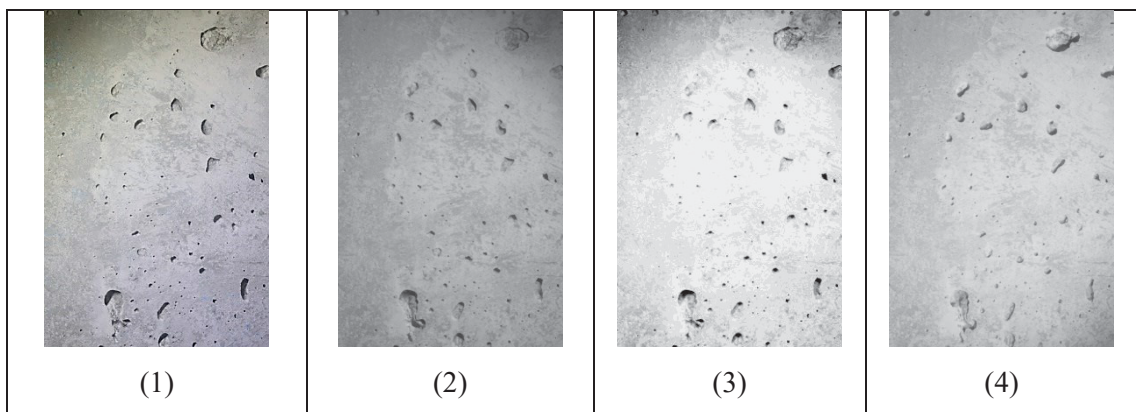


Figure 3.16 Different illumination cases as obtained images from 1 to 4

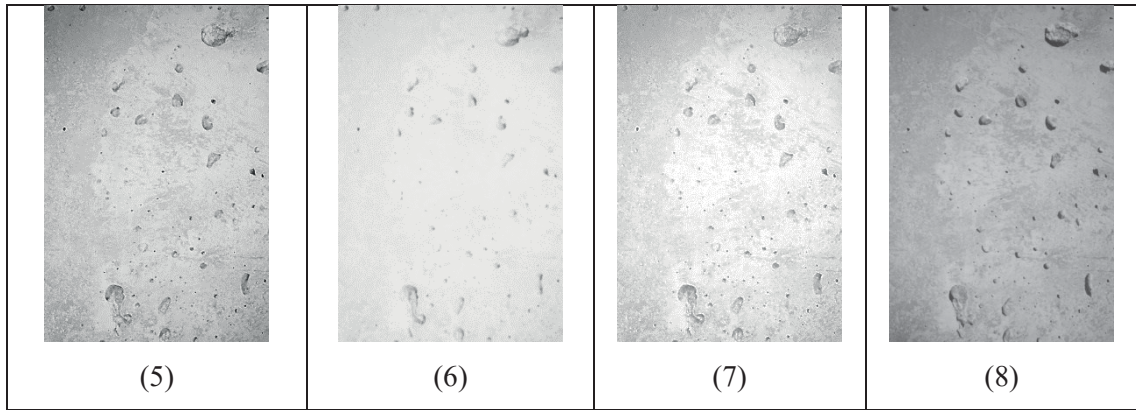


Figure 3.17a Different illumination cases as obtained images from 4 to 8

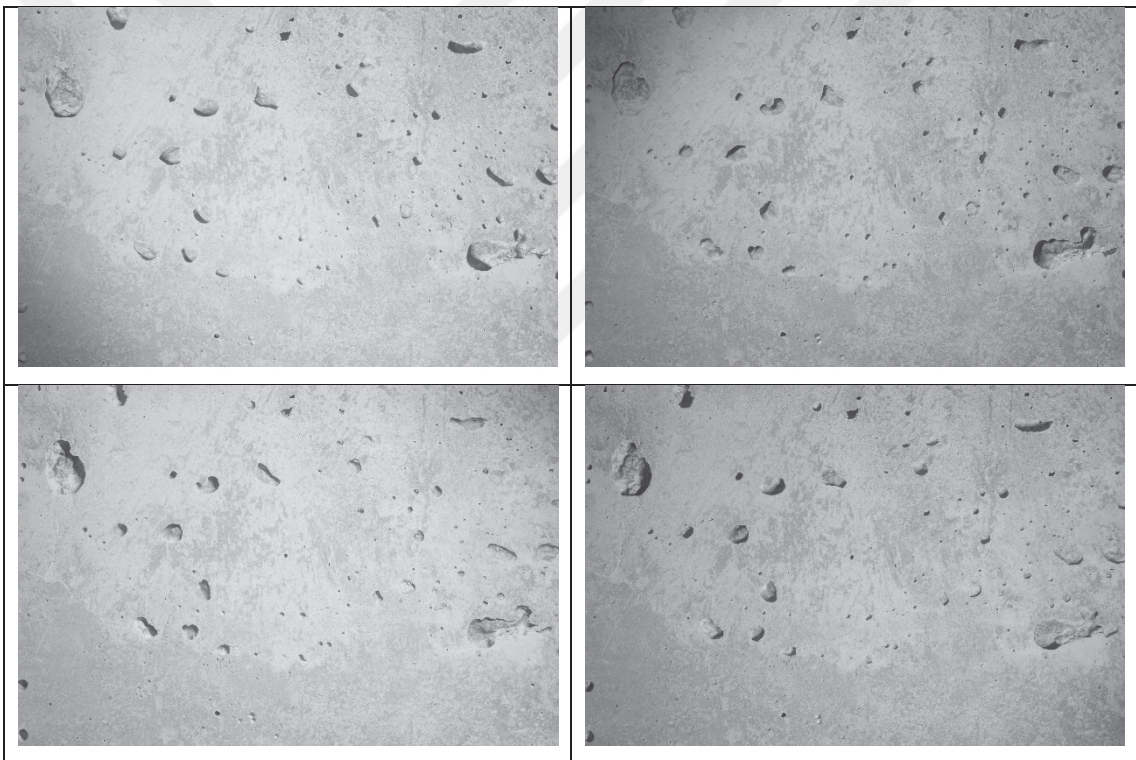


Figure 3.18 Illumination from up, down, left, and right (D5MID454)

From the Process menu of the Image J software, the Image calculator is chosen. 4 of the first eight images were picked. Illumination from four sides of the specimen is obtained by running a combination of automated led lambs. Those lamps are running with an electrical circuit. The obtained images can be seen in Figure 3.17.

The image calculator performs logical operations between two images. Every pixel of an 8-bit image has a gray value. That value changes between 0-255. 0 refers to black, and 255 refers to white. The image J calculator tool is used to select the darkest and lightest points for images in pairs. Darkest points mean voids with minimum depth. An explanation is shown Figure 3.19 .

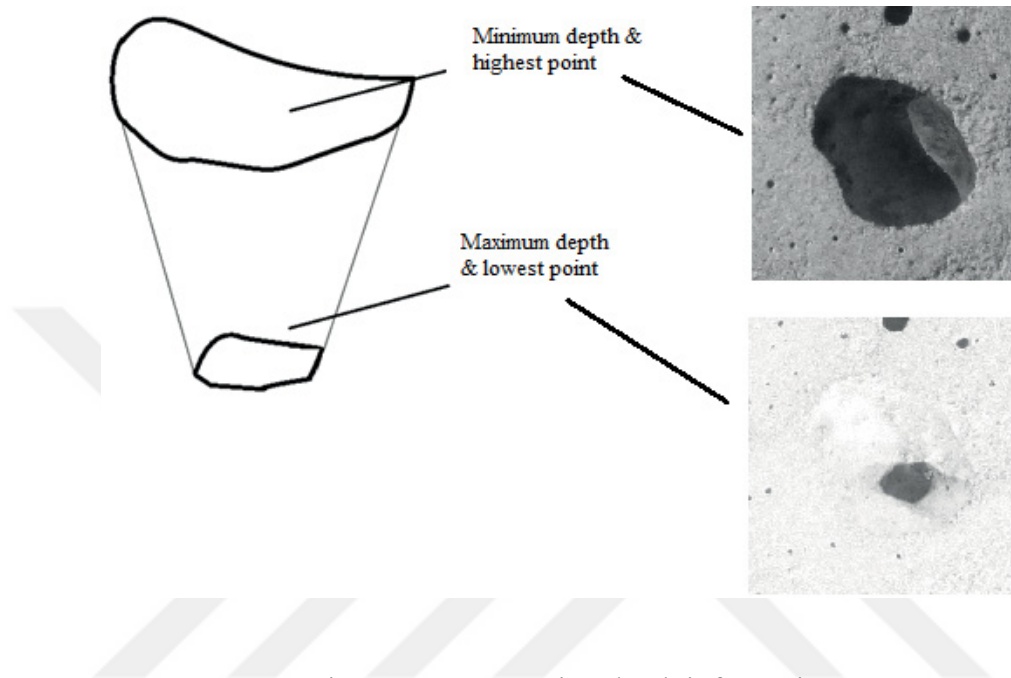


Figure 3.19 Extracting depth information

The minimum pixel values are selected by using logical operators. The same procedure followed for selecting the max pixel values, max and min gray values of images can be seen in Figure 3.20.

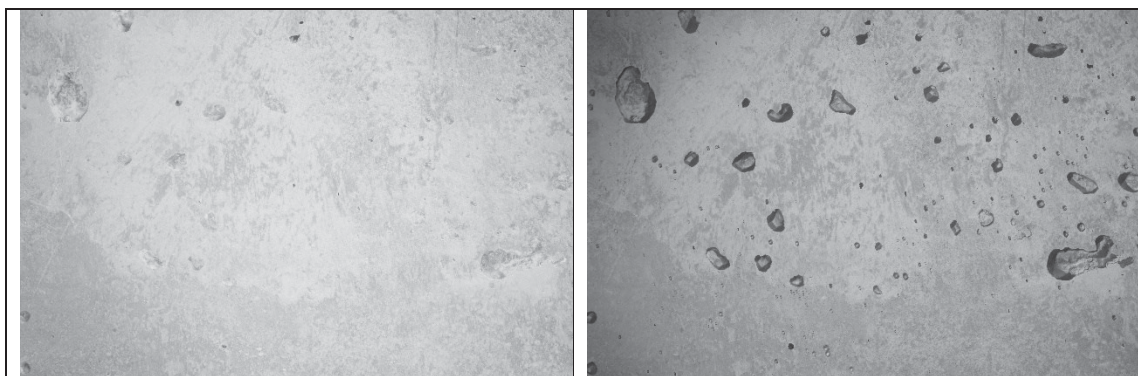


Figure 3.20 Max and min

After the selection of maximum and minimum gray values and shadow length of images, the following operation should be the application of threshold methods to acquire segmented pictures (Ersöz, 2012). An example binary image can be seen in Figure 3.21.

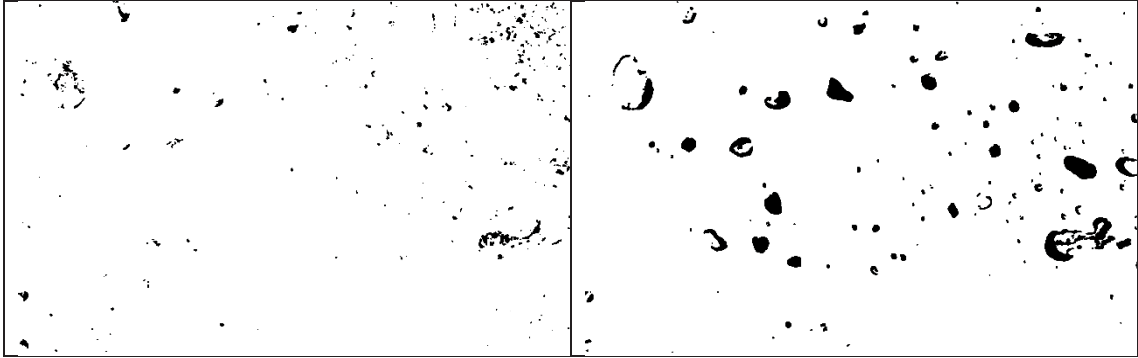


Figure 3.21 Binary image for min and max

With the Yen threshold method, maximum and minimum 8-bit images were inverted to binary images. Thresholding is possible by selecting a pixel density value above which the pixel will be rated as belonging to a particle; below this, it will be accepted as background. Binary images for the other surfaces are given in Appendix A.

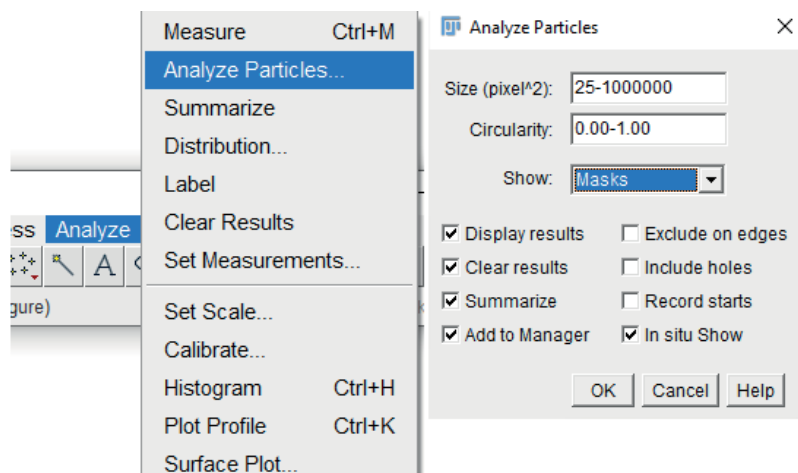


Figure 3.22 Analyze particles

From the Analyze menu (Figure 3.21), an output table is obtained from Image J. Two tables are obtained: summary and results. Void count, surface, and a total area of voids are selected. Voids and defects smaller than 25 pixels were ignored. Voids smaller than 25 pixels were accepted as noise. A binary image can be seen in the figure. Two types of output window are obtained. In the results table, every void or defect is explained numerically. In the summary window, average values of all defects and voids can be seen in Figure 3.23

Summary.csv							
File Edit Font							
Slice	Count	Total Area	Average Size	%Area	Mean	Perim.	Feret
min.tif	165	248774	1507.721	1.653	252.109	121.244	37.381
max.tif	175	108169	618.109	0.719	251.476	118.361	35.100

Figure 3.23 Summary of Image-j analysis results

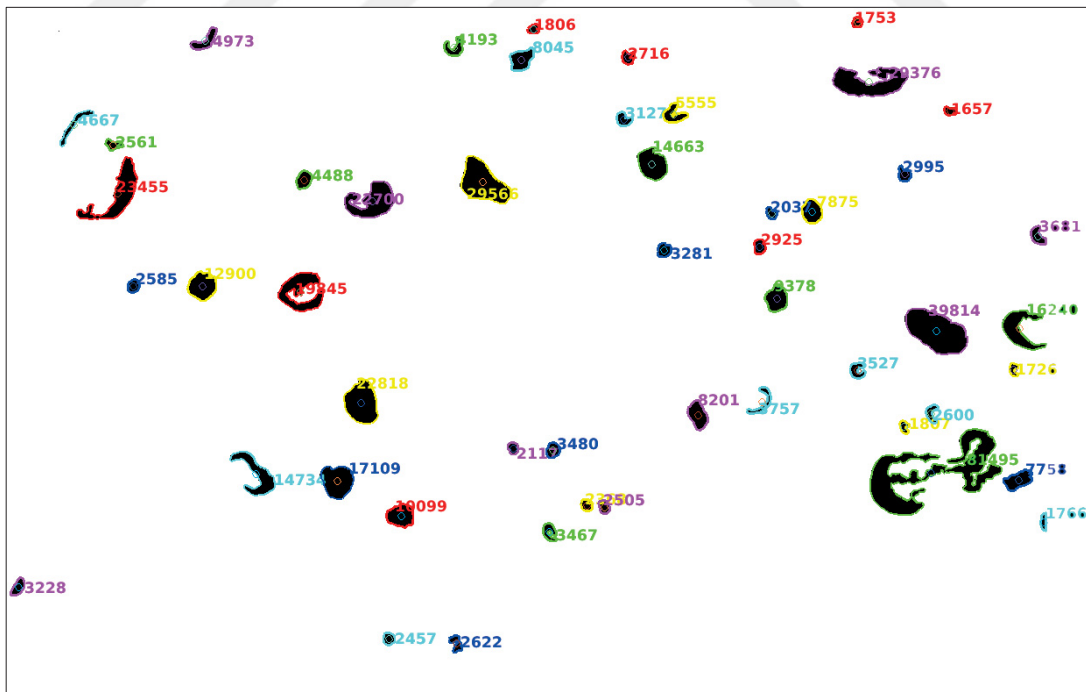


Figure 3.24 Area labelled voids of binary image

In this work, summary of data was used for discussions. Some information about the surface is disregarded to hold the parameters. Figure 3.24 is an example of a binary image. A binary image is the result of the threshold and segmentation process. Edge-based segmentation was used in this study.

Analyzed points can be seen in Figure 3.24. The area of the voids is illustrated as numbers beside. Every black pixel was recognized as a void or defect by Image J. White pixels were assumed as a smooth surface. Figure 3.25 shows only a part of the analysis results for an example surface. Results of all voids and extended results table are given in the table in Appendix B.

	Area	Mean	Min	Max	Perim.	Feret	%Area	FeretX	FeretY	FeretAngle	MinFeret
1	29376.000	255	255	255	1263.141	344.907	100	3775.000	348.000	4.157	132.849
2	1502.000	255	255	255	154.610	58.241	100	8.000	3047.000	15.945	32.772
3	1272.000	255	255	255	133.882	46.487	100	4217.000	2202.000	18.825	36.000
4	180.000	255	255	255	48.284	17.088	100	4621.000	1608.000	20.556	14.000
5	7758.000	255	255	255	394.032	137.993	100	4557.000	2178.000	20.799	71.689
6	222.000	255	255	255	53.698	19.313	100	4345.000	2212.000	21.251	15.000
7	372.000	255	255	255	70.770	24.698	100	17.000	3123.000	21.371	20.000
8	391.000	255	255	255	73.941	26.926	100	2966.000	1670.000	21.801	19.000
9	331.000	255	255	255	65.941	23.770	100	1935.000	2942.000	22.249	18.000
10	81495.000	255	255	255	4029.230	616.416	100	3962.000	2259.000	27.854	295.201
11	405.000	255	255	255	77.497	30.017	100	2250.000	3080.000	29.982	17.788
12	637.000	255	255	255	98.083	35.847	100	3732.000	1946.000	30.141	25.991
13	12900.000	255	255	255	437.144	139.086	100	836.000	1313.000	31.176	122.076
14	19845.000	255	255	255	1079.242	207.473	100	1244.000	1336.000	33.001	176.821
15	1806.000	255	255	255	161.054	56.859	100	2384.000	122.000	34.249	43.000
16	4973.000	255	255	255	381.605	141.241	100	848.000	191.000	35.491	66.688
17	3281.000	255	255	255	220.995	72.801	100	2979.000	1142.000	37.185	63.864
18	4667.000	255	255	255	512.985	216.541	100	248.000	641.000	47.246	55.156
19	23455.000	255	255	255	1110.916	361.168	100	327.000	964.000	48.142	156.835
20	8045.000	255	255	255	379.220	137.441	100	2313.000	296.000	48.540	90.894
21	891.000	255	255	255	120.912	47.508	100	0.000	2626.000	49.268	30.231
22	1613.000	255	255	255	152.225	50.606	100	4668.000	782.000	52.224	42.000
23	3757.000	255	255	255	453.245	143.003	100	3389.000	1859.000	53.531	78.605
24	1753.000	255	255	255	156.468	51.614	100	3873.000	99.000	54.462	46.000

Figure 3.25 Results window

3.3.1.3. 3D Image Analysis with Matlab

According to the work plan of this study, after 2D surface analyses, 3D analysis is conducted for cubic specimens. A new method to scan the surfaces of the concrete specimens was developed at the “IYTE Department of Electrical and Electronics

Engineering.” Further information about the method can be found in the report of Mehmet Çalı (Çalı, 2019). Method was implemented for the scanning of the concrete surfaces. The focus was the extracting the depth information precisely by using the calibrated stereo images from the left and right lens of the stereo camera. For operation, the same image acquisition system with a different lens (stereo lens) is used. Stereo images are obtained. The sample pair of images is shown in Figure 3.26.

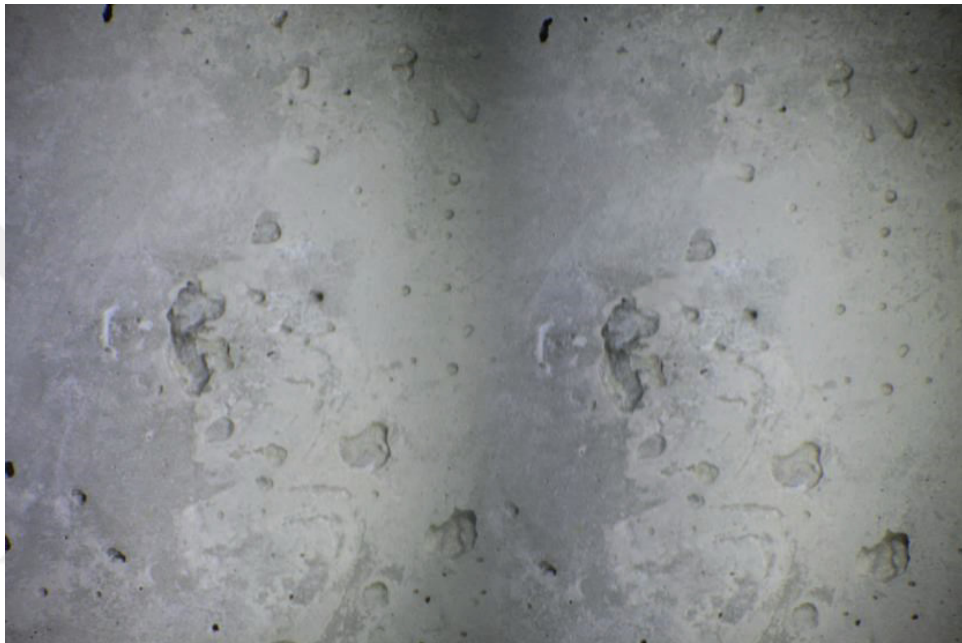


Figure 3.26 Unrectified stereo image for D4LO45 3rd illumination case

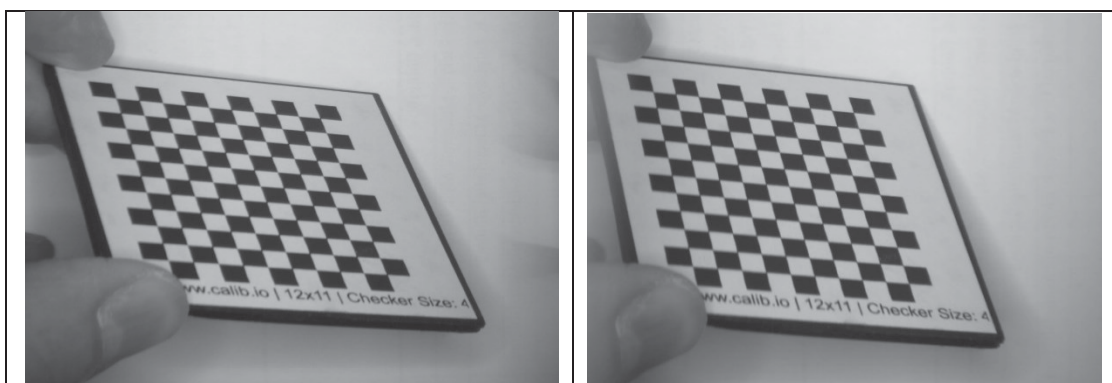


Figure 3.27 Third illumination case left and right view

The calibration process is followed by using a calibration board. Sixteen images were taken (8 right 8 left). 3rd pair of the image is illustrated in Figure 3.26. Left and right views from the camera are obtained, and the stereo image is split into two parts. Original images RGB is converted to 8 bit. After rectification, using calibration data, results images, (rectified images) are obtained as shown in Figure 3.27.

The structural similarity index method (SSIM) is used. Multiple illumination case is used in this method. Sixteen rectified images helped to obtain a 3D point cloud.

SSIM method, described by Fei et al. (Fei et al., 2017), is a relatively new approach to construct 3D data from extract data from multiple stereo images. The technique uses the same procedure with human eye vision. Depth information is calculated using the difference in the location of an object from two different images from two different cameras. Figure 3.27 shows the rectified images of 1st illumination case from the right and left cameras of D4LO45.

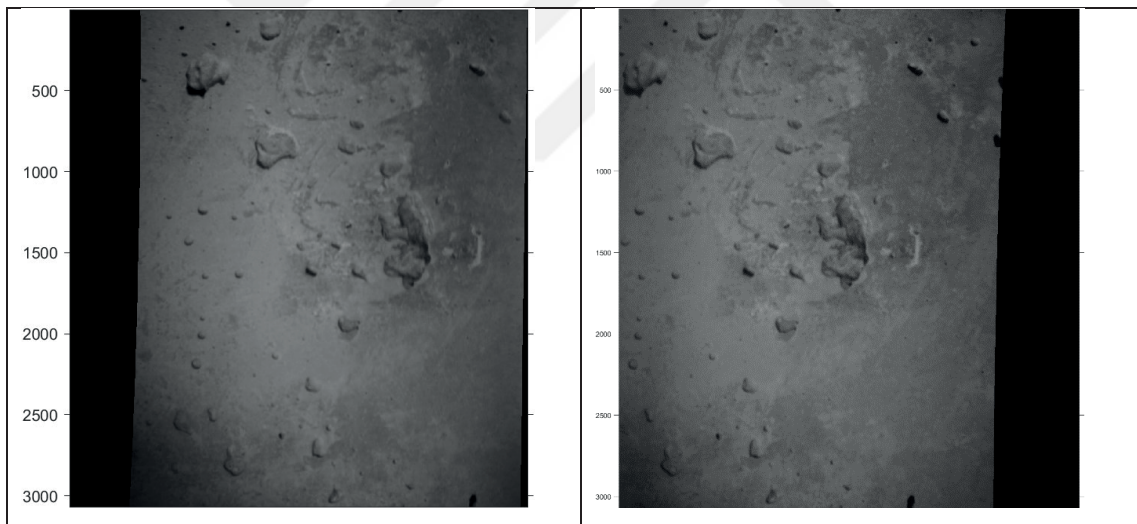


Figure 3.28 Rectified images

Distance from the camera to the surface of the scanned specimen is chosen as 280mm – 310mm and specified as search region. The disparity map is obtained with the disparity map function, and the disparity value is obtained 0.6103 in Figure 3.29.

The disparity map is generated from the illumination difference of right and left cameras. 3D points are given on Figure 3.30, and 3D background is shown on Figure 3.30. Background data is illustrated in Figure 3.32.

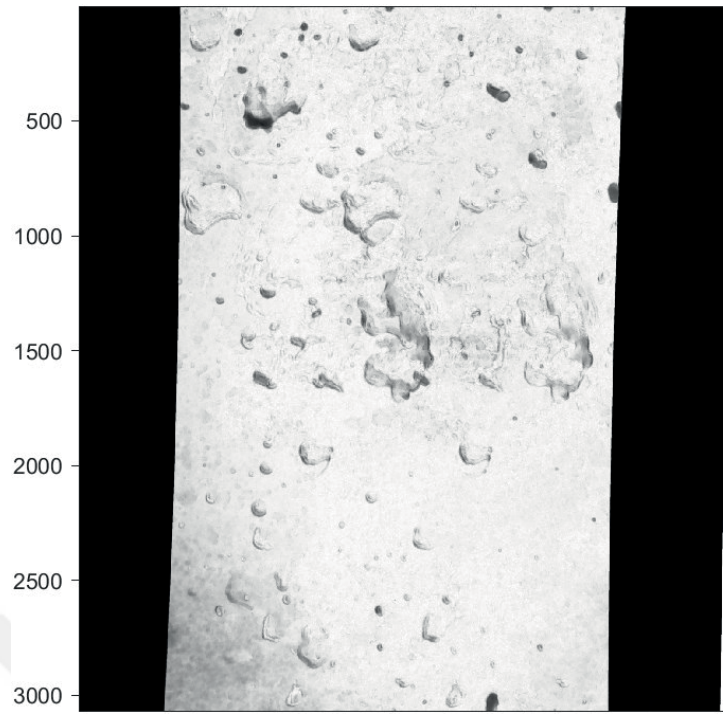


Figure 3.29 1st illumination case disparity map (surface of D4LO45)

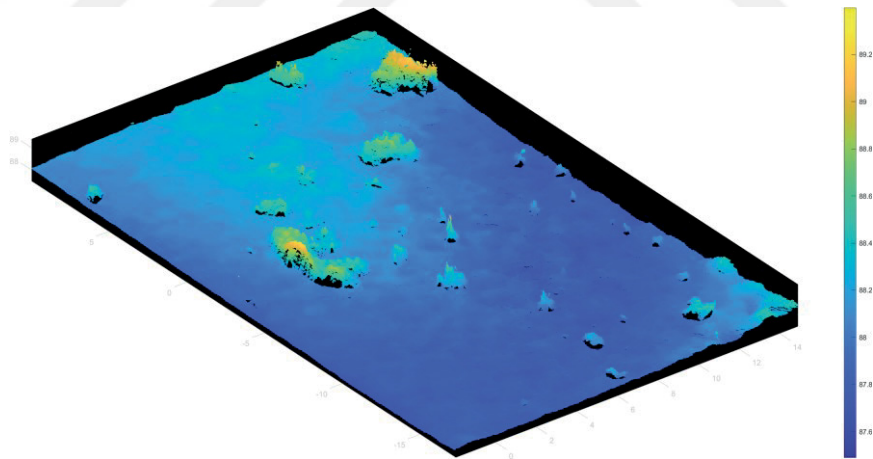


Figure 3.30 Points 3D (surface of D4LO45)

Figure 3.31, images and point data were extracted from the disparity map and the disparity map vector. Depth information was used with the cavity data obtained from the previous 2D analysis. By extracting the background point data from the depth map, volumetric info was obtained.

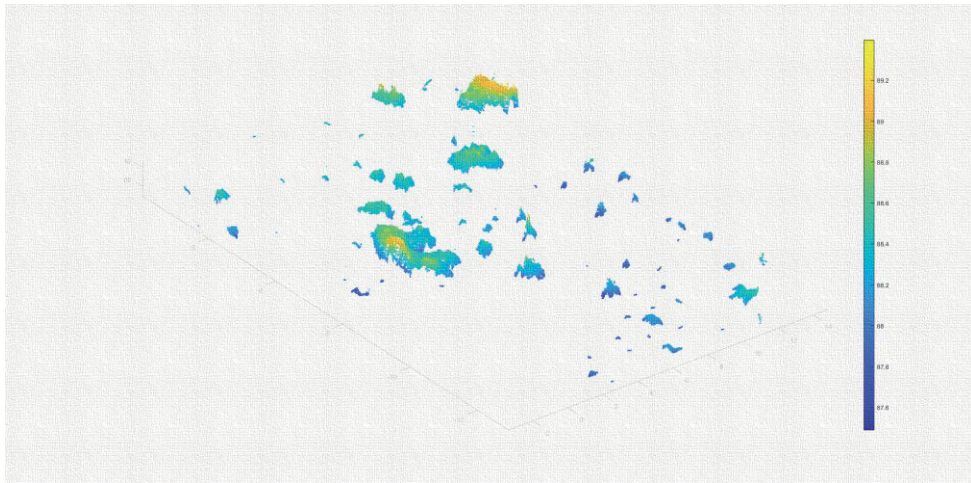


Figure 3.31 3D Cavities (for so-called D4LO45 concrete)

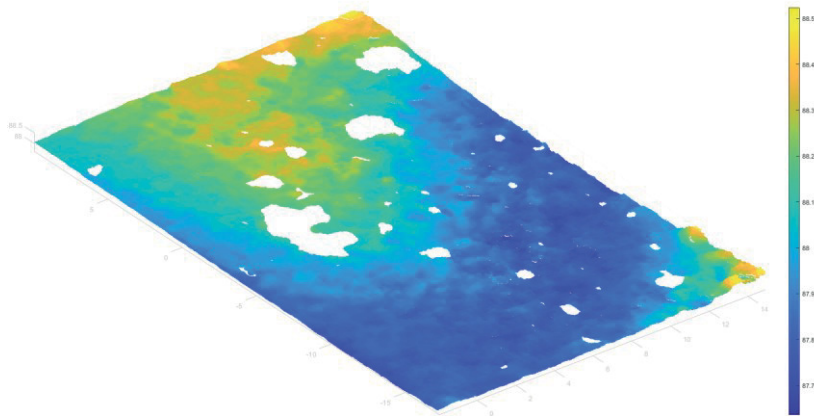


Figure 3.32 3D background (for so-called D4LO45 concrete)

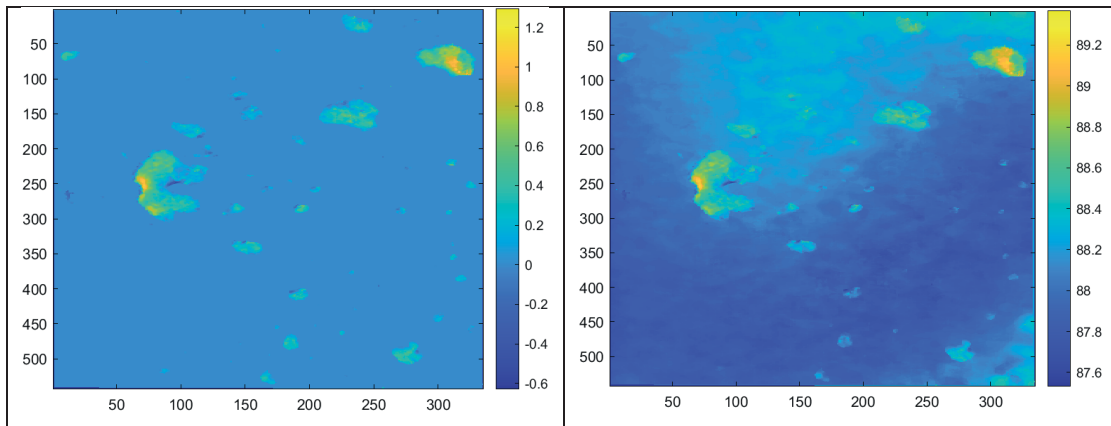


Figure 3.33 2D depth map (for so-called D4LO45 concrete)

For the example concrete (so-called D4LO45 concrete) surface, volume was calculated as 8 mm^3 and 2D depth maps are illustrated in Figure 3.23. Four different steps were covered in the process of computing the volume in this section. To help and visualize, a flow chart is generated in Figure 3.34. Example depth maps for other surfaces is given in Appendix C.

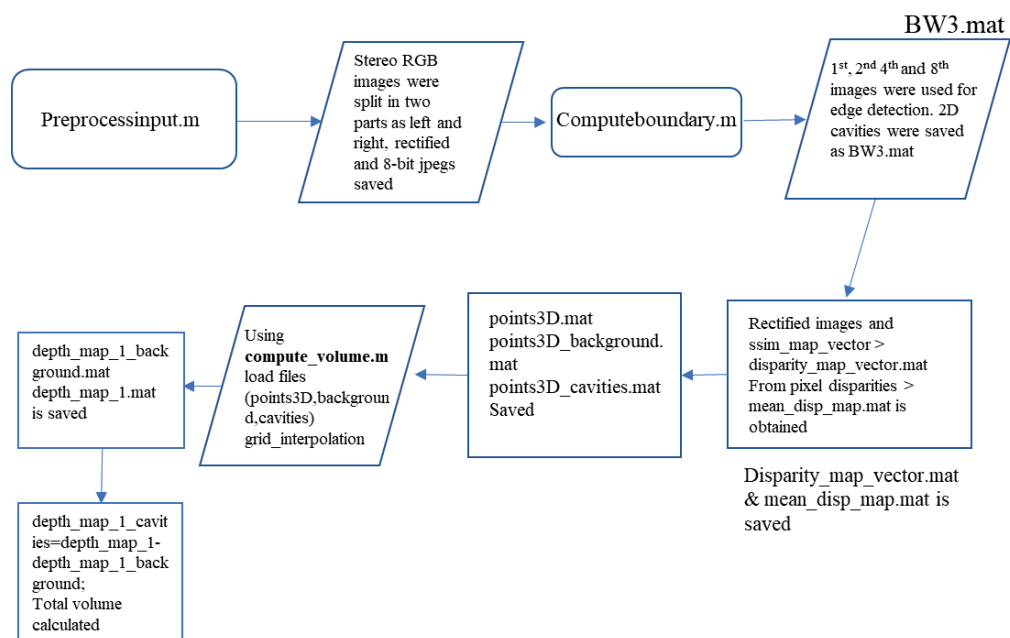


Figure 3.34 Flow chart for Matlab analysis

3.3.2. Bi-surface Shear Test

The loading setup for the test is shown in Figure 3.35. Cubic specimens were filled in two layers. 2/3 of the mold was filled as the first layer. After a definite duration (45 and 90 minutes for this study), the remaining 1/3 was introduced to the mold. With the help of three steel pieces (with $t=15\text{mm}$, $w=50\text{mm}$ and $l=150\text{mm}$), compressive force that will create shear on the interlayer surface was applied. 2 KN/s was selected as loading speed (Momayez et al. 2004; Megid and Khayat., 2017).

The bond strength was obtained by dividing the maximum load at failure by the bond area. Equation is given in equation (3.5).

$$\sigma = P/2A_{Fracture\ Plane} \quad (3.5)$$

σ = Splitting tensile strength (MPa)

P = Applied load

A = Area of the fracture surface in mm^2

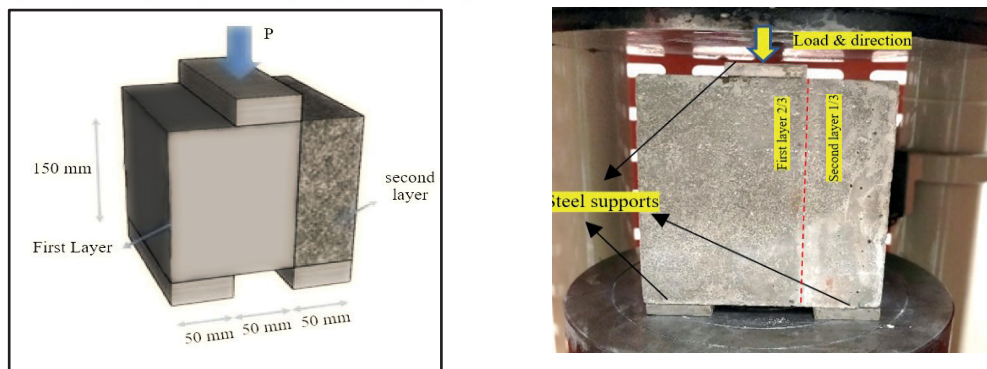


Figure 3.35 Bi-surface Shear loading

3.3.3. Slant Shear Test

The slant shear test was carried out according to ASTM C 882 (ASTM, 2013) . The test measures the shear bond between the existing concrete and the new concrete at an angle of 30° (Figure 3.36). Specimens size was selected as $10*20\text{ cm}$ cylinder.

Fracture plane area (A) was noted as 90.69 cm² for cylinder specimens. The bond strength was determined at the diagonal face by testing the composite specimen in compression (Nagaonkar and Bhusari 2014). Bond strength for slant shear was calculated by dividing the maximum load at the failure by the bond area; slanted surface for this test is given in equation (3.6) (Momayez et al. 2005).

$$\sigma = P/A_{Fracture\ Plane} \quad (3.6)$$

σ = Splitting tensile strength (MPa)

P= Applied load

A= Area of the fracture surface in mm²

The preparation of the specimens was described in section 3.3.7.

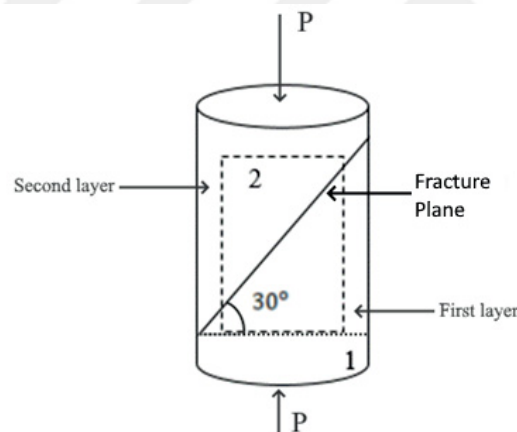


Figure 3.36 Slant Shear Test

3.3.4. Ultrasonic Pulse Velocity Test

Ultrasonic pulse velocity is a non-destructive test that can be applied to concrete samples and diagnose concrete quality indirectly. Without damaging or destroying, estimation of the compressive strength is possible with non-destructive testing by assessing the velocity of the transmitted pulse (Neville, 1995).

The test method ensures information about the denseness of the concrete specimen. The equipment generates an ultrasonic pulse with a frequency of 56 kHz and

calculates the transit time for transmitting the transducer across the sample to the receiving transducer by presenting it in the form of three digits on the screen. The transmitter transforms the electrical pulse into mechanical ones, which are later transformed into an electrical pulse by the receiver.

As stated in the instruction manual (CNS Farnell, n.d.), several defects and conditions can be tested with ultrasonic pulses in concrete. The time of the transmitted pulse is related to concrete density. Moreover, for solid concrete, travel time would be the shortest. Similarly, the duration would be longer for porous, honeycombed concrete, for instance. Separated pulse as it transmits through the neighboring parts, travel distance and travel time is longer for pulse though a reduced pulse velocity will be obtained in this situation. The pulse will not be able to travel beyond a crack because of the concrete air interface in the lowermost case; travel time is not detectable.

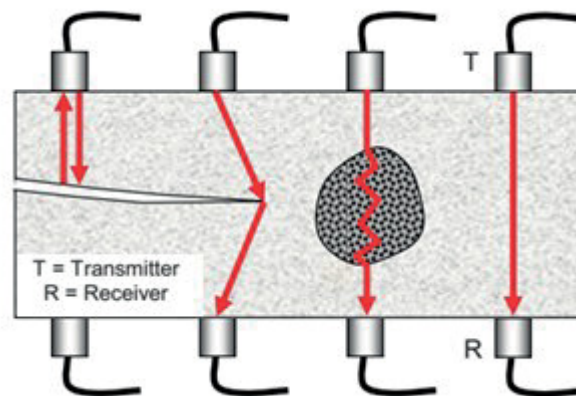


Figure 3.37 Different cases of pulse transmission (CNS Farnell, n.d.)

As shown in Figure 3.37, transmitter and receiver positions were placed in a direct transmission arrangement. Four different cases for a specimen is investigated. The transmission of the signal above the cold joint takes time “ t ” with no signal loss. A signal through the cold joint can be made, showing that the transmission time can become much longer than t , and a part or all the signal is lost. Portable ultrasonic transit time (in μs) is recorded for all specimens. Pulse velocity is calculated according to equation (3.7) (ASTM C 597-09, 2010) :

$$\text{Pulse velocity} = \frac{\text{Path length}}{\text{Transit time}} \quad (3.7)$$

Table 3.6 Classification of concrete (Neville, 1995)

Longitudinal pulse km/s	Quality of concrete
>4.5	Excellent
3.5-4.5	Good
3.0-3.5	Doubtful
2.0-3.0	Poor
<2.0	Very poor

The test was conducted according to ASTM C-597 (ASTM, 2010). Pundit 6 type equipment calibrated by using the calibration rod. For direct transmission, transducers were placed on opposite faces of the specimen. Classification of concrete samples according to longitudinal pulse can be seen in Table 3.6

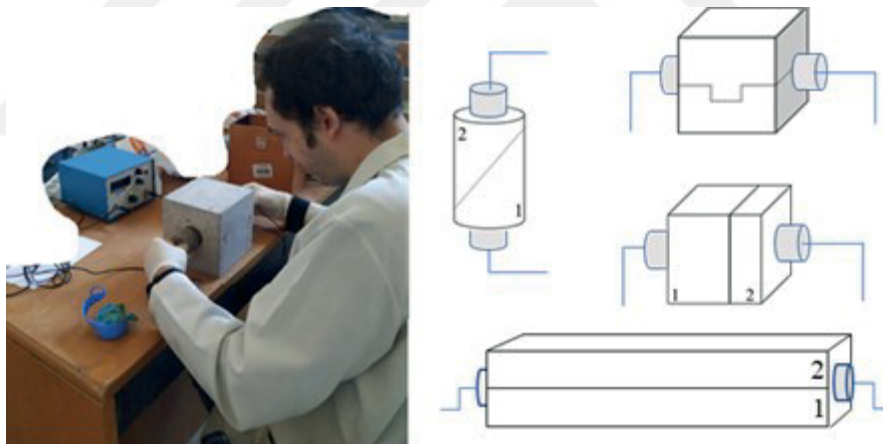


Figure 3.38 UPV testing (left), transducer positions (right)

The specimens were placed between transducers. Grease oil was used to ensure the perfect contact between the transducers and the concrete surface. The value was read from the LCD screen of the device with an accuracy $\pm 0.1\mu\text{s}$ and was noted. The same procedure was repeated for all specimens. Operation is shown in Figure 3.38. Testing of the layered specimens are also shown on the same Figure 3.38 (right).

3.3.5. Pull-off Testing

Pull-off test method was carried out according to (ASTM C1583, 2013). Adhesion between the first and second layer (or overlay and the substrate concrete) is tested by fixing a loading disk to the surface of the concrete upper layer. The test method has been designed to determine the in-situ tensile strength of specimens by applying a tensile load axially (Bungey and Grantham, 2006).

By using a core-drilling machine, four locations of the 60*15 cm beams were cut until a depth of 8 cm by partial coring (Figure 3.39). Two halves of the depth belong to first and second layers. The second layers belonged to delay periods of 45 and 90 minutes. A disk is bonded with an epoxy compound adhesive to the upper part of the concrete and pulled off to determine the force needed to break up a piece from the surface concrete. The force applied to the loading fixture is then progressively and smoothly increased. Failure occurs, and specimen breaks from the four possible weakest plane within the system as shown in Figure 3.40 (Bonaldo et al., 2005).

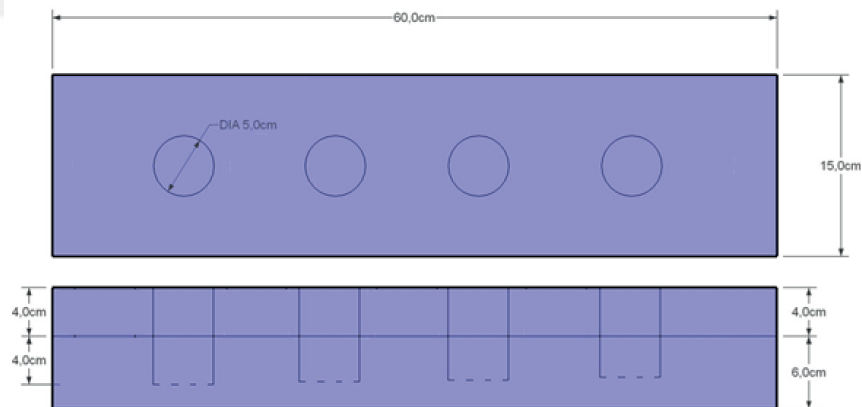


Figure 3.39 Partially drilled specimens and locations

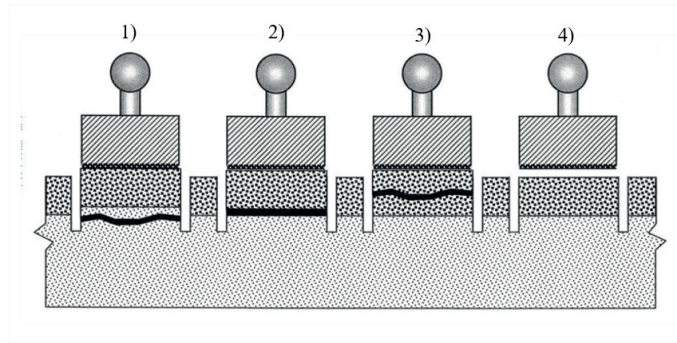


Figure 3.40 Illustration of Failure Modes (ASTM C1583, 2013)

Four different break situations are illustrated in Figure 3.40 as described in ASTM C1583 (ASTM C1583, 2013). The first failure mode occurs in the first layer. The second failure mode occurs at the concrete overlay interface. The third situation occurs in the overlay section. The fourth failure appears at the epoxy adhesive/overlay interface. Figure 3.41 shows the experimental steps. Thirty-six drilled specimens were tested under tensile force. Results are given in the next section.

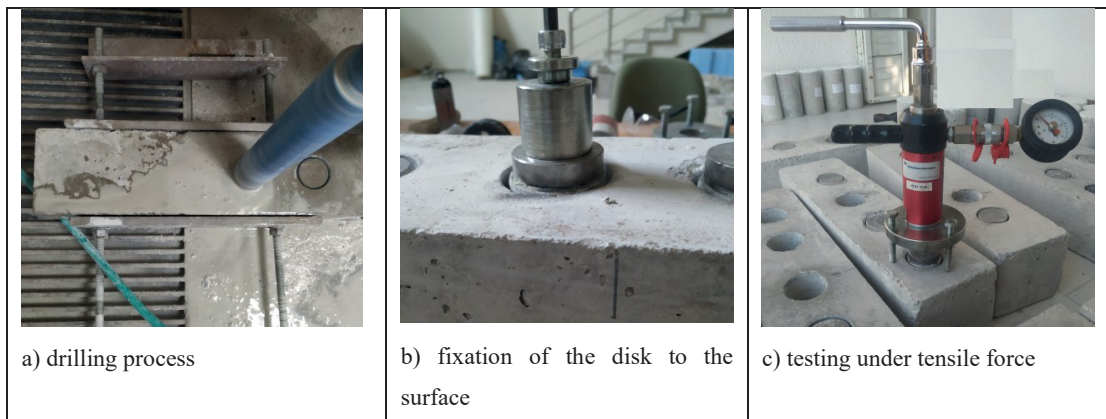


Figure 3.41 Experimental steps

3.3.6. Compressive Strength

Compression tests were carried out with 200-ton capacity hydraulic concrete press. The loading rate was 3 KN/s. Three 15x15x15 cm cubic specimens were tested for each mixture at 28 days. During this period, the specimens were cured underwater at $(23 \pm 2 \text{ } ^\circ \text{C})$ (Ersöz, 2012).

3.3.7. Preparation of the Specimens

Plywood frames were produced for this study. Geometry of the frames were picked to create a surface roughness between layers. Figure 3.42 show the designs of the frames. Weight of the frames were measured as 230, 280, 305, 415, and 200 grams for D1, D2, D3, D4 and D5, respectively. Dimensions of the frames is given in Figure 3.43.

Cubic specimens: First, 15cm*15cm*15cm cubic specimens were prepared. These specimens were cast monolithically or in layers. In the case of layered cubic specimens, the first layer was placed and then wooden frames having different shapes were kept on the first layer for 45 or 90 minutes. Then, the frames were removed, and the second layer was placed on the first layer having a definite shape (Figure 3.44) to fill the cubes.

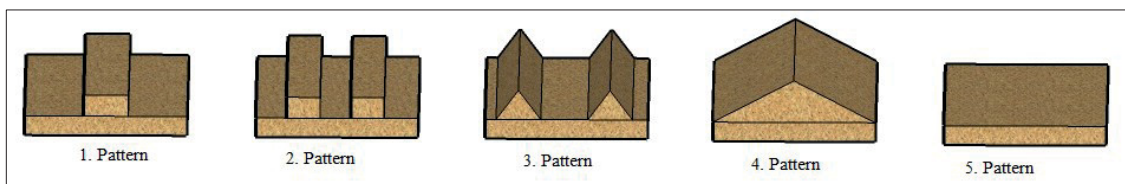


Figure 3.42 Applied patterns

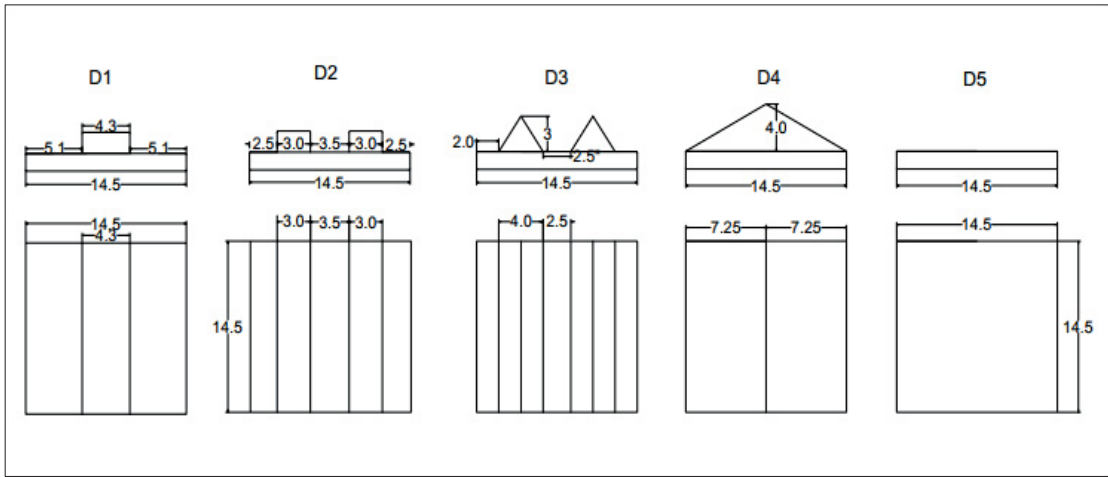


Figure 3.43 Dimension of patterns in cm

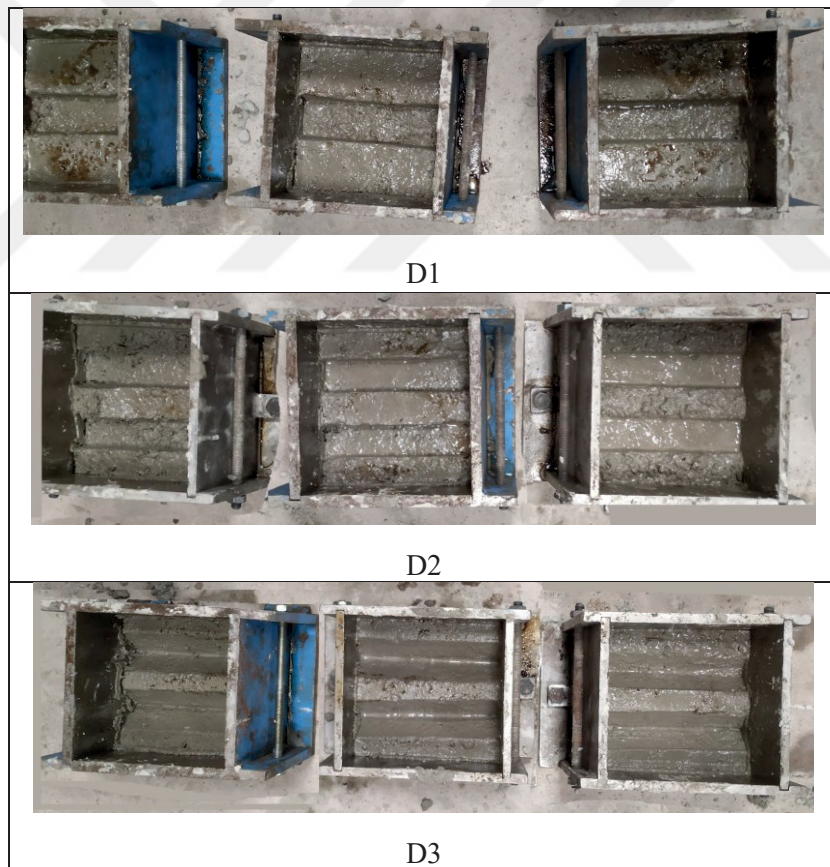


Figure 3.44 First layer of the cubic samples (for mid-thixotropy level)

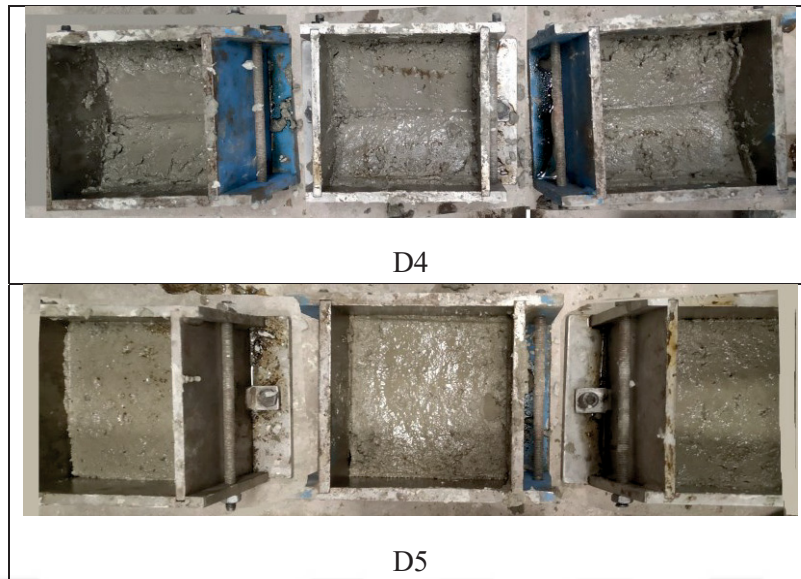


Figure 3.44a - (continue) First layer of the cubic samples (for mid-thixotropy level)

Cylindrical specimens: Cylindrical specimens with 10 cm diameter and 20 cm height were prepared for every batch of concrete. Three monolithic specimens were prepared with a single shot. For the layered specimens, three specimens were allowed to rest for 45 or 90 min in inclined position (Figure 3.45) and then the second layer was cast.



Figure 3.45 Slant Shear specimens

Bi-surface shear specimens: Again, 15-cm cubic specimens were used. The layers were formed by use of a 5-cm thick separator vertically. Firstly, the concrete is placed

while the separator was standing (Figure 3.45). After 45 or 90 minutes, the separator was removed, and the rest of the cube was filled. The first layer has a width of 10 cm while the second layer has a width of 5 cm.

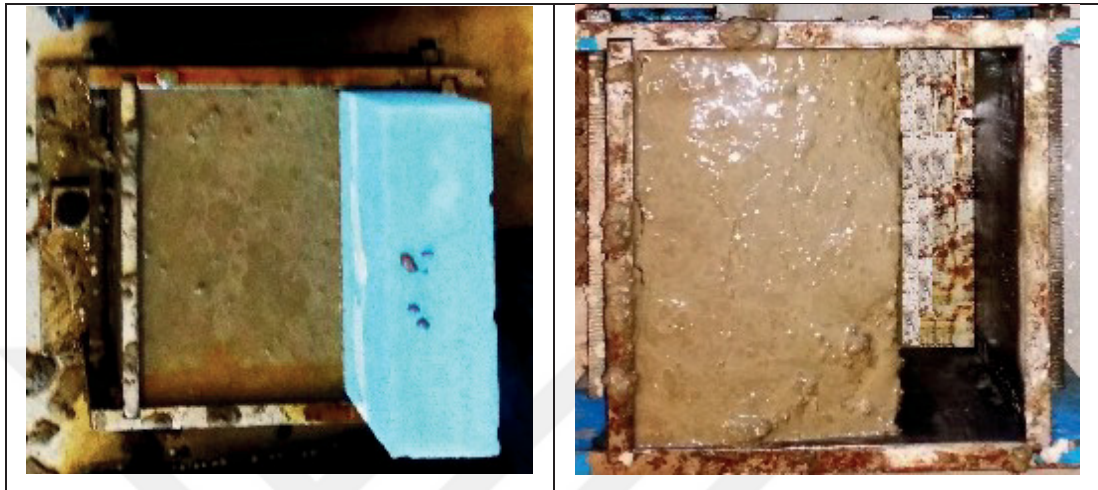


Figure 3.46 Bi-surface Shear specimens

Table 3.7 Specimen counts and dimensions

Level of Thixotropy	Application of pattern/test purpose	Delay time	Specimen type	Number #	
Low, Mid, High	D1, D2, D3, D4, D5	45 and 90 min	15 cm cubic specimen	90	
	Monolithic specimens	0 min		9	
	Bi-surface shear	45 and 90 min		18	
	Slant Shear		45 and 90 min	10*20 cm cylinder	18
			0 min		9
	Pull-off		45 and 90 min	15*60 cm prismatic specimen	6
			0 min		3

Beam specimens: A prismatic mold with 60 cm length and 15 cm*15 cm cross-section was used. The first layer was placed to have a thickness of 6 cm. The second layer

was placed after 45 or 90 minutes with a thickness of 4 cm. Beam specimens were used for pull-off testing. The types and the number of specimens for each test type are listed in Table 3.7.

3.3.8. Surface Properties

Four factors were selected as the output: Area Fraction void count and void area and the average of ten largest points for 2D scanning part. After the scanning of lateral surfaces of the specimen's 2D image processing steps were applied with Image-J. Several types of surface data were obtained. Count of voids, total void area, average size, area fraction. Average of the two lateral surfaces were taken. Two surfaces were picked to distinguish the difference between patterns. Surfaces were picked to Void count, area fraction, and the average area size of voids are picked for graphics and to obtain and compare results.

Cubic specimens were prepared for the direct- bi surface tests and analyzed. Cylinder specimens were prepared for the slant shear test previously. 15*60 cm beams were also prepared previously for pull-off testing.

3.3.9. Surface Scanning Procedure

The surface scanning procedure is explained in this section. Briefly, images were captured of the specimens and analyzed. The scanning procedure of the cubic specimens are shown in Figure 3.47. In determining the surface properties, two of four lateral surfaces of the cubic specimens which are in contact with the mold were scanned. Top and bottom surfaces were ignored. No extra labelling was made. Since the specimens did not have exactly the same surface areas, a so-called area-fraction term was defined and given in equation 3.8 to obtain accurate and comparable results. Area fraction is given in equation (3.9), and can be stated as "The percentage of pixels in the image or selection that have been highlighted in black":

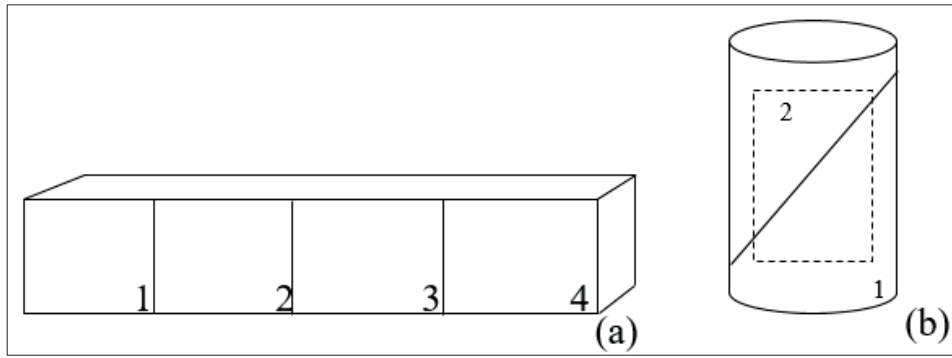


Figure 3.47 (a) beam specimens (b) cylinder specimens

$$\text{Area Fraction} = \frac{\text{Total void area}}{\text{Overall investigation area}} \quad (3.9)$$

Figure 3.47 shows the scanning technique for the specimens other than 15*15 cm cube. Surfaces were split into four areas (1,2,3,4), and images were captured for the beam to compare results easier. Similarly, for cylinder specimens, the curvature of the surface made the capturing process harder. Because of this, as seen in Figure 3.47, the dashed area was captured to minimize the curve effect.

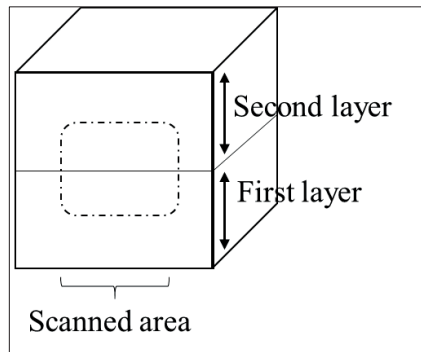


Figure 3.48 Specimen Scanning Procedure

CHAPTER 4

RESULTS AND DISCUSSION

4.1. Fresh Concrete Tests

In this study, 15 SCC mixtures were prepared in the first step and the basic fresh properties were determined. In addition to the rheological parameters, thixotropy was determined just after casting the concretes and after delay periods of 45 and 90 minutes. Thixotropic and rheological parameters were investigated, and three of the 15 mixtures were selected for testing the hardened concretes which were cast to have varying delay time and interlayer patterns.

4.1.1. V- funnel and T50 Durations

The V-funnel results of the concretes produced in this work are presented in Table 4.1.

Table 4.1 V-funnel and T50 durations

Slump Flow	Notation	V-funnel duration (s)	T ₅₀ duration (s)	Slump Flow	Notation	V-funnel duration (s)	T ₅₀ duration (s)
60 cm	46/50/60	6.00	0.70	70 cm	46/50/70	2.60	1.50
	46/55/60	3.80	1.00		46/55/70	2.60	0.80
					46/45/70	4.22	0.70
	41/45/60	39.25	2.00		41/45/70	2.64	0.80
	41/50/60	12.00	2.00		41/50/70	13.45	1.40
	41/55/60	5.50	1.00				
	36/45/60	45.00	2.50		36/45/70	45.00	1.34
					36/50/70	49.13	1.50
	36/55/60	6.00	8.00		36/55/70	3.70	1.32

Figure 4.1 shows the relation between w/c and V-funnel test results for different FA/TA when slump flow was 60 cm. A similar representation was also prepared for slump flow of 70 cm in Figure 4.2. It is clear from both figures that as w/c increases V-funnel durations decreases. Use of more water decreases the viscosity of the mixture and makes the flow more rapid hence decreases the V-funnel durations. The slowest durations occurred for 0.46 w/c ratio mixtures for both slump flow values.

The V-funnel durations were very close to each other when FA/TA was 0.55. This indicates that the effect of w/c on V-funnel is small for high fine aggregate content. Moreover, the shortest durations belong to the mixtures with high FA/TA ratio. This can be explained by the more friction between the coarse particles and their coagulation at the exit of the V-funnel when the mixture contains more amounts of coarse aggregate.

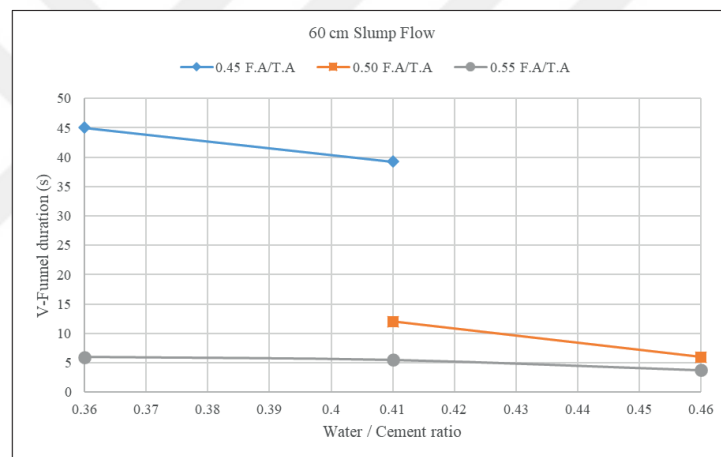


Figure 4.1 Change of V-funnel durations with w/c and FA/TA for 60 cm slump flow

When Figure 4.1 and Figure 4.2 are compared, it is seen that the V-funnel durations are longer for slump flow of 60 cm. Use of more superplasticizer to reach 70 cm slump flow, decreased the viscosity of the mixtures and decreased the V-funnel durations. All of the values varied in a close range for 60 cm slump flow. The range was more for 70 cm slump flow. This can be related to lower accuracy in measuring the fast flow of the mixtures with higher slump flow.

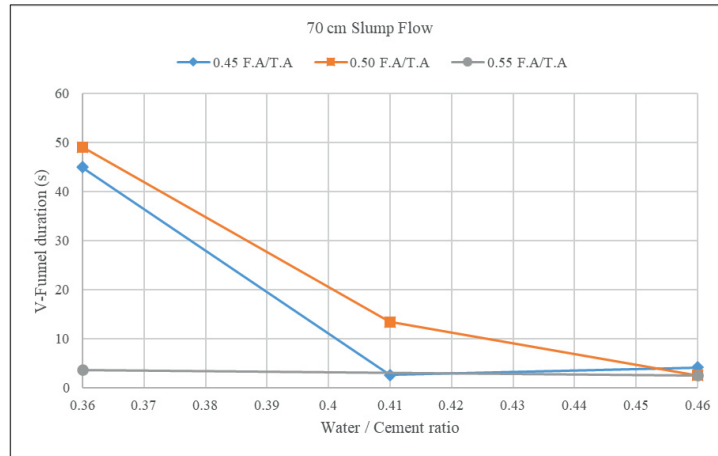


Figure 4.2 Change of V-funnel durations with w/c and FA/TA for 70 cm slump flow

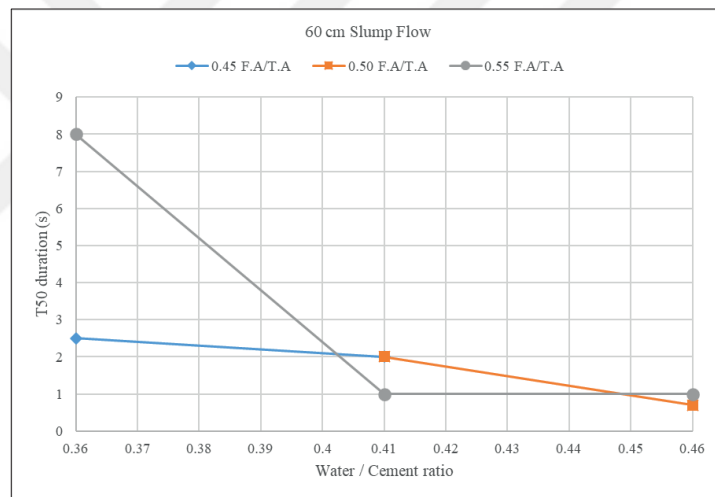


Figure 4.3 Change of T50 durations with w/c and FA/TA for 60 cm slump flow

Figure 4.3 and Figure 4.4 show the change of T50 durations with w/c and FA/TA for 60 and 70 cm slump flow values, respectively. Since both V-funnel and T50 durations indicate the viscosity of SCC mixtures, similar results were observed for these tests. Again, the T50 durations decreased with increasing w/c due to the decreased viscosity originating from the use of more water. The effect of F.A./T.A. on T50 was not so obvious since the durations for T50 test are much shorter and the accuracy becomes less for T50 results. the T50 durations were shorter for 70 cm slump flow as expected.

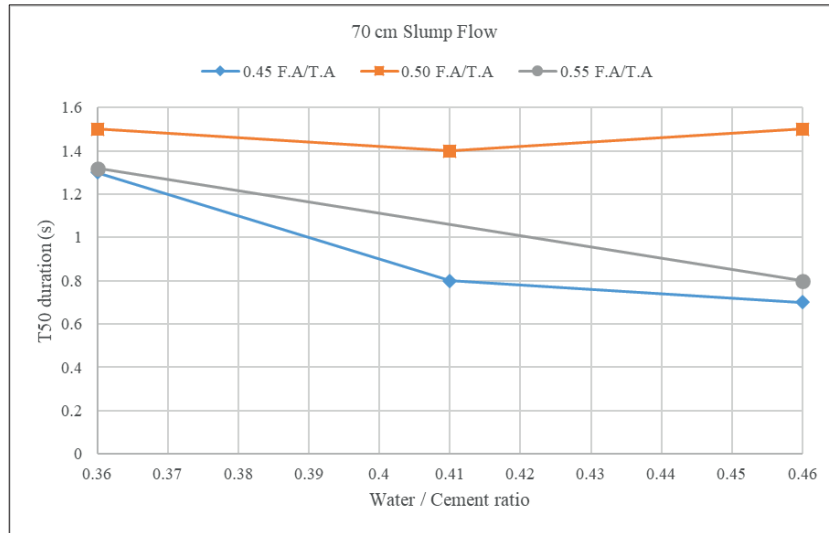


Figure 4.4 Change of T50 durations with w/c and FA/TA for 70 cm slump flow

4.1.2. VSI

Visual stability index was recorded for the mixtures. VSI values can be seen in Table 4.2. Higher coarse aggregate content may be the reason for low stability for only two of the mixtures (36/45/70 and 36/45/60). For the 46/50/70 mixture, higher w/c and higher slump flow affected the stability of the mixture.

Table 4.2 VSI values

Slump Flow	Notation	VSI	Slump Flow	Notation	VSI
60 cm	46/55/60	1	70 cm	46/55/70	1
	46/50/60	1		46/50/70	2
	-	-		46/45/70	1
	41/45/60	1		41/45/70	1
	41/50/60	2		41/50/70	0
	41/55/60	1		-	-
	36/45/60	2		36/45/70	2
	-	-		36/50/70	0
	36/55/60	1		36/55/70	1

4.1.3. Sieve Segregation Resistance

Static sieve segregation results are given in Table 4.3. Mixtures were investigated in two groups as 60 and 70 cm slump flow. Slightly higher results were obtained for the mixtures with 70 cm slump flow. Higher dosages of superplasticizers have led to higher segregation.

Table 4.3 Static Sieve Segregation results

Slump Flow	Notation	Segregation index	Slump Flow	Notation	Segregation index
60 cm	-		70 cm	46/45/70	1%
	46/50/60	0.10%		46/50/70	1.10%
	46/55/60	1%		46/55/70	1.50%
	41/45/60	0%		41/45/70	6%
	41/50/60	4%		41/50/70	2.10%
	41/55/60	0%		-	
	36/45/60	0.70%		36/45/70	0%
	-			36/50/70	0%
	36/55/60	1.60%		36/55/70	0.40%
	-				

All the mixtures are acceptable according to EFNARC (EFNARC 2005), since the threshold value for a recommended SCC is 10%.

4.1.4. Thixotropy

The change of thixotropy measured with yield value at rest method with w/c and FA/TA can be seen in Table 4.4. The results are also shown in Figure 4.5 and Figure 4.6 for slump flow values of 60 and 70 cm, respectively. Both figures indicate that there is a general tendency of decreasing effect of w/c on the thixotropy. The variation was less significant when FA/TA was 0.55. Higher water contents increased interparticle spacing making the thixotropic bonding more difficult.

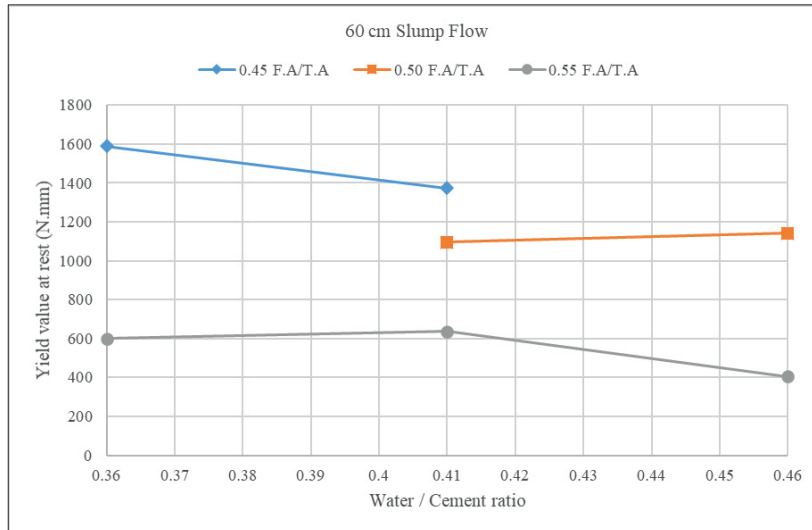


Figure 4.5 Change of thixotropy with w/c and FA/TA for 60 cm slump flow

For both slump flow values, the mixture with FA/TA=0.55 resulted in lower thixotropy levels. The increase in the coarse aggregate content caused an increase in the thixotropy as stated in previous study (Assaad, 2004). This is because the coarse aggregates have the tendency to show coagulation in the mixture, resulting an increase in the thixotropy (Erdem et al., 2009; Assaad et al., 2003).

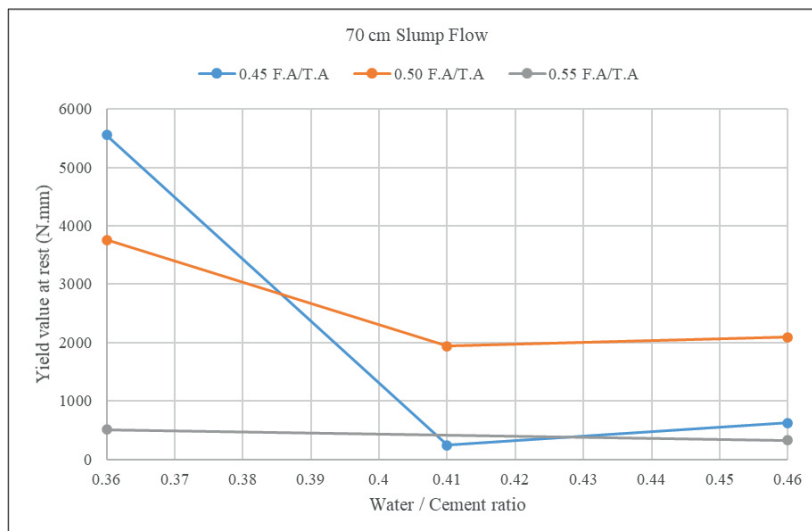


Figure 4.6 Change of thixotropy with w/c and FA/TA for 70 cm slump flow

After obtaining the thixotropy results, the mixtures with low, medium and high thixotropy were picked to make the hardened concrete tests because thixotropy is one of the most important parameters that can affect the interlayer bonding of the concretes. The lowest and highest values were identified for the low and high thixotropy levels. For the medium thixotropy, averages of the results were taken. According to this selection, the following mixtures were selected:

- Low thixotropy level: 41/45/70
- Medium thixotropy level: 41/50/60
- High thixotropy level: 36/45/70

Table 4.4 Thixotropy values

Notation Delay	Yield value at rest (N.mm)		
	0 min	45 min	90 min
36/45/60	1589	1839	1926
36/55/60	400	944	2802
41/45/60	1372	1926	1499
41/50/60	1096	2039	2147
41/55/60	637	2341	2460
46/50/60	1142	1370	1299
46/55/60	404	808	983
36/45/70	5558	6168	5338
36/50/70	3760	2440	4894
36/55/70	512	846	231
41/45/70	240	466	878
41/50/70	291	1407	1499
46/45/70	625	622	999
46/50/70	2089	4346	6526
46/55/70	324	952	1274

Box plot for YVR method is given in Figure 4.7. Box plots were prepared for 15 mixtures. Selected mixtures were marked on the graph. The results show that for the selected three concrete's low, medium, and high is accurate for this method.

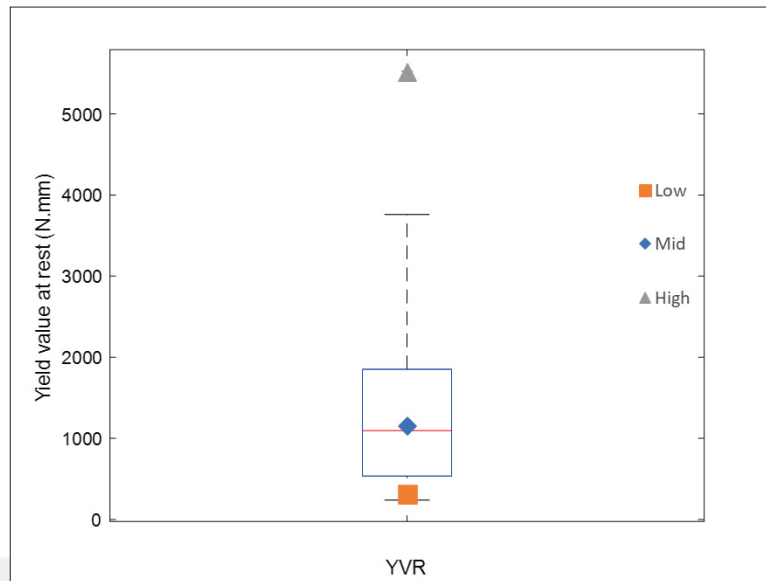


Figure 4.7 Box -whisker graph for YVR

Thixotropy is a time dependent characteristic of SCC and therefore the change of thixotropy with time was also investigated as shown in Table 4.4, Figure 4.8 and Figure 4.9. As seen, the thixotropy increased with time.

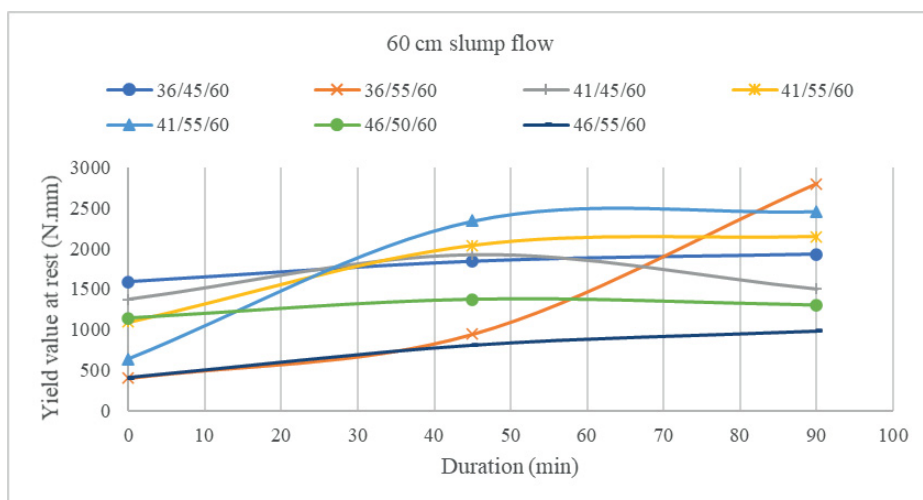


Figure 4.8 Change of thixotropy with duration (60 cm slump flow)

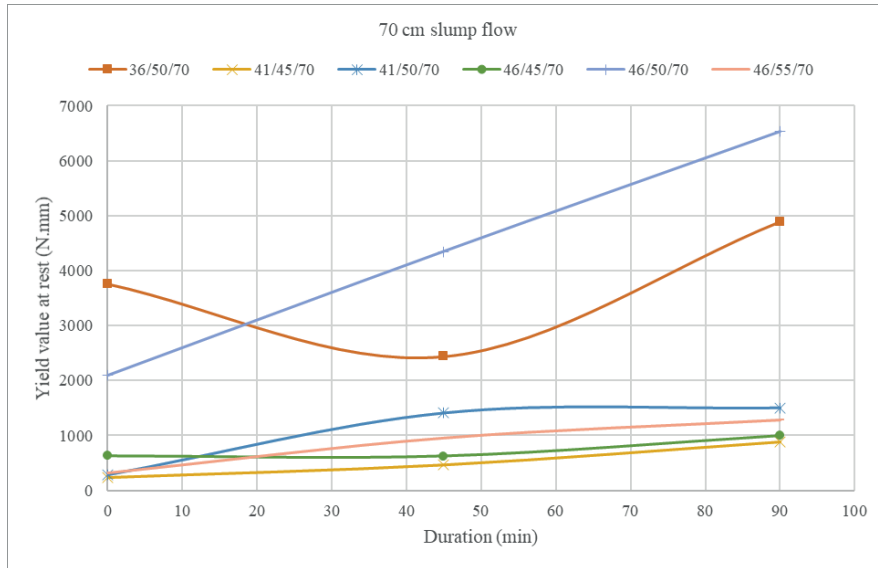


Figure 4.9 Change of thixotropy with duration (70 cm slump flow)

4.1.5. Rheology

The results of the rheology tests can be seen in Table 4.5.

Table 4.5 Rheology test results

Notation	Apparent yield stress (g), N.mm	Torque plastic viscosity (h), N.mm.s
36/55/60	5.01	1683.1
36/45/60	73.01	2556
41/45/60	103.59	2065
41/50/60	96.9	1109.8
41/55/60	101.8	1035.1
46/50/60	233.34	1196.6
46/55/60	27	459
36/45/70	1838	6577.7
36/50/70	278.61	4937
36/55/70	7.33	786
41/50/70	66.67	697.53
41/45/70	114.4	459.12
46/45/70	178.39	729
46/55/70	68	607.92
46/50/70	22.4	967.10

The change of apparent yield stress with w/c and FA/TA for 70 cm slump flow can be seen in Figure 4.10. It is clear from the figure that when the w/c increased from 0.36 to 0.41, apparent yield stress decreased significantly for the FA/TA ratios of 0.45 and 0.50. Higher water content in these mixtures separated the distance between the solids and reduced the internal friction and minimum stress required to initiate the flow. At w/c=0.41, the apparent yield stress was already very low and further increase in the w/c did not provide additional reduction in the apparent yield stress. The mixture with FA/TA=0.55 had very low apparent yield stress even at w/c of 0.36 and the increase in w/c did not affect the results further.

The apparent yield stress was higher when the coarse aggregate content was higher as seen in Figure 4.10 for all w/c ratios because the internal friction between the coarse particles to initiate the flow was higher. However, the effect of FA/TA was less pronounced beyond w/c ratio of 0.41 since all the values were very low and close to each other.

Table 4.5 shows that apparent yield stress values were lower for 70 cm slump flow as expected because as known, the effect of superplasticizers is mostly on the yield stress. The polycarboxylate based superplasticizer used in this study dispersed the cement particles and enhanced the flow.

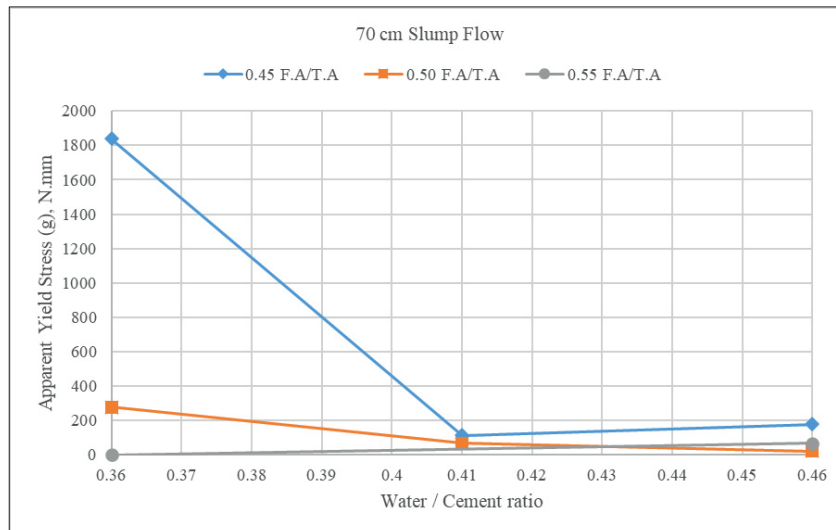


Figure 4.10 Change of apparent yield stress with w/c and FA/TA for 70 cm slump flow

Figure 4.11 and Figure 4.12 show the variation of torque plastic viscosity (T.P.V.) with w/c and FA/TA for different slump flow values. As expected, from the literature and from the V-funnel and T50 results, it can be said from these figures that the torque plastic viscosity decreased with increasing w/c especially for lower w/c. Moreover, the values are much lower for 70 cm slump flow when compared to 60 cm slump flow. Therefore, it can be concluded that the amount of superplasticizer is a major factor that affects the viscosity of the mixtures.

The effect of FA/TA was obvious when w/c changes from 0.36 to 0.41. However, when the w/c increased from 0.41 to 0.46, neither w/c nor FA/TA made a significant change especially for 70 cm slump flow. Nevertheless, for both slump flow values, the lowest torque plastic viscosity values were noted for FA/TA=0.55 mixtures. When the amount of coarse particles was less, there was less internal friction in the internal structure during the SCC flow.

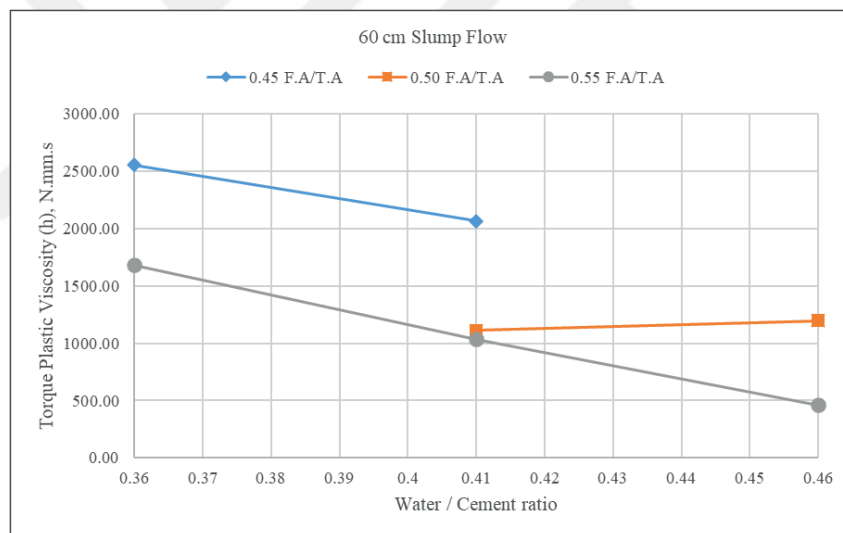


Figure 4.11 Change of T.P.V. with w/c and FA/TA for 60 cm slump flow

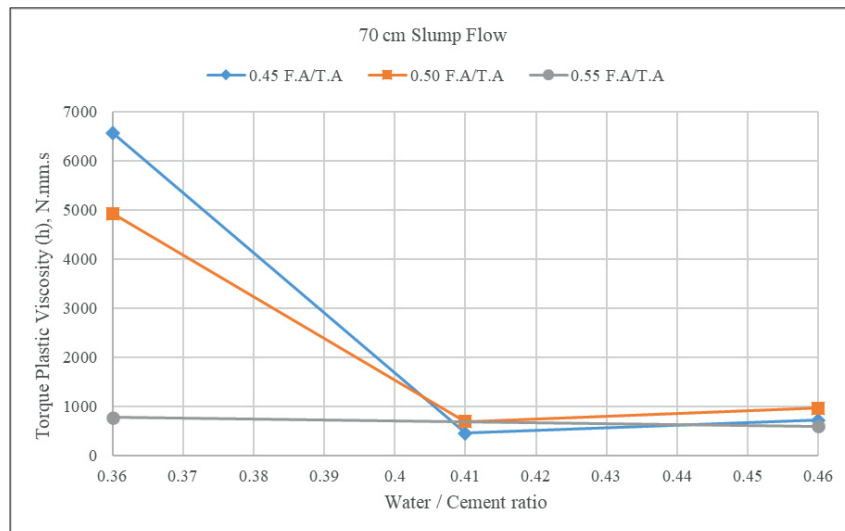


Figure 4.12 Change of T.P.V. with w/c and FA/TA for 70 cm slump flow

4.2. Hardened Concrete Tests

4.2.1. Compressive Strength

28-day compressive strength of the mixtures having monolithic specimens can be seen in Table 4.6. The mean and coefficient of variation (COV) values can also be seen in Table 4.6. The results showed that there is not a direct relation between the compressive strength and the mix design parameters except w/c ratio. Mixtures with the 0.36 w/c gave the highest compressive strengths (Table 4.6).

Table 4.6 Compressive strength test results

Mixture name	#1	#2	#3	St dev (Mpa)	COV	Mean Compressive strength (MPa)
36/45/60	52.47	50.44	50.32	1.21	0.02365	51.08
36/45/70	52.88	49.32	54.1	1.14	0.02217	51.62
36/50/70	51	56.9	49.6	3.87	0.07380	52.50
36/55/60	52.04	51.82	51.5	0.27	0.00524	51.79
41/50/60	45.03	45.1	46.79	1.00	0.02183	45.64
41/45/70	39.93	38.25	37.42	1.28	0.03319	38.53
41/45/60	47.41	46.63	47.97	0.67	0.01422	47.34
41/55/60	52.54	58.14	54.64	2.83	0.05134	55.11
46/45/70	46.49	45.76	47.19	0.72	0.01538	46.48
46/50/60	40.91	39.96	43.62	1.90	0.04577	41.50
46/55/70	45.59	47.85	47.02	1.14	0.02442	46.82
46/55/60	55.06	49.21	45.17	4.97	0.09982	49.81

From the literature (EFNARC, 2005), it is expected, SCC would have slightly higher compressive strength when compared to traditionally vibrated concrete.

As explained previously, three mixtures were selected for the further hardened concrete tests and layered specimens were produced with these mixtures. The notation for these mixtures is explained below:

D1, D2, D3, D4, D5 is the code for pattern name, (see section 3.3.7)

HI, LO, MID is the code for the thixotropy level for high, low and medium respectively.

45, 90 are the resting (delay) times in minutes for the casting between layers

Mono: Monolithically cast samples

SS: Slant shear specimens

DB: Bi-surface Shear specimens

K: Beams prepared for the pull-off specimens

The compressive strength of the layered specimens together with the monolithic specimens are tabulated in Table 4.7. Specimens were kept in water for 28 days and n kept at laboratory conditions for eight months.

The change of the strength with different patterns and delay times are also shown in Figure 4.13, Figure 4.14, and Table 4.7.

Table 4.7 Compressive Strength results (cubic)

Layer type	Thixotropy level	Delay time	Label	Mean compressive strength (MPa)	cov
Mono	Low	-	MONOLO	57.54	0.08538
	Medium		MONOMID	61.97	0.12173
	High		MONOHI	59.2	0.1175
D1	Low	45 min	D1LO45	55.81	0.11138
		90 min	D1LO90	65.91	0.0371
	Medium	45 min	D1MID45	68.61	0.02181
		90 min	D1MID90	64.22	0.07456
	High	45 min	D1HI45	65.45	0.0341
		90 min	D1HI90	69.33	0.01043
D2	Low	45 min	D2LO45	60.33	0.10485
		90 min	D2LO90	63.04	0.01907
	Medium	45 min	D2MID45	75.12	0.07022
		90 min	D2MID90	70.45	0.05486
	High	45 min	D2HI45	65.95	0.02054
		90 min	D2HI90	60.82	0.04622
D3	Low	45 min	D3LO45	57.74	0.0062
		90 min	D3LO90	63.81	0.02913
	Medium	45 min	D3MID45	73.71	0.03874
		90 min	D3MID90	66.63	0.01951
	High	45 min	D3HI45	66.01	0.01954
		90 min	D3HI90	65.44	0.0435
D4	Low	45 min	D4LO45	61.61	0.02168
		90 min	D4LO90	63.92	0.03712
	Medium	45 min	D4MID45	74.75	0.06532
		90 min	D4MID90	73.32	0.03766
	High	45 min	D4HI45	63.57	0.01525
		90 min	D4HI90	67.78	0.0025
D5	Low	45 min	D5LO45	59.95	0.02704
		90 min	D5LO90	57.75	0.03286
	Medium	45 min	D5MID45	62.2	0.06838
		90 min	D5MID90	67.85	0.11365
	High	45 min	D5HI45	63.77	0.01507
		90 min	D5HI90	65.26	0.00708

Several factors affected the compressive strength of the cubic specimens. Lowest compressive strength results were obtained for low thixotropy. Potential reasons can be the higher water content and lower viscosity of the mixture, which can show more segregation.

Although the mixture with medium thixotropy has higher w/c ratio than the one with high thixotropy, the compressive strengths of the medium thixotropy concrete were higher than the high thixotropy concretes for the layered specimens. This can be due to the fact that high thixotropy can cause a fast structuring in the lower layer and prevent a sufficient bonding with the subsequent layer.

Surface of first layer was changed with the shape of the pattern. From the literature there is a direct proportion between surface roughness and bond strength (Santos et al., 2007; Aysha et al. 2014; Momayez et al. 2005). In our study, geometrical patterns were used. The effect of pattern geometry was not significant for the compressive strength when compared to other factors like level of thixotropy and w/c ratio.

Another factor that affects the compressive strength is the air content of the mixture. There is an inverse proportion between compressive strength and air content of the mixtures. The application of wooden patterns may have facilitated the migration of air in the mixture. This can be the explanation of higher compressive strength results for 90 min delay when compared to 45 minutes for D1LO90, D3LO90, D4LO90, D1HI90, D4HI90.

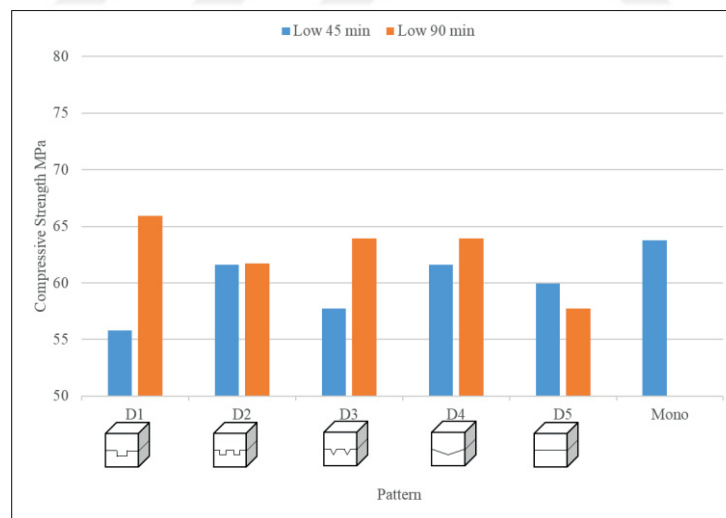


Figure 4.13 Compressive strength (for low thixotropy)

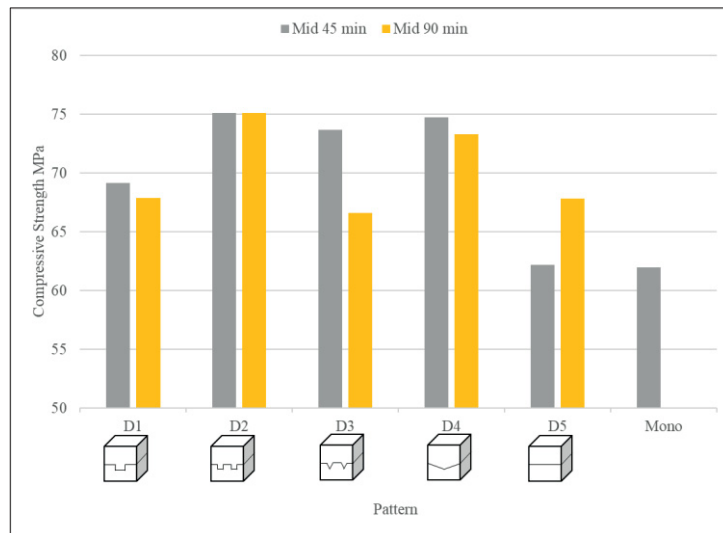


Figure 4.14 Compressive strength (for medium thixotropy)

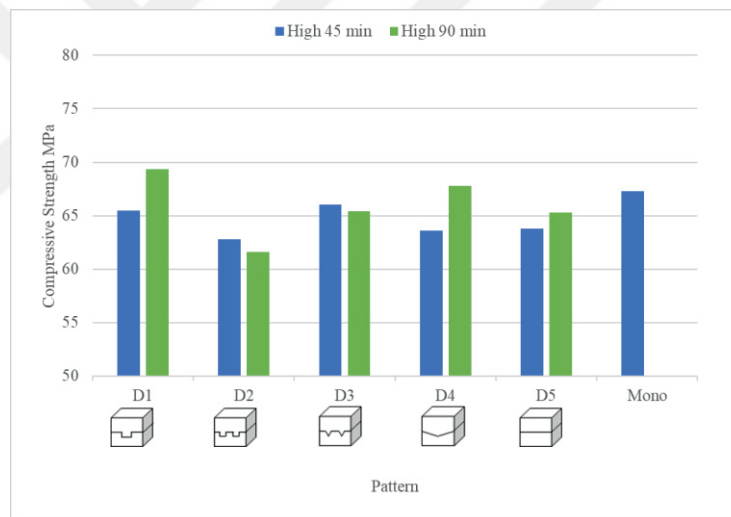


Figure 4.15 Compressive strength (for high thixotropy)

Some of the layered specimens resulted in higher strengths than monolithic specimens. This can be due to the pressure applied for placing the wooden frames. Moreover, the air in the lower layer has to travel a shorter distance to the surface, making a more dense structure when compared to monolithic specimens.

4.2.2. Slant Shear

The notation used for the slant shear test specimens can be described as follows: SS is the abbreviation for Slant shear. LO, MID, HI are the codes regarding the thixotropy level of the concrete for low, medium and high respectively. MONO means monolithically cast specimens. 45 and 90 corresponds to casting delay between layers, 45 minutes and 90 minutes, respectively. Slant shear test results are presented in Table 4.8 and Figure 4.16. Images for tested specimens are given in Appendix F.

The change of the results with the delay time and thixotropy is shown in Figure 4.16. As expected, low thixotropy and highest w/c ratio gave the lowest slant shear strength. Parallel to compressive strength results, higher water content (41/45/70) reduced the bond strength significantly.

Table 4.8 Slant Shear results

Thixotropy level	Delay (min)	Notation	Compressive strength (Mpa)	cov
Low	0	SSMONOLO	38.11	0.0948
	45	SSLO45	31.49	0.0779
	90	SSLO90	34.83	0.0703
Medium	0	SSMONOMID	43.57	0.0674
	45	SSMID45	39.85	0.0710
	90	SSMID90	40.70	0.3730
High	0	SSMONOHI	46.00	0.0189
	45	SSHI45	44.80	0.1058
	90	SSHI90	39.72	0.0551

The highest values were obtained for the specimens with high thixotropy. Lower w/c ratio and higher coarse particle content led better interlocking and increased roughness between layers.

The results for medium thixotropy and high thixotropy were close to each other, despite the lower w/c of the high thixotropy mixture. Similar to the discussion made for compressive strength results, relatively high thixotropy prevented the interlayer bonding.

On the other hand, the higher coarse aggregate content in the high thixotropy concrete can lead to better interlocking and increased roughness between the layers.

Considering the above discussions, the positive and negative factors seemed to balance each other and resulted in comparable slant shear test results.

Slant shear results were varied from 38.11 to 46 MPa for monolithically cast specimens. Strength loss after 45 minutes between layers was recorded as 11.3 %, 8.6%, 2.6% for low and mid and high thixotropy, respectively.

For the 90 minutes of delay between layers of concrete, Slant shear strength decreased 8.7% , 6.5% and 13.7% for low, mid and high respectively. Higher results were obtained for 90 min delay when compared to 45 min delay. SSMID45 and SSMID90 gave values close to each other. low stability and high water content of the mixture for SSLO45 resulted as possible segregation, created a weak zone between the interface of first and second layer and also weakened the interfacial transition zone between aggregate and cement paste. This may be the reason for inadequate strength gain for the specimens.

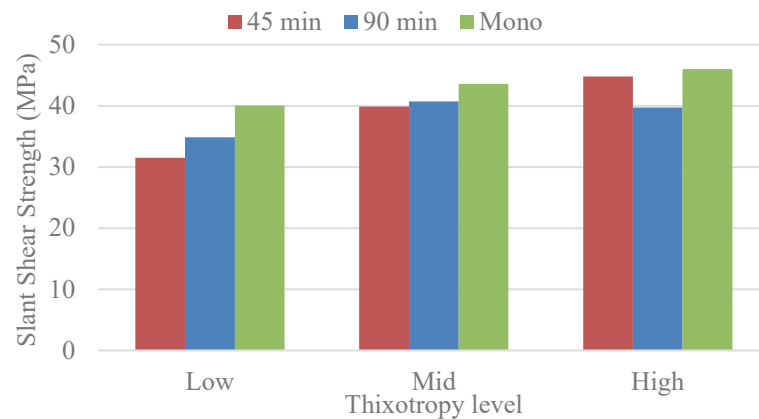


Figure 4.16 Slant Shear specimens bond strength change

Megid and Khayat (Megid and Khayat, 2017), reported values varying from 44.3 to 55.1 MPa for monolithic control samples of the slant shear test. Strength loss after 45 minutes between layers was reported as 7%, 8.3% and 34% for low, mid, and high thixotropy, respectively.

For this study, 7 % average COV varying from 2% to 10% was obtained for the slant shear test. Other studies (Momayez et al., 2004; Diab et al, 2017) reported the slant

shear test results with following COV values of 9.46% for Momayez, 5.82% for Diab et al.

4.2.3. Bi-surface Shear

Table 4.9 shows the results for the bi-surface shear test. Notation was as follow: DB is the B-surface shear, LO, MID, HI are the codes regarding the thixotropy level of the concrete for low, medium and high respectively.

Vertical joint was created between layers. The mechanism of the Bi-surface shear test is given in section 3.3.2. Thixotropy level and filling ability of the mixtures affected the results. Highest values were found with mid thixotropy level similarly to Slant shear method and lowest values were obtained for low thixotropy. 5% %17 and %18 strength loss was detected from 45 minutes to 90 minutes delay for low, mid and high thixotropy respectively. Partial loss of workability and high plasticity of the first layer reduced the bi-surface shear strength. Therefore, bond strength between layers is reduced for 90 minutes when compared to 45 minutes delay. Filling ability of the concrete affected the strength results. Moderate thixotropy level ensured good filling ability and moderate viscosity to give required stability.

Table 4.9 Bi-surface test results

Notation	COV	Compressive strength mean (Mpa)
DBLO45	0.02123	7.92
DBMID45	0.02603	9.70
DBHI45	0.12278	9.34
DBLO90	0.04925	7.63
DBMID90	0.04574	8.21
DBHI90	0.04769	8.29

Another factor affects the results is the roughness between layers. A smooth interface can lower the strength for the bi-surface shear test. Shear force, bending moment and tensile forces

between opposite surfaces of the specimen worked together for failure in this test. Images of a group of tested specimens is given in Appendix E.

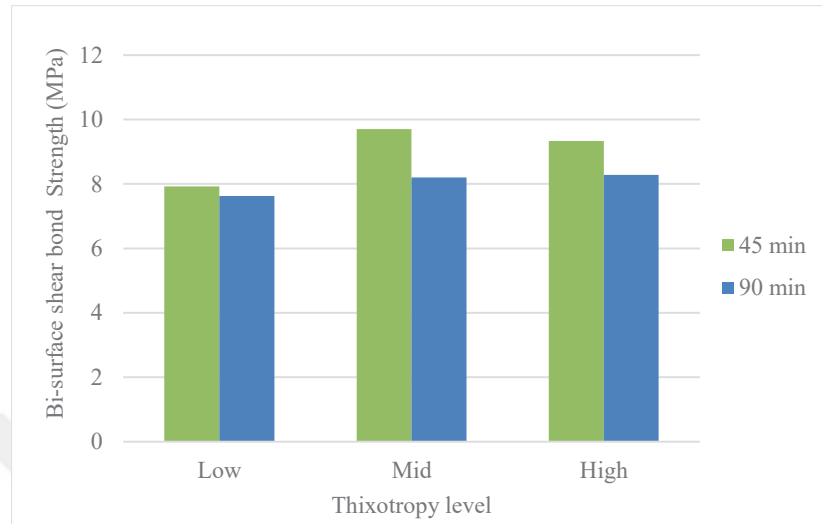


Figure 4.17 Bi-surface shear results

4.2.4. Pull-off Test

Figure 4.18 illustrates the results of the pull-off test. Drilled specimens were tested under tensile force. Thirty-two partially drilled specimens were tested. Table 4.10 and Figure 4.18 shows approximately 18% and 20% strength loss for the specimens prepared with low thixotropy with 45 and 90 minutes delay time, respectively.

Consistently, monolithically cast specimens gave the highest pull-off strength for three thixotropy levels. For 90 minutes of delay time, specimens prepared with high thixotropy, 4 % strength loss for 45 minutes between layers , 18% strength loss obtained when compared to monolithic specimens.

Since the tensile strength of the concrete is connected to compressive strength, highest values are expected from concretes with high compressive strength. High thixotropy and reduced segregation increased the strength aggregate-paste interface due to the low water content. Higher coarse aggregate ratio and surface texture of crushed limestone aggregates led to better interlocking between layers. Similarly, high w/c ratio made the Interfacial transition zone weaker and the porous. Moreover high coarse aggregate content for low thixotropy resulted as segregation partially. Higher w/c ratio

gave the lowest pull-off strength. It is connected to weaker aggregate paste interface. Moreover since this is a layered specimen, higher w/c ratio at the interlayer zone between layers decreased the bond strength. Tested specimens are given in Appendix D.

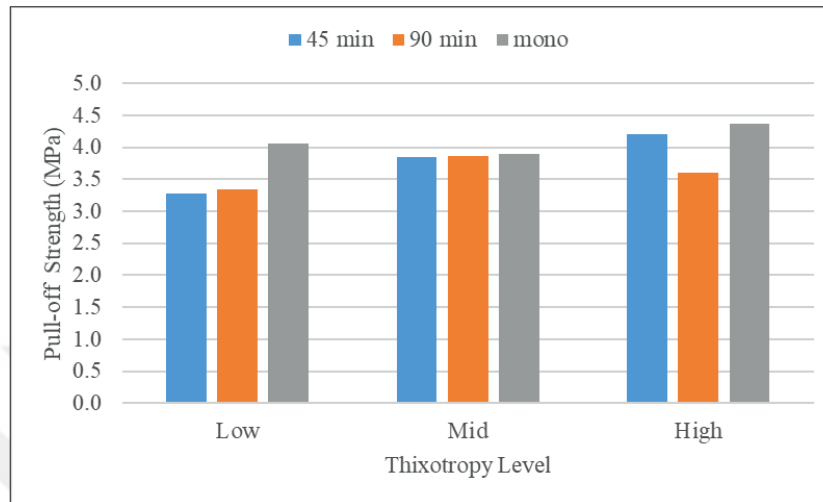


Figure 4.18 Pull-off test results

Table 4.10 Pull-off test results

Delay Between layers	Thixotropy level	Pull-off strength (MPa)	COV
45 min	Low	3.28	0.1160
	Mid	3.85	0.2411
	High	4.2	0.1445
90 min	Low	3.35	0.0789
	Mid	3.86	0.1001
	High	3.61	0.234
mono	Low	4.06	0.1774
	Mid	3.9	0.0617
	High	4.37	0.0989

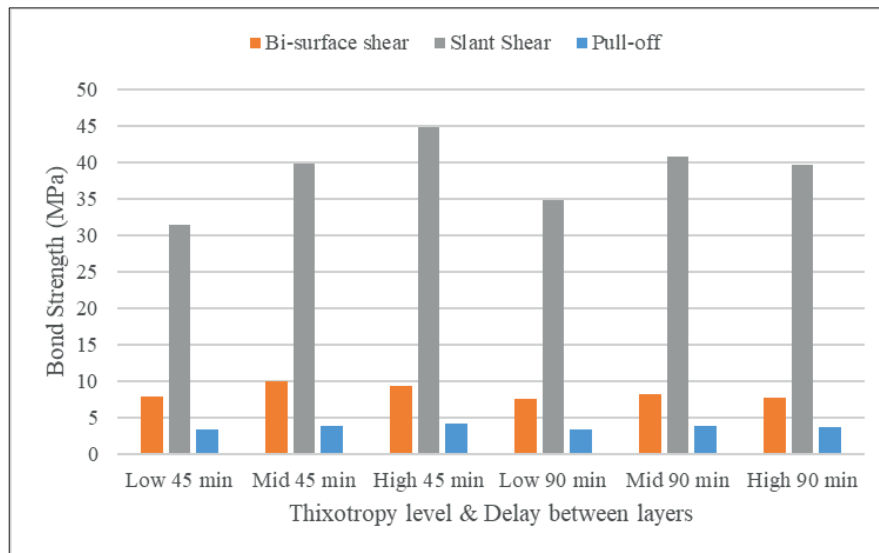


Figure 4.19 Bonding tests comparison

Pull-off test results showed that mixture with high thixotropy showed loss in bond strength drop in pull off strength 13 % from 45 minutes to 90 minutes delay. Similar drop in strength didn't detected for low and mid thixotropy specimens.

Bi-surface shear, slant shear, and pull-off test methods were used to assess bond strength for the specimens. It is beneficial to compare all the results related to bonding properties in the same graph. Figure 4.19 indicates the lowest values were obtained with the pull-off test. Pull-off results and slant shear results showed that the best bonding belongs to the mixture with high thixotropy having 45 min delay between layers. All of the three tests gave similar results for the lowest bonding and it was the mixture with low thixotropy and 45 min delay. This is connected to a higher w/c ratio. Lower water content increased the strength at the aggregate-paste interface. Moreover, for the mixture coded as "mid," optimal mixture proportions and 60 cm slump flow gave the highest bonding strength for 45 minutes. COV values changed between 9-24% for Pull-off, 2-10% for Slant Shear and 2-12% for Bi-surface Shear tests.

One of the reasons for the lowest strength for the pull-off is for slant shear test, combined state of compression and shear; for the bi-surface shear test, there is shear force and bending moment, on the contrary for pull-off test pure tensile stress was applied.

Results were varied for slant shear, bi-surface shear and pull-off test in decreasing order. Similar sorting was also reported in the article by Momayez et al. (Momayez et al. 2005).

Load eccentricity, partial core depth, thickness of substrate layer and loading rate may affect the pull-off results. Heterogeneity of concrete and granular materials in the concrete made the COV values higher for Pull-off test (Bonaldo and Barros, 2004).

4.2.5. UPV results

Table 4.11 shows the UPV results for cubic, cylindrical and beam specimens. Velocity results are shown in km/s to compare with the values as given in ASTM C597 (ASTM C 597-09 2010) (see table Table 3.6). The majority of the UPV results indicate that the concrete quality degree is good and excellent. For cubic and cylinder specimens, average results were taken for three specimens. For beam specimens, one specimen was tested for each mixture and delay.

Ultrasonic pulse velocity test method calculates the duration of the transmitting pulse along the specimen. This test method is an indirect method to gain knowledge about homogeneity of the specimens. According to this homogeneity, assumptions can be made about mechanical properties of the specimen.

Table 4.11 UPV results (km/s)

Thixotropy level		Low		Mid		High	
Duration (min)		45	90	45	90	45	90
Pattern	D1	5.59	5.59	5.63	5.74	5.45	5.60
	D2	5.54	5.47	5.58	5.82	5.54	5.49
	D3	5.47	5.56	5.48	5.73	5.46	5.65
	D4	5.58	5.61	5.59	5.65	5.49	5.69
	D5	5.43	5.53	5.71	5.70	5.39	5.60
Mono (Cubes)		5.52		5.46		5.43	
Slant Shear		4.31	4.23	4.25	4.42	4.40	4.24
Mono (Cylinders)		4.52		4.64		4.41	
Bi-surface Shear		5.87	5.52	5.90	5.63	5.69	5.47
Beam specimens		4.17	4.29	4.35	4.72	4.17	5
Mono (beams)		4.2		4.05		3.66	

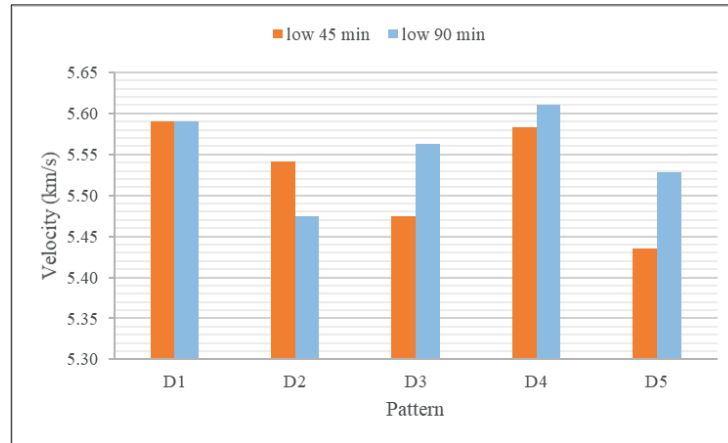


Figure 4.20 UPV results of cubes with patterns for low thixotropy

The change of average UPV results with the pattern type is seen in Figure 4.20, Figure 4.21 and Figure 4.22. 90-min delay between layers gave higher rates of velocity compared to 45 minutes delay for three thixotropy levels. On the contrary, specimens coded with D1LO45, D2LO45 and D5MID45 showed lower rates of velocity for 45 minutes delay. Cubic specimens were prepared with the successive casting of layers. As explained in previous sections, a new batch of concrete was produced for a layer of a specimen. Therefore, to compare two specimens prepared with a delay, four batches of concrete have to be considered. So, a composite concrete specimen was tested with a sonic pulse and velocity of the sonic pulse can give information about concrete. The mechanism of the wave propagation is given in the book of Concrete (p. 404). Ultrasonic Pulse transmits from least porous and most solid as well as the fastest way (Mehta and Monteiro 2006). With another say, UPV results for a layered specimen does not reflect the whole material property but only the more homogeneous and denser layer of the concrete. The same assumption can be made for all horizontally layered specimens tested with UPV.

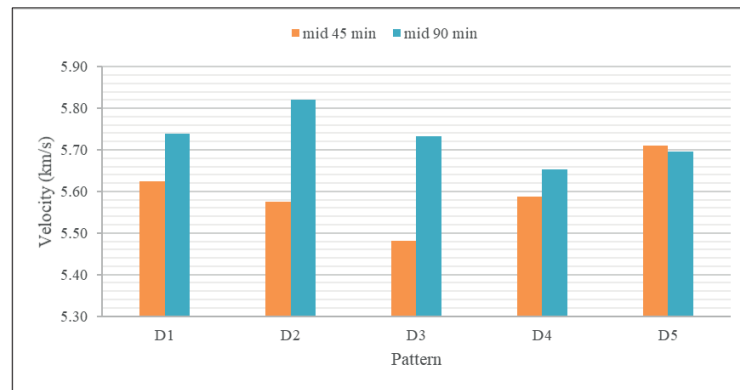


Figure 4.21 UPV results of cubes with patterns for mid thixotropy

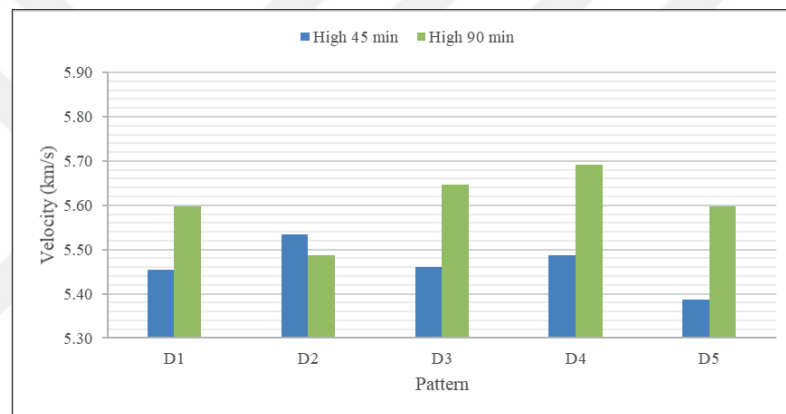


Figure 4.22 UPV results of cubes with patterns for high thixotropy

There are two factors that affect the UPV results for the beams. Length of the specimens (60 cm) increased the change of faults and discontinuity of the homogeneous structure resulted as lower speeds when compared cubic specimens. Moreover, because of the factors listed above, commenting on the different delay times will not be legitimate. For monolithic specimens, high thixotropy gave the lowest velocity. Low thixotropy gave the highest velocity rate. Possible workability drop and partial slump loss for high thixotropy and mid thixotropy may be the reason for the difference.

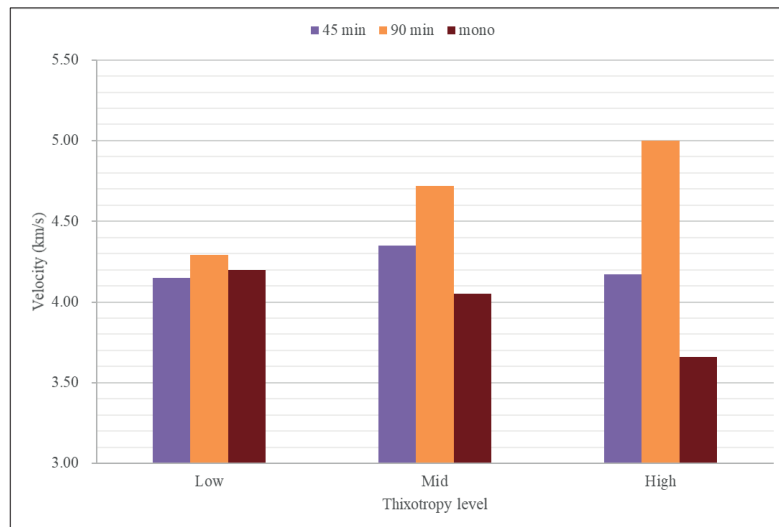


Figure 4.23 UPV results of the beam specimens

Results from UPV testing of the cylinder specimens are given in Figure 4.24. Monolithic specimens gave the highest results for mid and low thixotropy. For high thixotropy 45 minutes delay gave similar result with the monolithic specimen. Ultrasonic pulse velocity results mostly related to w/c ratio. Moreover, interface between layers were perpendicular to the sonic pulse and affected the duration of transmitted sonic pulse. From 45 minutes to 90 minutes of delay time, velocity for low and high thixotropy decreased.

The reason for the strength decrease for the high thixotropy; a highly thixotropic SCC has a short time to build structure, if the time exceed a critical value two layer do not mix and establish a connection (Roussel and Cussigh, 2008). Low thixotropy gave close values for 45 and 90 minutes between layers.

Figure 4.25 shows the UPV results for the Bi-surface Shear specimens. Results mostly correlated with the mechanical test results for the Bi-surface Shear test. Highest pulse rate was obtained for the specimen with the highest Bi-surface Shear strength. Relatively higher yield stress of the high thixotropy concrete made the vertical interlayer zone porous. This situation lowered the rate of pulse velocity. Interlayer zone for 45 minutes and 90 minutes of delay affected the UPV results. Higher strength and higher

velocity rate were obtained for 45 minutes when compared to 90 minutes of delay. The reason for the drop is the structuration of the previously placed concrete.

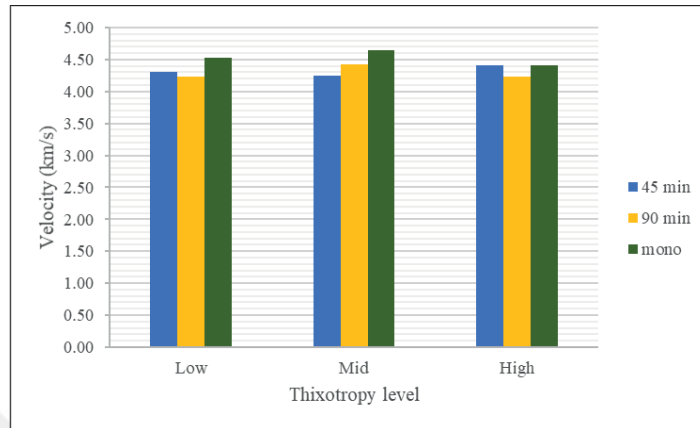


Figure 4.24 UPV for Cylinder specimens

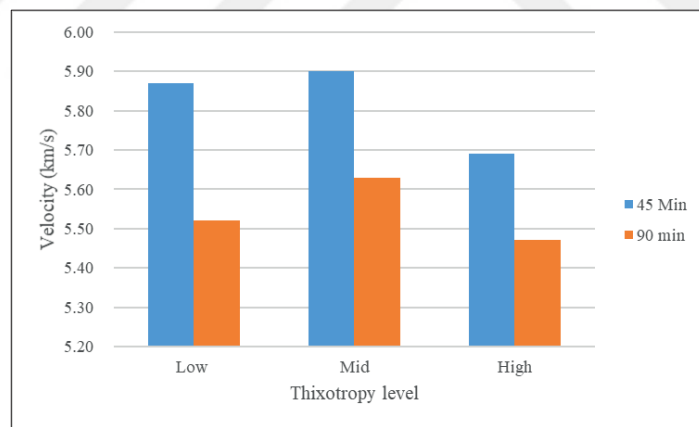


Figure 4.25 UPV for Bi-surface Shear specimens

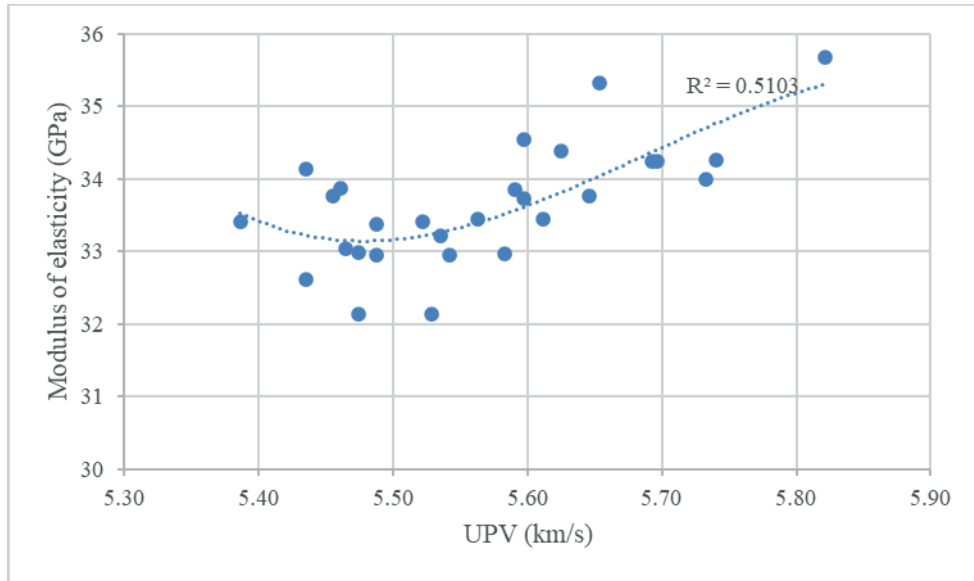


Figure 4.26 Relationship between UPV and E for cubic specimens

As stated by Yildirim and Sengul (Yildirim and Sengul 2011), from the equation in ACI 363 (ACI Committee 363 1997), equation (4.1) was proposed to determine the modulus of elasticity for Self-consolidating concrete, where, E_s is modulus of elasticity in GPa and f_c' in MPa.

From this equation modulus of elasticity was calculated for all cubic specimens (tested for compressive strength). Scatter plot was created from the data of UPV and the module of elasticity. There is a relation between UPV and elasticity with a R^2 value of 0.51. This value was reported as 0.93 by Yildirim & Sengul (Yildirim and Sengul, 2011), 0.80 by Turgut (Turgut, 2004), 0.59 by Nash't et al. (Nash't et al., 2005).

$$E_s = 3320\sqrt{f_c'} + 6900 \quad (4.1)$$

4.3. Surface Properties

As stated in Chapter 3, surface properties were investigated in the terms of average of 10 largest void area in mm², void count and area fraction. Effect of delay between layers, effect of thixotropy, and effect of interlayer pattern (for cubic specimens) were

picked as factors affecting the surface conditions. Beam specimens, Bi surface shear specimens and slant shear specimens were scanned and analyzed, as well.

4.3.1. Cubic Specimens

The effect of interlayer patterns, the effect of delay between layers, and the effect of thixotropy of mixtures on average of the largest voids and total void count of the lateral surfaces have been investigated in this section.

4.3.1.1. Area Fraction and Void Count

Figure 4.27 was generated with the data from the specimens cast with low-level thixotropy. One of the vertical axes on the left shows the void count, and the right axis illustrates the area fraction. For low level thixotropy, main factor was the stability that affect the surfaces. Low yield stress of the mixture made the flow easier for both layers. Whereas for a good stability and to avoid segregation, moderate viscosity is needed for the SCC (K. H. Khayat 1999). No major rise was detected in area fraction with the increase in time. Moreover, for the D3 and D4, 90 minute delay between layers gave the surfaces with less area fraction when compared to 45 minute delay. Geometry and weight of the pattern affected the surface properties.

Geometry of the D1 and D2 patterns, created a predefined roughness, and enhanced the surface between layers. Similar result for 45 and 90 minutes was obtained for each of the D1 and D2 patterns.

Higher area fraction was observed for D3, D4 and D5. Effect of pattern and short delay could not compensate the low uniformity of the concrete with low thixotropy. Possible loss of workability resulted in higher area fraction. Moreover, faults originated from pattern application to the first layer can explain higher area fractions.

Void count numbers ranged between 200 and 300 and specimens prepared with 90 minutes delay gave lower void count. Possibly, longer waiting time resulted as migration of entrapped air. Applied patterns also forced this process.

Several factors affected the surface of hardened specimens. However, sampling and producing steps are crucial for the mixtures with low thixotropy and low uniformity.

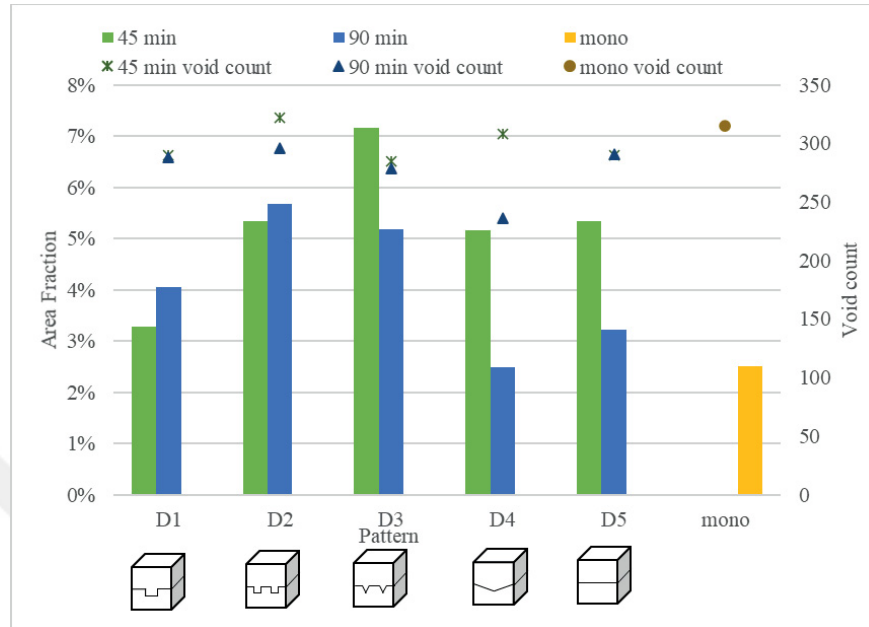


Figure 4.27 Low Level for all patterns

For medium level of thixotropy (Figure 4.28), moderate viscosity and balanced F.A/T.A ratio resulted in similar area fraction values for three pattern (D2, D3 and D4) for 45 minutes delay. This is related to fresh concrete properties since moderate viscosity could carry coarse particles of the mixtures and secures the bonding between layers due to the sufficient roughness. Moderate thixotropy also allowed first layer of concrete to establish a connection with new layer with its relatively low yield stress and moderate viscosity.

For D2, D3 and D4 patterns, area fraction increased with the change in delay. Loss of workability and hydration of cement particles are the reasons for the drop. Gravitational forces affected the coarse particles and triggered segregation. Since first layer of concrete starts to lose its workable plasticity, new layer of concrete increased the area fraction.

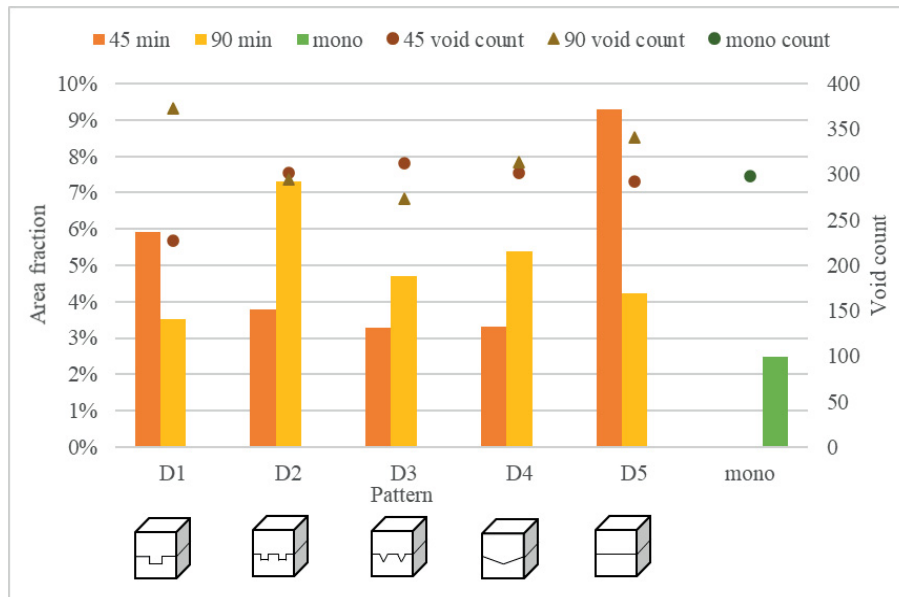


Figure 4.28 Mid level for all patterns

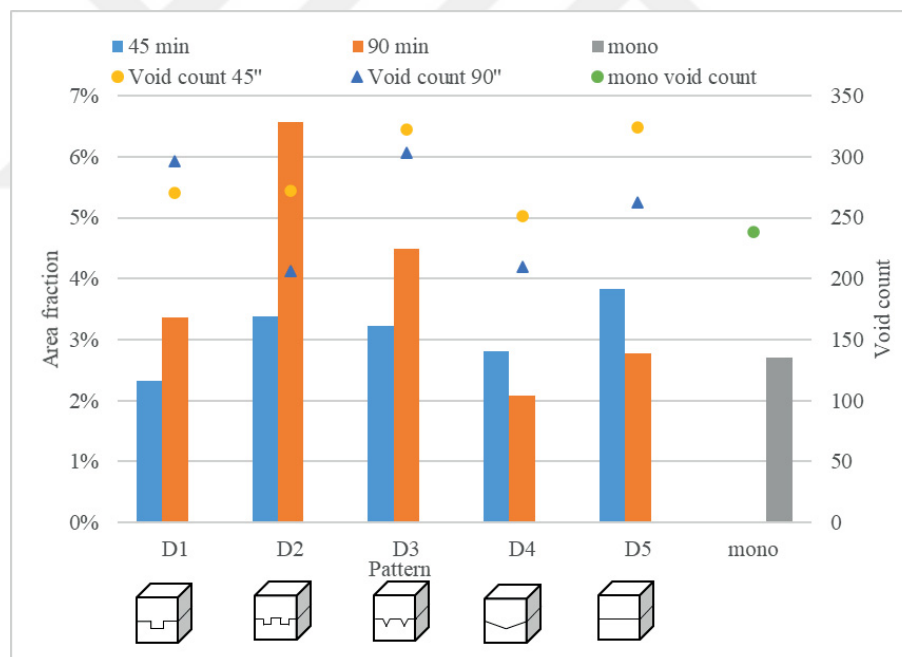


Figure 4.29 High level for all patterns

For high thixotropy (Figure 4.29), same increase in area fraction with mid thixotropy from 45 minutes to 90 minutes was detected for D2 and D3. However, rate of increase is greater for high thixotropy. Geometry of the patterns affected the results due to concrete' flow behaviour, water and coarse aggregate content. This is connected to

high viscosity of the mixtures since low w/c ratio and 70 cm of slump flow ensured enough stability and required filling ability when the surfaces are considered. Accordingly, area fraction changed in a closer range (2.3% to 3.8%) when compared to other thixotropy levels. for 45-minute delay. This value was recorded as 3.3% to 7.2% for low and 3.3% to 9.3% for mid thixotropy.

Monolithic samples were also given on the graphs, and when compared to specimens cast with delay, greatest variations were obtained for mid thixotropy. 2.5% for monolithic sample and 7.2% for D3LO45, 2.5% for MONOMID and 7.3% for D2MID90, 2.7% for MONOHI and 6.6% for D2HI90.

For all levels of thixotropy D2 pattern gave the highest results for 90 minutes. The reason for the rise in the area fraction is the congested design of the pattern.

4.3.1.2. Average area of ten largest points

As a result of the surface scanning process and image analysis, all the void areas were stored in the Excel tables. To see and compare the results of the analysis, all the voids were sorted from large to small by their area. For each concrete surface average of the ten largest points was taken. Conversion from pixel² to mm² was made. Results are given in Table 4.12. Variations were recorded for different patterns. Lowest values were obtained for monolithic specimens. From Figure 4.30 it can be seen that, average void area varies between 10.8 to 52.5 mm². No direct relation was obtained with pattern geometry and the average area of ten largest points. Lowest values were recorded for high thixotropy and 45 minutes of delay. High stability of the mixtures resulted in less void area on the surfaces (11.1 to 17 mm²).

Majority of the specimens (4 of 6 cases, except D5MID45 and D3LO45), largest average void area was obtained for D2 pattern. This result also fits to area fraction results. Congested geometry of D2 pattern increased the void area on the interlayer zone.

For high and low thixotropy, D1 and D4 gave the lowest average void area. Design of D1 and D4 helped for consolidation with predefine roughness and prepare the first layer to second layer in 45 and 90 minutes.

Table 4.12 Results for average of 10 largest void area

Notation	Average of ten largest void mm ²	Notation	Average of ten largest void mm ²
D1LO45	14.9	D1LO90	19.6
D2LO45	26.4	D2LO90	31.3
D3LO45	38.7	D3LO90	27.3
D4LO45	26.9	D4LO90	11.4
D5LO45	29.2	D5LO90	15.1
D1MID45	33.9	D1MID90	16.0
D2MID45	18.1	D2MID90	41.1
D3MID45	15.0	D3MID90	24.9
D4MID45	14.5	D4MID90	27.9
D5MID45	52.5	D5MID90	21.1
D1HI45	11.1	D1HI90	16.6
D2HI45	16.7	D2HI90	38.1
D3HI45	14.6	D3HI90	22.1
D4HI45	13.4	D4HI90	10.8
D5HI45	17.0	D5HI90	13.7

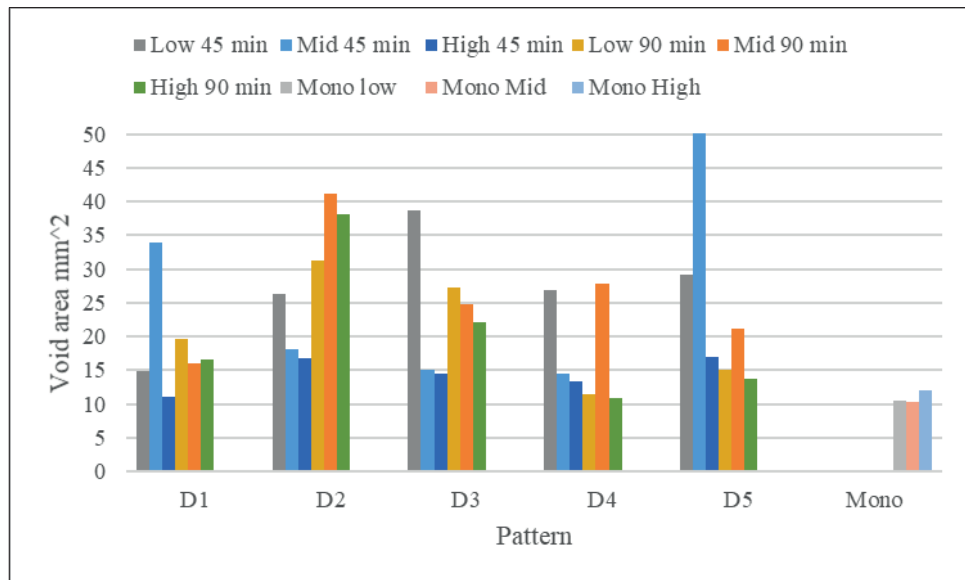


Figure 4.30 Average of 10 largest void area

4.3.2. Cylindrical Specimens

Images were captured to analyze the specimens prepared for slant shear testing. Table 4.13 shows the area fraction void count change. Specimens were prepared with the procedure previously stated, and different delays between layers as 0 min, 45 min, and 90 min were applied. The change in area fraction with delay time and thixotropy level is given in Figure 4.31.

Table 4.13 Cylinder surface analysis

Delay (min)	Thixotropy level	Void count	Average of ten largest void mm ²	Average void size In mm ²	Area fraction
45	low	179	10.53	0.27	0.17
	mid	182	10.80	0.17	0.17
	high	166	12.17	0.21	0.19
90	low	258	7.79	0.16	0.13
	mid	297	9.04	0.17	0.15
	high	248	10.64	0.08	0.17
mono	low	259	9.16	0.14	0.15
	mid	205	14.53	0.13	0.11
	high	257	8.24	0.13	0.13

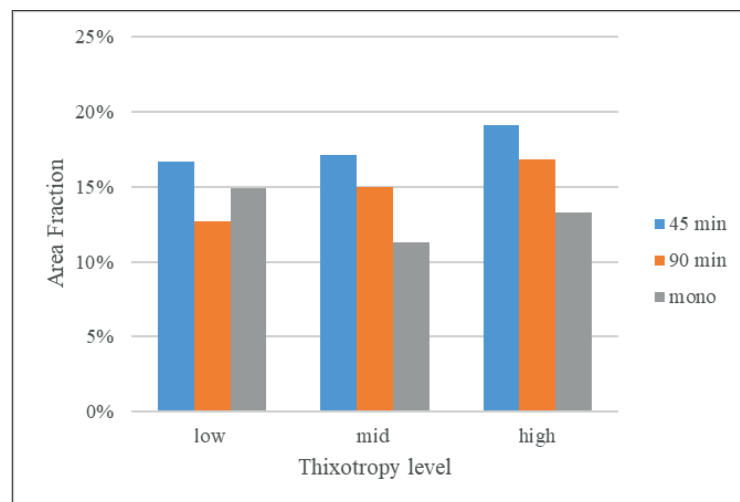


Figure 4.31 Surface analysis results of cylinders

Surface analysis results show that monolithic specimens gave the lowest area fractions parallel to cubic specimens results for mid and high thixotropy. 45 minutes delay between layers resulted in higher area fraction. Moreover, low stability of the mixture in an angled formwork is the reason of the difference for higher area fraction for low thixotropy.

Circular form surface and low surface quality originated from steel formwork may be the reason for the difference between 45 minutes and 90 minutes since those factors are more dominant than setting process of concrete. Moreover, scanning of the circular surfaces with 2D image processing may not be convenient since the whole process of measuring particles has to be very precise.

4.3.3. Beam Specimens and Bi-Surface Shear Specimens

The surfaces of Bi-surface shear specimens and beam specimens were investigated. 15*60 cm specimens void area and count increased with the delay between layers and the thixotropy. No cover or pattern was used for those specimens.

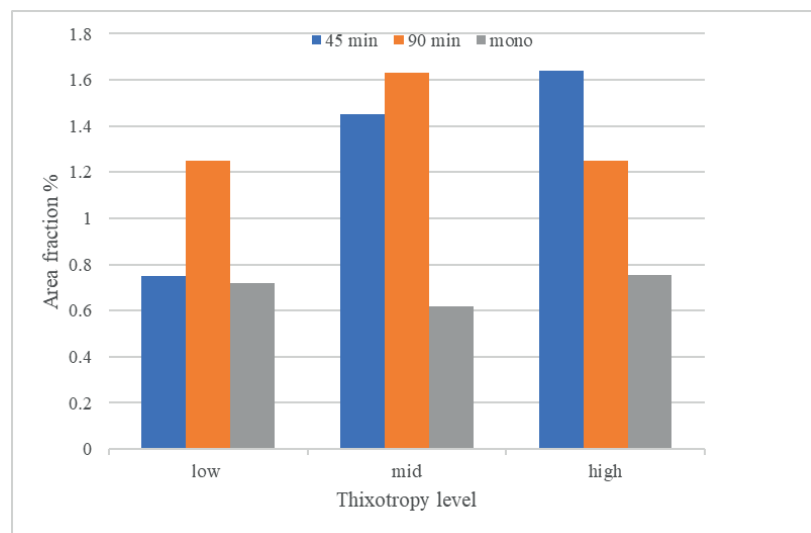


Figure 4.32 Results for the beam specimens

Left-as-cast specimens showed that when the beam surfaces were compared to cubic specimens, there was a positive impact of surface treatment on lateral surfaces of the cubic specimens since the area fraction decreased with time.

Surface analysis results show that low thixotropy gave the lowest area fraction for 45 minutes and 90 minutes delay. For the mid and high thixotropy, 45 minutes delay gave slightly higher area fraction when compared to 90 minutes. Difference is larger for the low thixotropy. Even though a sharp rise is shown, when compared to other surfaces area fraction, very low values were obtained for the beam specimens.

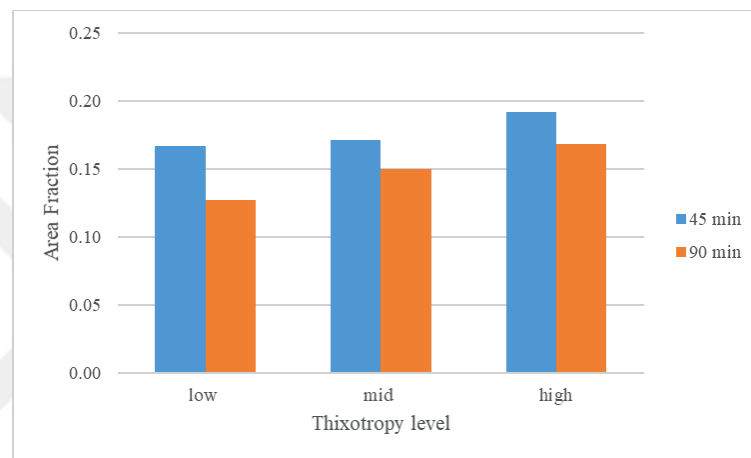


Figure 4.33 Bi surface shear specimens surface results

Unlike other tests, for the bi-surface shear test, vertical joint was created between first and second layer. Interlayer zone between the first and second layer is affected by different factors for this test. Especially removal of the foam that blocks the 1/3 of the mold usually agitates the remaining 2/3 of the concrete. This effect is more significant for the low thixotropy concrete with low structural build-up. This agitation of 2/3 is less visible for 90 minutes since concrete has more time to rest and build a gel structure and inter-particle links.

4.3.4. Extracting volumetric information

Since the 2D void information is used by this method, comparisons can be made with only largest voids from 2D image analysis data. SSIM method is a relatively new method and minor changes in the illumination, results in major differences. Moreover, color variations on the concrete surface can be detected as depth changes and this can alter the volumetric data.

Similar to the data obtained from the previous analysis, data were extracted from the stereo images (in the second part of the surface scanning procedure). This process is explained in section 3.3.8. Briefly, depth information is combined with the 2D information of detected cavities. Table 4.14 shows the average results obtained from three specimens.

Table 4.14 Volumetric info of the specimens

Notation	Volumetric info mm ³	Notation	Volumetric info mm ³	Notation	Volumetric info mm ³
D1LO45	139	D3HI45	148	D5MID90	188
D2LO45	292	D4HI45	131	D1HI90	175
D3LO45	247	D5HI45	185	D2HI90	339
D4LO45	91	D1LO90	149	D3HI90	136
D5LO45	100	D2LO90	323	D4HI90	125
D1MID45	273	D3LO90	357	D5HI90	177
D2MID45	176	D4LO90	246	MONOLO	180
D3MID45	104	D5LO90	303	MONOMID	67
D4MID45	169	D1MID90	128	MONOHI	88
D5MID45	357	D2MID90	278		
D1HI45	110	D3MID90	190		
D2HI45	148	D4MID90	161		

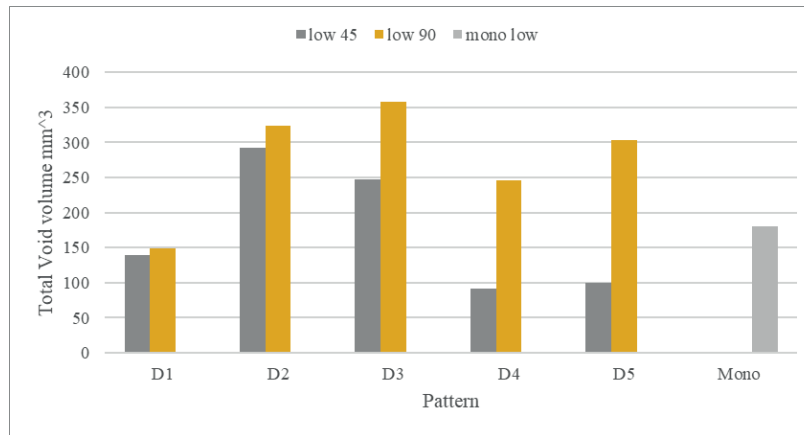


Figure 4.34 Void volume change with the Low thixotropy

Volumetric change with the delay for the level of thixotropy and the pattern number is shown in Figure 4.34. At the first stage, if the pattern effect is investigated, D2 and D3 gave the highest void volume for 45 and 90 minutes.

If the concrete has more time to build internal structure, establishing a connection between layers become difficult. This is the explanation for the rise for D3 D4 and D5 from 45 minutes delay to 90 minutes delay.

Monolithic specimen gave considerably high volume of voids on the surfaces when compared to other monolithic specimens for low thixotropy. Low thixotropy accordingly, low viscosity and yield stress resulted as more voids on the surface. Entrapped air voids followed a shorter distance to the upper surface for the layered specimens when compared to monolithic specimens. This may be a possible explanation for lower void volume for monolithic specimen with low thixotropy. Pattern application lowered total volume of voids for D1LO45, D1LO90, D4LO45 and D5LO45. Low thixotropy concrete may be affected from the applied pressure during application of the patterns. Pressure generated from the application altered the results for 45 minutes. Entrapped air voids followed a shorter distance to the upper surface for the layered specimens when compared to monolithic specimens.

Figure 4.35 shows the void volume change with different patterns. If the concrete has more time to build internal structure and if the yield stress of the first layer increases, establishing a connection between layers becomes difficult. This is the explanation for the rise for area fraction of the specimens with D2 and D3 patterns, from 45 minutes delay to 90 minutes delay.

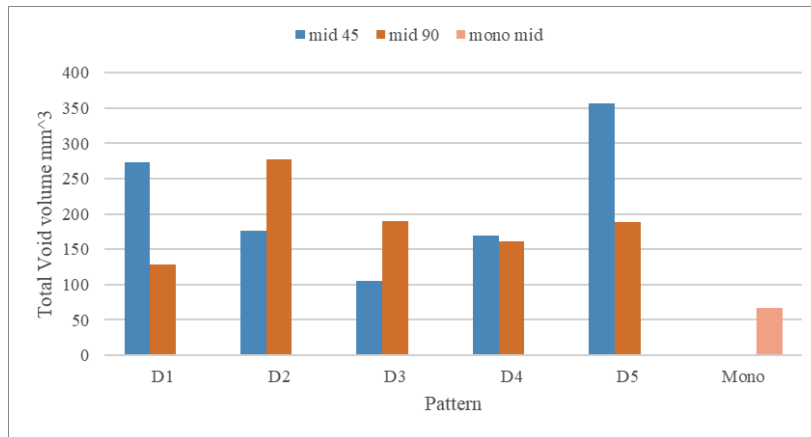


Figure 4.35 Void volume change with the mid thixotropy

For D1 pattern unexpected rise for 45 min delay can be seen from Figure 4.35. Possible change in workability, partial slump loss of the concrete in the mold can be reason for relatively high volumes for a shorter delay. Angular structure of D1 pattern also affected the aggregate particles therefore variations occurred on the surface condition.

Figure 4.36 shows the void volume change with different patterns. Similar to 2D surface area results, high thixotropy gave consistent performance since minor differences were seen from 45 minutes to 90 minutes delay. However, for 90 minutes delay, D2 pattern applied specimen showed excessive rise for volume. Congested structure of D2, high thixotropy of the mixture related to high coarse particle content and low w/c ratio were the reason for that rise.

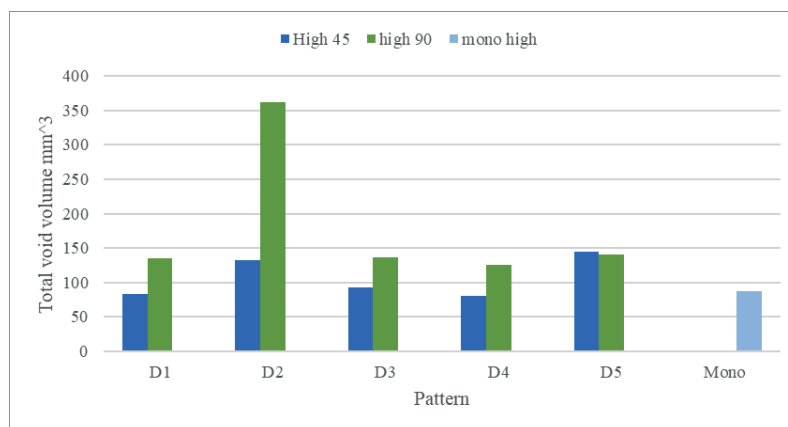


Figure 4.36 Void volume change with high thixotropy

CONCLUSION

5.1. Summary

Mixtures with higher coarse aggregate content (larger skeleton) gave longer durations of V-funnel time with higher thixotropy values.

Lower w/c ratio resulted as higher torque plastic viscosity values even with the lower coarse aggregate content.

Apparent yield stress is increased with time from 0 to 90 minutes for the mixtures for three w/c ratio (0.36 0.41 and 0.46)

The segregation index was increased with the slump flow accordingly.

For all levels of thixotropy, D2 pattern gave the highest results for 90 minutes. The reason for the rise in the area fraction is the congested design of the pattern. For 45 minutes delay no significant pattern effect was seen.

15*60 cm specimen's void area and count increased with time and thixotropy.

No relation was obtained between mechanical strength and the pattern geometry for cubic specimens. Whereas, there is an inverse relation between lateral surface properties and mechanical strength. Mixture proportions both affected the surface properties and thixotropy. Highest strength for the cubic specimens was recorded for mid thixotropy, however high thixotropy gave slightly lower area fraction when compared to mid thixotropy level. Low thixotropy gave the lowest strength and highest area fraction for the cubic specimens.

With an increase in the number of analyzed surfaces, correlating pattern geometry with surface properties and with mechanical properties may be possible.

Bond strength was determined with three different methods. The highest values were obtained with the slant shear test method. Monolithic samples gave the highest strength values for the pull-off test method and slant shear test method.

4% drop occurred for the specimens prepared with the mixtures with high thixotropy with the increase in delay from 45 minutes to 90 minutes between layers. Likewise, 18% and 20% strength loss occurred for the specimens prepared with low thixotropy with 45 and 90minutes delay time respectively when compared to monolithically cast specimens for the Pull-off test.

Bi-surface shear test results showed that, 5% 20% 21% strength loss recorded for low, mid and high thixotropy respectively, from 45 to 90-minute delay between layers

Cylinder specimen's analysis results showed that for low thixotropy, higher area fraction and lower bond strength was obtained. Invariably, higher bond strength values were found with lower area fractions.

Volumetric analysis of the samples showed that high thixotropy gave the lowest void volume in average.

For the majority of the volumetric analysis results, total void volume increased with the delay between layers.

For the specimens prepared with application of patterns with changing thixotropy levels (13 of 15) area fraction values correlated with calculated volume with structural similarity index method. A decrease in area fraction resulted in a decrease in total volume of voids and vice versa.

The 3D surface analysis needed much more computing power and less efficient when compared to 2D. However, the results were compatible with the 2D results. A similar range was obtained at calculating the volume of the voids. Moreover, mixtures with low thixotropy gave the higher area fraction as well as the highest total void volume when compared to other mixtures.

5.2. Recommendations

Concrete to concrete bond strength with relatively shorter delays has to be investigated exhaustively.

For the future studies, examining surfaces for successive casting can be studied on thinner and larger structural panels.

An increase for the number of scanned surfaces, less factors for the design of the mixtures and test setup will be beneficial for interpreting the results.

Layered specimens can be tested in perpendicular direction to the layers with UPV in order to assess information about interlayer zone.

To access the volumetric data of the surface, stereovision and 3-D scene construction with a specially designed illumination from multiple high-definition cameras may be a research area. Moreover, flow properties of Self consolidating concrete can be modelled in 3D detail with the help of stereovision. Same procedure can be used for crack patterns and fracture planes of the tested specimens.

REFERENCES

- ACI Committee 238. 2008. *Report on Measurements of Workability and Rheology of Fresh Concrete*.
- ACI Committee 363. 1997. "State-of-the-Art Report on High-Strength Concrete." *American Concrete Institute*.
- Aicha, Mouhcine Ben. 2020. *The Superplasticizer Effect on the Rheological and Mechanical Properties of Self-Compacting Concrete*. *New Materials in Civil Engineering*. INC. <https://doi.org/10.1016/b978-0-12-818961-0.00008-9>.
- Akbar Ali, Shirzadi Javid, Parviz Ghoddousi, Gholamreza Ghodrati Amiri, and Khalil Donyadideh. 2019. "A New Photogrammetry Method to Study the Relationship between Thixotropy and Bond Strength of Multi-Layers Casting of Self-Consolidating Concrete." *Construction and Building Materials* 204: 530–40. <https://doi.org/10.1016/j.conbuildmat.2019.01.204>.
- ASTM C882/C882M-13a, Standard Test Method for Bond Strength of Epoxy-Resin Systems Used With Concrete By Slant Shear. ASTM International 2013.
- ASTM C188- Standard Test Method for Density of Hydraulic Cement." American Society for Testing and Materials International *Annual Book of ASTM Standards*. <https://doi.org/10.1053/jhsu.2001.20160> 2017.
- Assaad, Joseph, Kamal H. Khayat, and Habib Mesbah. 2003. "Assessment of Thixotropy of Flowable and Self-Consolidating Concrete." *ACI Materials Journal*. <https://doi.org/10.14359/12548>.
- ASTM C29/C29M-09. 2009. "Standard Test Method for Bulk Density (‘ Unit Weight ’) and Voids in Aggregate." *ASTM International* i (c): 1–5. <https://doi.org/10.1520/C0029>.
- ASTM C191-08 "Standard Test Methods for Time of Setting of Hydraulic Cement by Vicat Needle" *Annual Book of ASTM Standards 191-08* i (C): 1–10. <https://doi.org/10.1520/C0191-08.2>.
- ASTM C403-08. 2008. "Standard Test Method for Time of Setting of Concrete Mixtures by Penetration Resistance" 04: 1–6.
- ASTM C457. 2013. "Standard Test Method for Microscopical Determination of Parameters of the Air-Void System in Hardened Concrete." *ASTM International*. <https://doi.org/10.1520/C0457>.
- ASTM C597-09. 2010. "Standard Test Method for Pulse Velocity Through Concrete¹." *United States: American Society for Testing and Material*. 04 (02): 3–6. <https://doi.org/10.1520/C0597-09>.

- ASTM C128-15.. “Standard Test Method for Relative Density (Specific Gravity) and Absorption of Fine Aggregate.” *American Society for Testing and Materials*. <https://doi.org/10.1520/C0128-15>. (2015)
- ASTM C1583. “Standard Test Method for Tensile Strength of Concrete Surfaces and the Bond Strength or Tensile Strength of Concrete Repair and Overlay Materials by Direct Tension (Pull-off Method).” *ASTM International*. (2013)
- ASTM C 136 Standard Test Method for Sieve Analysis of Fine and Coarse Aggregates.” *Annual Book of ASTM Standards* 04 (C): (2013) 1–5. <https://doi.org/10.1520/C0136-06.2>.
- ASTM C494/C494M-04: Standard Specification for Chemical Admixtures for Concrete. American Society for Testing and Materials. <https://doi.org/10.1520/C0260>. (2015)
- ASTM C127-15, Standard Test Method for Relative Density (Specific Gravity) and Absorption of Coarse Aggregate, ASTM International, (2015) DOI: 10.1520/C0127-15,
- Aysha, H, K R Ramsundar, M Arun, and G Velraj Kumar. “An Overview of Interface Behaviour between Concrete to Concrete” *International Journal of Advanced Structures and Geotechnical Engineering* 03 (02): (2014) 1–5. ISSN 2319-5347, Vol. 03, No. 02
- Banfill, Phillip. 1991. “Rheology of Fresh Cement and Concrete.” *Rheol Rev*. <https://doi.org/10.4324/9780203473290>.
- Barnes, Howard A.. “Thixotropy—a Review.” *Journal of Non-Newtonian Fluid Mechanics* 70 (1–2): (1997) 1–33. [https://doi.org/10.1016/S0377-0257\(97\)00004-9](https://doi.org/10.1016/S0377-0257(97)00004-9).
- Beushausen, H., and M. G. Alexander. 2008. “Bond Strength Development between Concretes of Different Ages.” *Magazine of Concrete Research* , (2008): 60 (1): 65–74. <https://doi.org/10.1680/macrc.2007.00108>.
- Billberg, P H.. “The Structural Behaviour of SCC at Rest.” *36th Conference on Our World in Concrete & Structures*, no. (2011) August: 1–9. <http://cipremier.com/100036004>.
- Bonaldo, Everaldo, Joaquim A O Barros, and Paulo B. Lourenço.. “Bond Characterization between Concrete Substrate and Repairing SFRC Using Pull-off Testing.” *International Journal of Adhesion and Adhesives* 25, (6) (2005): 463–74. <https://doi.org/10.1016/j.ijadhadh.2005.01.002>.

- British Standards Institution. “BS 8500-1:2006 Concrete — Complementary British Standard to BS EN 206-1 Part 1: Method of Specifying and Guidance for the Specifier.” *British Standards*. (2006)
- Bungey, John H., and Michael G. Grantham. *Testing of Concrete in Structures. Testing of Concrete in Structures*. (2006) <https://doi.org/10.1201/9781482264685>.
- Chatterji, S., and H. Gudmundsson. “Characterization of Entrained Air Bubble Systems in Concretes by Means of an Image Analysing Microscope.” *Cement and Concrete Research* 7 (1977) (4): 423–28. [https://doi.org/10.1016/0008-8846\(77\)90070-9](https://doi.org/10.1016/0008-8846(77)90070-9).
- CNS Farnell. n.d. “Pundit 6 Manual.” *Proceq*, 105–8.
- Cold Joints.” n.d. Concrete Society. Accessed October 11, (2020). <http://www.concrete.org.uk/>.
- Courard, Luc, Tomasz Piotrowski, and Andrzej Garbacz. “Near-to-Surface Properties Affecting Bond Strength in Concrete Repair.” *Cement and Concrete Composites* (2014) 46: 73–80. <https://doi.org/10.1016/j.cemconcomp.2013.11.005>.
- Çalı, Mehmet. “Depth Estimation Report.” [Unpublished manuscript], Department Of Electrical And Electronics Engineering, (2019) 15-30 İzmir Institute of Technology, İzmir.
- Delatte, Norbert, M Williamson, and David Fowler.. “Bond Strength Development with Maturity of High-Earlystrength Bonded Concrete Overlays.” *ACI Structural Journal* 97 (2000) (March): 201–7.
- Diab, Ahmed M., Abd Elmoaty M. Abd Elmoaty, and Mohamed R. Tag Eldin.. “Slant Shear Bond Strength between Self Compacting Concrete and Old Concrete.” *Construction and Building Materials* (2017) 130: 73–82. <https://doi.org/10.1016/j.conbuildmat.2016.11.023>.
- Domone, P. “The Slump Flow Test for High-Workability Concrete.” *Cement and Concrete Research*. (1998) 177-182, [https://doi.org/10.1016/S0008-8846\(97\)00224-X](https://doi.org/10.1016/S0008-8846(97)00224-X).
- Dzuy, Nguyen Q., and D. V. Boger. “Direct Yield Stress Measurement with the Vane Method.” *Journal of Rheology* 29, (1985): 335. <https://doi.org/10.1122/1.549794>.
- EFNARC. “The European Guidelines for Self-Compacting Concrete.” *The European Guidelines for Self Compacting Concrete*, no. May (2005).
- Erdem, Tahir Kemal; Kamal H. Khayat and Ammar Yahia. “Correlating Rheology of Self-Consolidating Concrete to Corresponding Concrete-Equivalent Mortar.” *ACI Materials Journal* 106 (2) (2009): 154–60. <https://doi.org/10.14359/56462>.

- Erdem, Tahir Kemal ; Özge Andiç-Çakır; Ali Topal; Mustafa Şahmaran; Kambiz Ramyar; Hasan Yavuz Ersöz; Murat Tuyan; Reza Saleh Ahari.. “Kendiliğinden Yerleşen Betonlarda Tiksotropinin Kalıp Basıncı , Yüzey ve Dürabilite Özelliklerine Etkileri Proje No : 109M615.” (2012), 94.
- Ersöz, Hasan Yavuz.. “Effects of Thixotropy on Self Consolidating Concrete Surface Properties.”, [Master’s thesis], (2012), 101. Izmir Institute of Technology.
- Fang, Chuanxin, and Samuel Labi. 2007. “Image-Processing Technology to Evaluate Static Segregation Resistance of Hardened Self-Consolidating Concrete.” *Transportation Research Record: Journal of the Transportation Research Board*, no. 2020: pp 1-9. <https://doi.org/10.3141/2020-01>.
- Fei, Liang, Li Yan, Changhai Chen, Zhiyun Ye, and Jiantong Zhou.. “OSSIM: An Object-Based Multiview Stereo Algorithm Using SSIM Index Matching Cost.” *IEEE Transactions on Geoscience and Remote Sensing* (2017) 55 (12): 6937–49. <https://doi.org/10.1109/TGRS.2017.2737033>.
- Ferraris, Chiara F.. “Measurement of the Rheological Properties of High Performance Concrete: State of the Art Report.” *Journal of Research of the National Institute of Standards and Technology*., (1999) 461–478 <https://doi.org/10.6028/jres.104.028>.
- Fonseca, P. C., and G. W. Scherer. “An Image Analysis Procedure to Quantify the Air Void System of Mortar and Concrete.” *Materials and Structures* 48 (10) (2015): 3087–98. <https://doi.org/10.1617/s11527-014-0381-9>.
- Gaimster, Rob, and Noel Dixon.. “Self-Compacting Concrete.” In *Advanced Concrete Technology*., Butterworth-Heinemann books, (2003): Pages 1-22, <https://doi.org/10.1016/B978-075065686-3/50295-0>.
- Gonzalez, Rafael C, and Richard E Woods. *Digital Image Processing (3rd Edition)*. Prentice-Hall, Inc. Upper Saddle River, NJ, USA (2006). [https://doi.org/10.1016/0734-189X\(90\)90171-Q](https://doi.org/10.1016/0734-189X(90)90171-Q).
- Jähne, Bernd.. *Digital Image Processing: 6th Revised and Extended Edition*. *Digital Image Processing: 6th Revised and Extended Edition*. (2005) <https://doi.org/10.1007/3-540-27563-0>.
- Jakobsen, U. H., C. Pade, N. Thaulow, D. Brown, S. Sahu, O. Magnusson, S. De Buck, and G. De Schutter. “Automated Air Void Analysis of Hardened Concrete - a Round Robin Study.” *Cement and Concrete Research*. (2006) <https://doi.org/10.1016/j.cemconres.2006.03.005>.
- Jeffery S. Volz, Carlton A. Olson, Ralph G. Oesterle, And Steven H. Gebler. (1997). “Are They Pour Lines.” p. 8-15
- Joseph J. Assaad.. “Formwork Pressure of Self-Consolidating Concrete-Influence of Thixotropy.”, Sherbrooke University. (PhD thesis) (2004) p.494

- Kevern, John T., Kejin Wang, and Vernon R. Schaefer.. “Test Methods for Characterizing Air Void Systems in Portland Cement Pervious Concrete.” *Journal of ASTM International*. (2009) <https://doi.org/10.1520/JAI102451>.
- Khayat, Kamal. H.. “Workability, Testing, and Performance of Self-Consolidating Concrete.” *ACI Materials Journal*. (1999) <https://doi.org/10.14359/632>.
- Khayat, Kamal H., Mladenka Saric-Coric, and Frank Liotta.. “Influence of Thixotropy on Stability Characteristics of Cement Grout and Concrete.” *ACI Materials Journal* (2002) 99 (3): 234–41. <https://doi.org/10.14359/11968>.
- Khayat Kamal H, Megid Wael A Megid. “Bond Strength in Multilayer Casting of Self-Consolidating Concrete.” *ACI Structural Journal* 114 (2017) (3): 467–76. <https://doi.org/10.14359/51689597>.
- Lapasin, R., A. Papo, and S. Rajgelj.. “Flow Behavior of Fresh Cement Pastes. A Comparison of Different Rheological Instruments and Techniques.” *Cement and Concrete Research*. (1983) Volume 13, Issue 3, Pages 349-356, [https://doi.org/10.1016/0008-8846\(83\)90034-0](https://doi.org/10.1016/0008-8846(83)90034-0).
- Lee, Han-Seung, Hyun-O Jang, and Keun-Hee Cho. “Evaluation of Bonding Shear Performance of Ultra-High-Performance Concrete with Increase in Delay in Formation of Cold Joints.” *Materials* (2016). 9 (5): 362. <https://doi.org/10.3390/ma9050362>.
- Mayercsik, Nathan P., Robert Felice, M. Tyler Ley, and Kimberly E. Kurtis.. “A Probabilistic Technique for Entrained Air Void Analysis in Hardened Concrete.” *Cement and Concrete Research* (2014) 59: 16–23. <https://doi.org/10.1016/j.cemconres.2014.01.023>.
- McNaught, A. D., and A. Wilkinson. *IUPAC Compendium of Chemical Terminology: Gold Book*. Blackwell Scientific Publications. (2014) <https://doi.org/http://dx.doi.org/10.1351/goldbook.I03352>.
- Mehta, P. Kumar, and Paulo J M Monteiro.. *Concrete: Microstructure, Properties, and Materials*. Concrete. (2006) <https://doi.org/10.1036/0071462899>.
- Mohamadien, H A, Nevi Alle, and Sri Ravindrarajah.. “The Impact of the Time When Casting the Second Layer of Concrete on Its Mechanical Properties” (2013) 41 (3): 919–29.
- Momayez, A., M. R. Ehsani, A. A. Ramezani pour, and H. Rajaie.. “Comparison of Methods for Evaluating Bond Strength between Concrete Substrate and Repair Materials.” *Cement and Concrete Research* (2005) 35 (4): 748–57. <https://doi.org/10.1016/j.cemconres.2004.05.027>.

- Momayez, A., A. A. Ramezani-pour, H. Rajaie, and M. R. Ehsani.. “Bi-Surface Shear Test for Evaluating Bond between Existing and New Concrete.” *ACI Materials Journal*. (2004) <https://doi.org/10.14359/13045>.
- Nagaonkar, Dipali S, and Jyoti P Bhusari.. “Characterization of Reactive Powder Concrete with Respect to Its Bond Strength” (2014) 5 (5): 279–282.
- Nash’t Isam H., A’bour Saeed Hameed, Sadoon Anwar Abdallah, Finding an unified relationship between crushing strength of concrete and non-destructive tests, 3rd MENDT, Middle East NDT Conf & Exhibition, 27–30 Nov. (2005), Bahrain, Manama.
- Neville, A. M.. “Ultrasonic Pulse Velocity Test.” *Properties of Concrete*, Pearson, (1995), 864 pp
- Ouchi, Masahiro, Sada-aki Nakamura, Thomas Osterberg, and Sven-Erik Hallberg. “Applications of Self-Compacting Concrete in Japan, Europe and the United States.” (2003). ISHPC 2003: Tokyo-Odaiba, Japan
- Peterson, Karl, Jeremy Carlson, Lawrence Sutter, and Thomas Van Dam. “Methods for Threshold Optimization for Images Collected from Contrast Enhanced Concrete Surfaces for Air-Void System Characterization.” *Materials Characterization*. (2009) <https://doi.org/10.1016/j.matchar.2008.10.005>.
- Peterson, KW, RA Swartz. 2001. “Air Void Analysis of Hardened Concrete with a Flatbed Scanner.” *Journal of the no.* May: 1–28
- Pigeon M, Saucier F. 1992. “F. Durability of Repaired Concrete Structures.” *Proceedings of an International Symposium on Advances in Concrete Technology*, 741–773.
- Rathi, V R, and P K Kolase. 2013. “Rathi, V. R., & Kolase, P. K. (2013). Effect of Cold Joint on Strength Of Concrete. *International Journal of Innovative Research in Science, Engineering and Technology*, 2(9), 4671–4679.” *International Journal of Innovative Research in Science, Engineering and Technology* 2 (9): 4671–79.
- Roussel, N.. “A Theoretical Frame to Study Stability of Fresh Concrete.” *Materials and Structures* (2006) 39: 81-91. <https://doi.org/10.1617/s11527-005-9036-1>.
- Roussel, N., and F. Cussigh. “Distinct-Layer Casting of SCC: The Mechanical Consequences of Thixotropy.” *Cement and Concrete Research* (2008). 38 (5): 624–32. <https://doi.org/10.1016/j.cemconres.2007.09.023>.
- Roussel, N., R. Le Roy, and P. Coussot.. “Thixotropy Modelling at Local and Macroscopic Scales.” *Journal of Non-Newtonian Fluid Mechanics* (2004) 117 (2–3): 85–95. <https://doi.org/10.1016/j.jnnfm.2004.01.001>.
- Roussel, Nicolas.. “A Thixotropy Model for Fresh Fluid Concretes: Theory, Validation and Applications.” *Cement and Concrete Research* (2006) 36 (10): 1797–1806. <https://doi.org/10.1016/j.cemconres.2006.05.025>.

- Roussel, Nicolas. "Rheology of Fresh Concrete: From Measurements to Predictions of Casting Processes." *Materials and Structures/Materiaux et Constructions* (2007). 40 (10): 1001–12. <https://doi.org/10.1617/s11527-007-9313-2>.
- Santos, Pedro M.D., Eduardo N.B.S. Júlio, and Vítor D. Silva.. "Correlation between Concrete-to-Concrete Bond Strength and the Roughness of the Substrate Surface." *Construction and Building Materials* (2007) 21 (8): 1688–95. <https://doi.org/10.1016/j.conbuildmat.2006.05.044>.
- Tattersall, G. H., and P. F.G. Banfill. "Relationships between the British Standard Tests for Workability and the Two-Point Test." *Magazine of Concrete Research* (1977). 29 (100): 156–58. <https://doi.org/10.1680/mac.1977.29.100.156>.
- Turgut P Evaluation of the ultrasonic pulse velocity data coming on the field. In: Fourth international conference on NDE in relation to structural integrity for nuclear and pressurised components, London, (2004), pp 573–578
- W.B. and Thompson, S.E.. "The Laws of Proportioning Concrete,." *Transactions of the ASCE* 159 (1907).
- Wan, Zhifu. 2011. "Interfacial Shear Bond Strength Between Old and New Concrete," no. May.
- Yahia, A., S. Mantellato, and Robert J. Flatt.. *Concrete Rheology: A Basis for Understanding Chemical Admixtures. Science and Technology of Concrete Admixtures.*, (2016) Woodhead Publishing, Pages 97-127, <https://doi.org/10.1016/B978-0-08-100693-1.00007-2>.
- Yen, Jui Cheng, Fu Juay Chang, and Shyang Chang. "A New Criterion for Automatic Multilevel Thresholding." *IEEE Transactions on Image Processing* (1995) 4 (3): 370–78. <https://doi.org/10.1109/83.366472>.
- Yildirim, Hasan, and Ozkan Sengul. "Modulus of Elasticity of Substandard and Normal Concretes." *Construction and Building Materials* (2011) 25 (4): 1645–52. <https://doi.org/10.1016/j.conbuildmat.2010.10.009>.
- Young, Ian, Jan Gerbrands, and Lucas van Vliet.. "Fundamentals of Image Processing," 1–85. (2009) <https://doi.org/10.1201/9781420046090-c13>. 2009b.
- Zalocha, D., and J. Kasperkiewicz.. "Estimation of the Structure of Air Entrained Concrete Using a Flatbed Scanner." *Cement and Concrete Research* (2005) 35 (10): 2041–46. <https://doi.org/10.1016/j.cemconres.2005.05.004>.

APPENDIX A

2D surface analysis examples were given in this section. Total area is in pixel² and average sizes are given as number of pixels.

Table A.1. Results of D1LO45

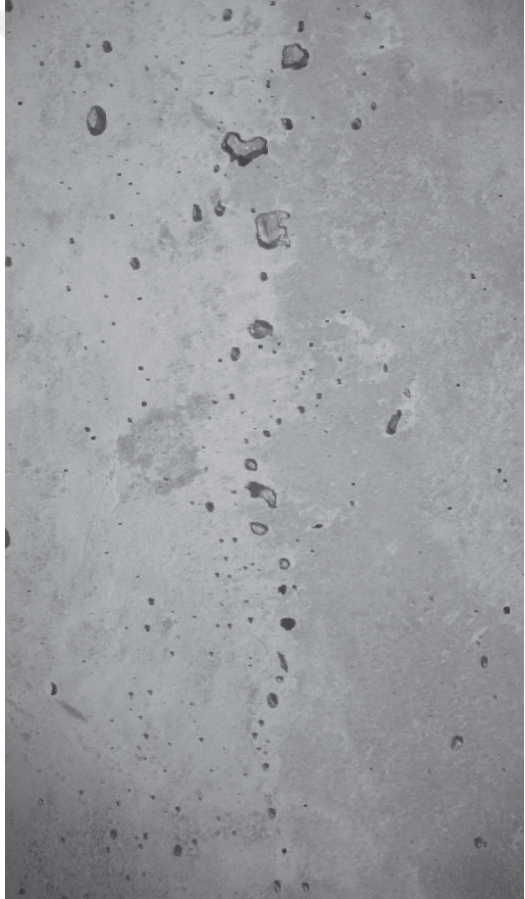

				
D1LO45				
Slice	Count	Total Area (pixel ²)	Average Size (pixel)	%Area
D1LO45.JP EG	123	229179	1863.244	1.522

Table A.2. Images and results for D1LO90

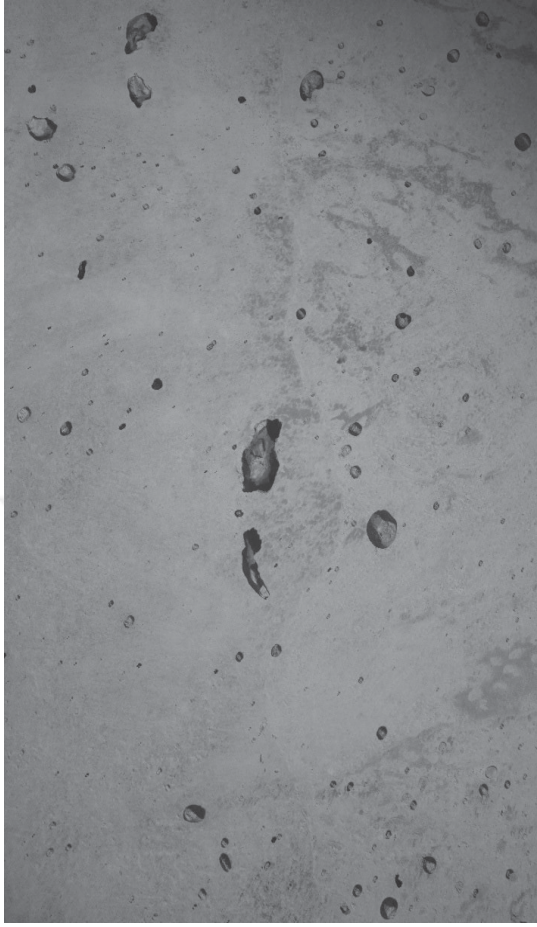

				
D1LO90				
Slice	Count	Total Area (pixel ²)	Average Size (pixel)	%Area
D1LO90.jpg	571	376003	658.499	2.498

Table A.3. Images and results of D2HI45

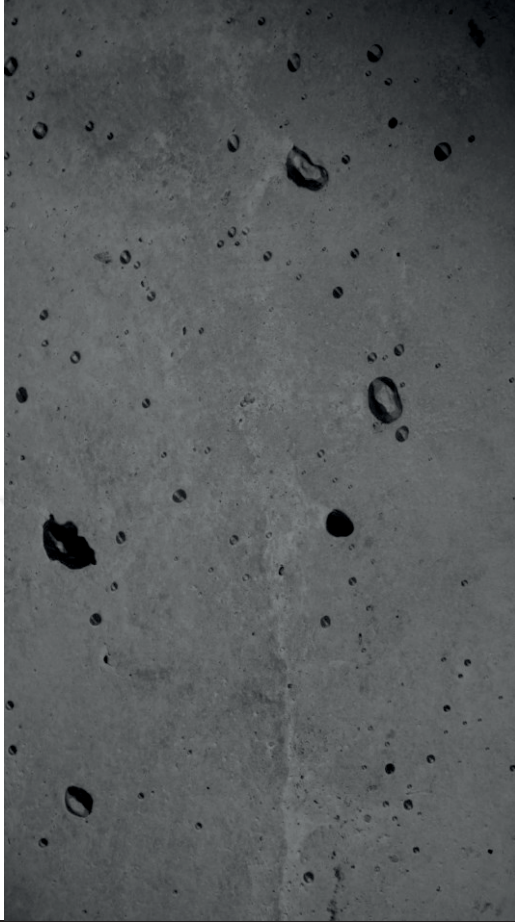
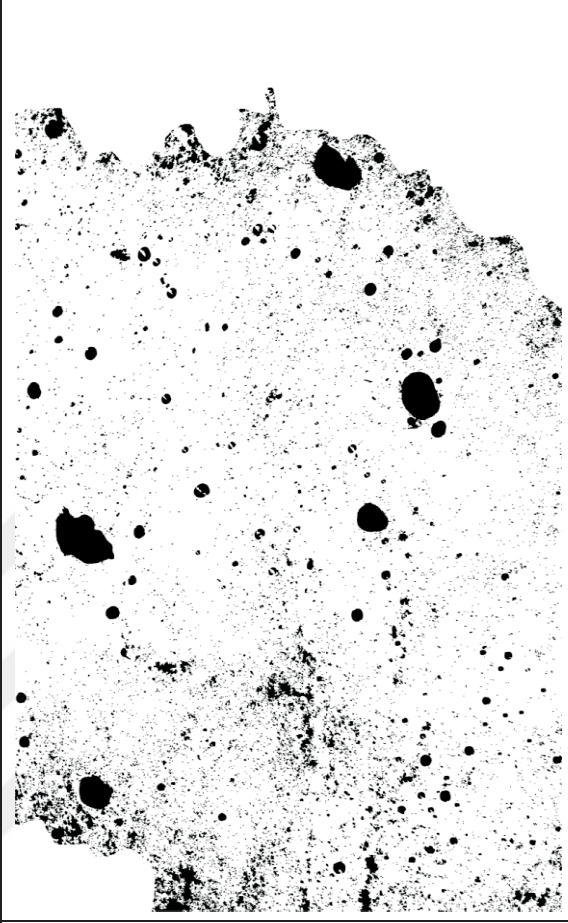
				
D2HI45				
Slice	Count	Total Area (pixel ²)	Average Size (pixel)	%Area
D2HI45.jpg	550	21991	399.836	2.291

Table A.4. Images and results of D2LO45

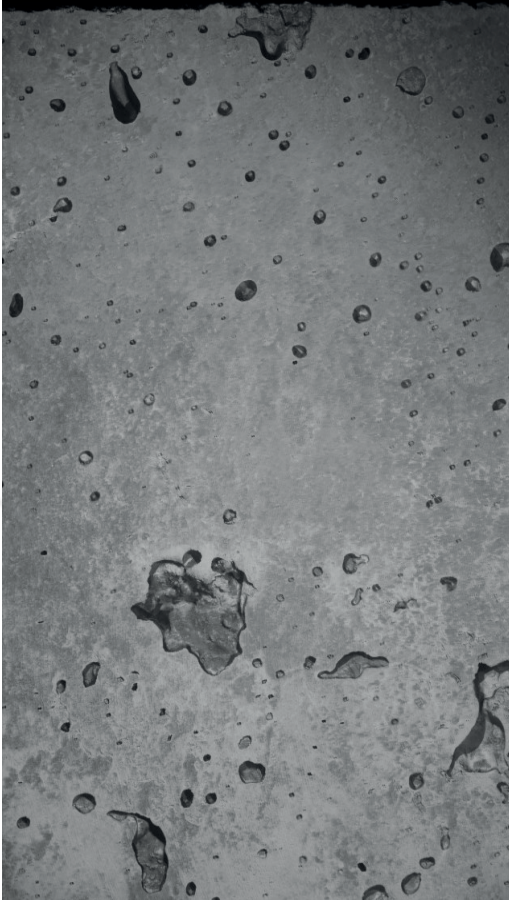
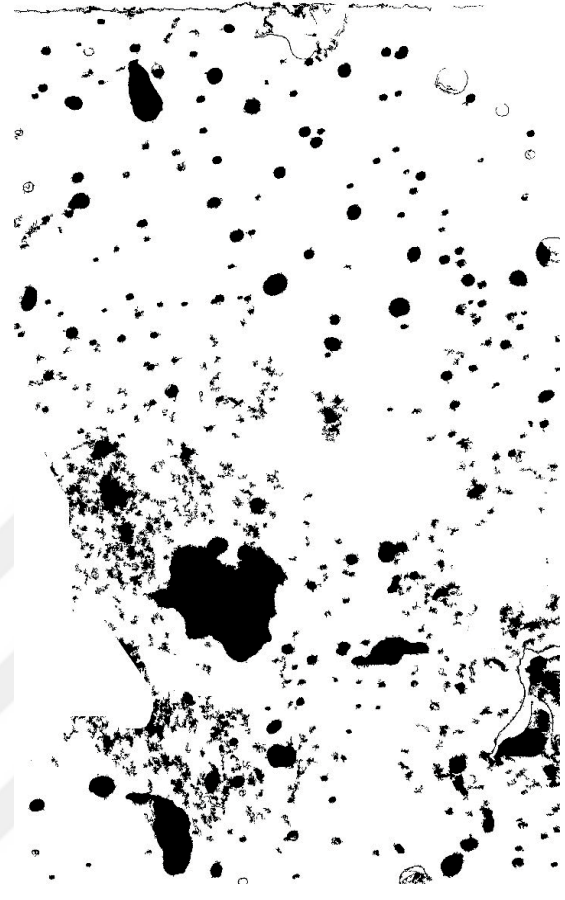
				
D2LO45				
Slice	Count	Total Area (pixel ²)	Average Size (pixel)	%Area
D2LO45.jpg	764	363497	475.78	2.415

Table A.5. Images and results of D2MID90

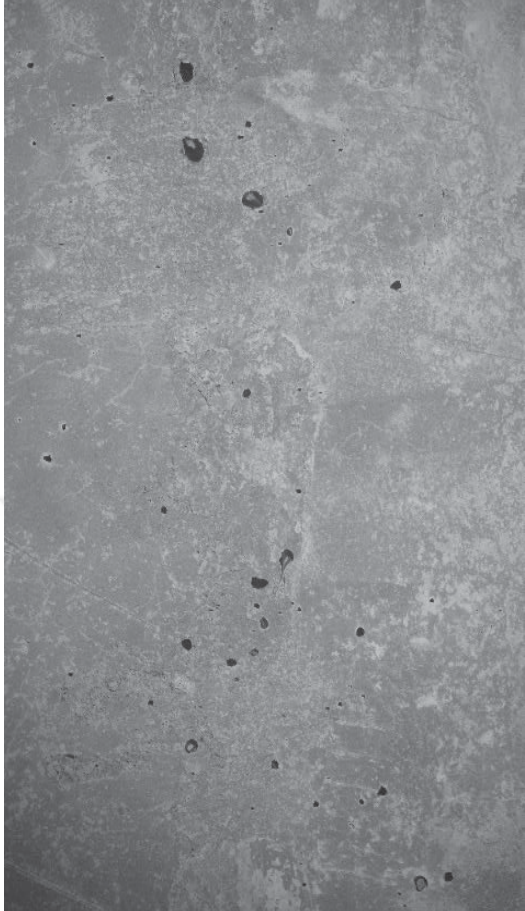

				
D2MID90				
Slice	Count	Total Area (pixel ²)	Average Size (pixel)	%Area
D2MID90.jpg	195	116372	596.779	0.773

Table A.6. Images and results of D3LO45

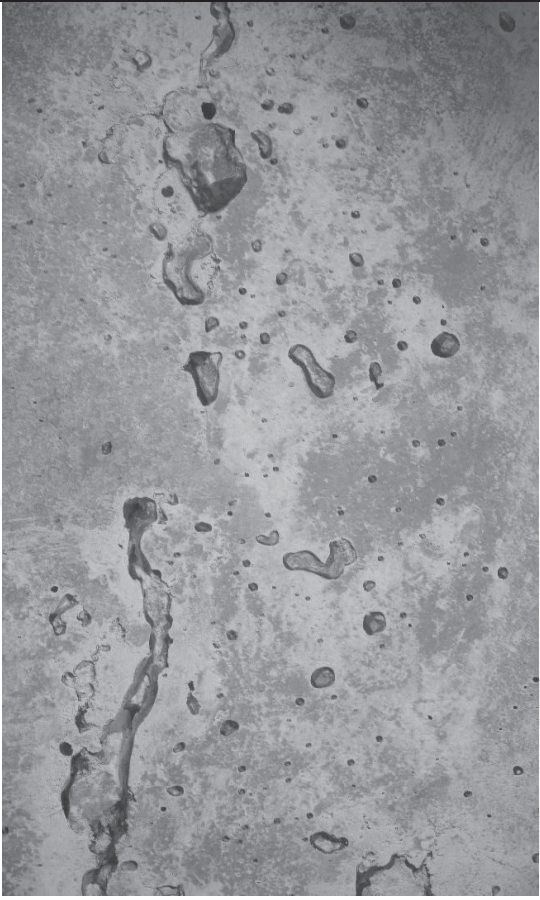

				
Slice	Count	Total Area (pixel ²)	Average Size (pixel)	%Area
D3LO45.jpg	140	262855	1712.975	1.746

Table A.6. Images and results of D3MID45

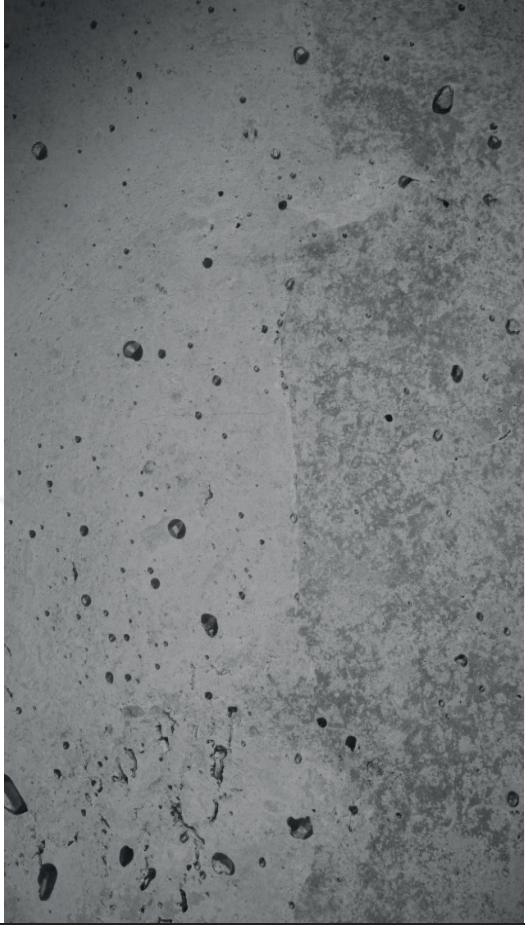
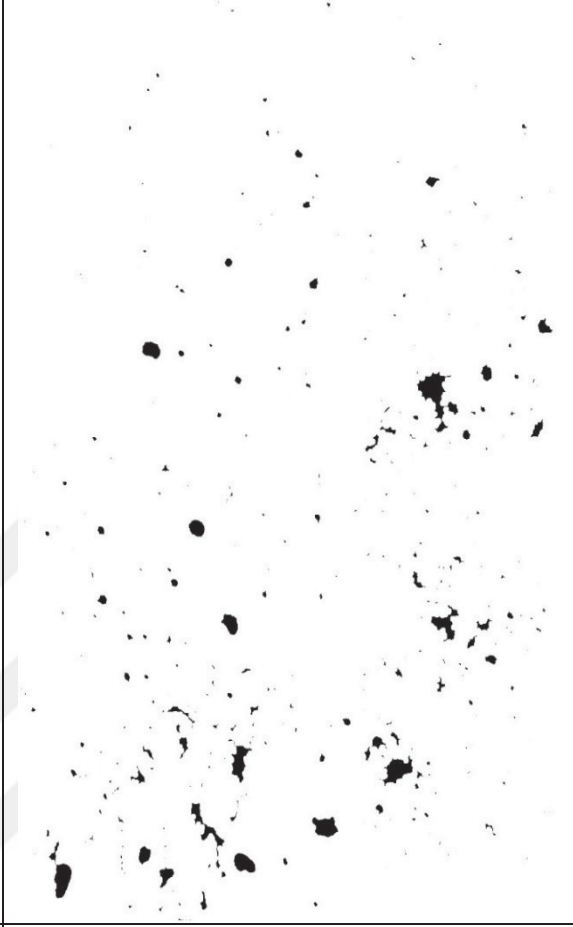
				
D3MID45				
Slice	Count	Total Area (pixel ²)	Average Size (pixel)	%Area
D3MID45.jpg	256	185051	1250.345	1.229

Table A.7. Images and results of D3MID90

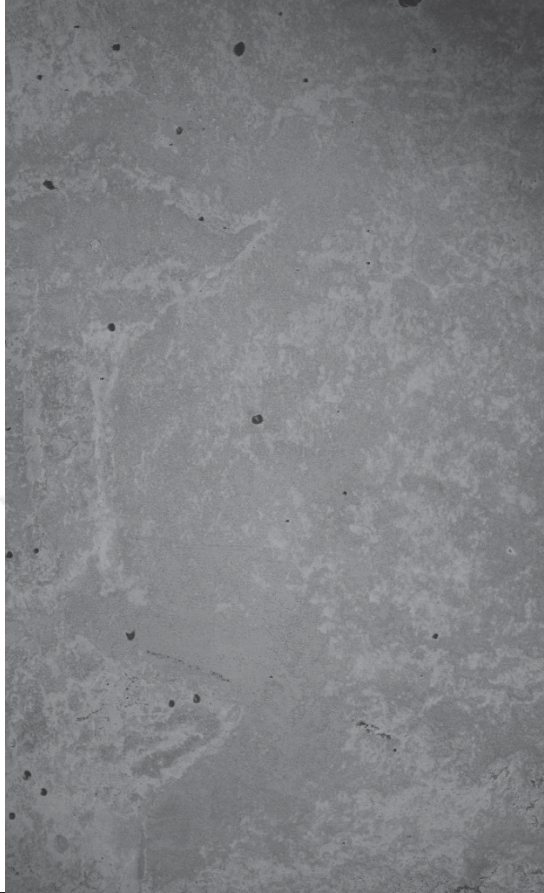
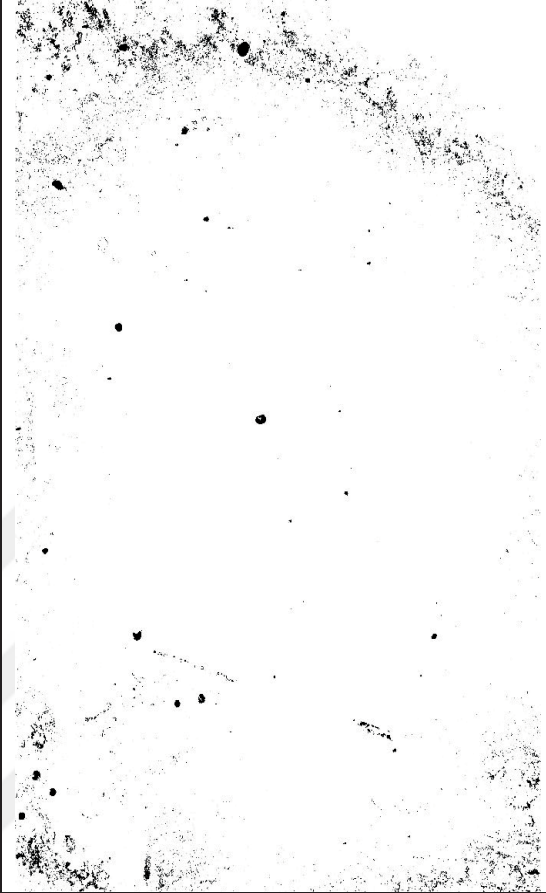
				
D3MID90				
Slice	Count	Total Area (pixel ²)	Average Size (pixel)	%Area
D3MID90.jpg	197	60235	305.761	0.4

Table A.8. Images and results of D4HI90



				
D4HI90				
Slice	Count	Total Area (pixel ²)	Average Size (pixel)	%Area
D4HI90.jpg	273	78965	289.2	0.525

Table A.8. Images and results of D5LO90

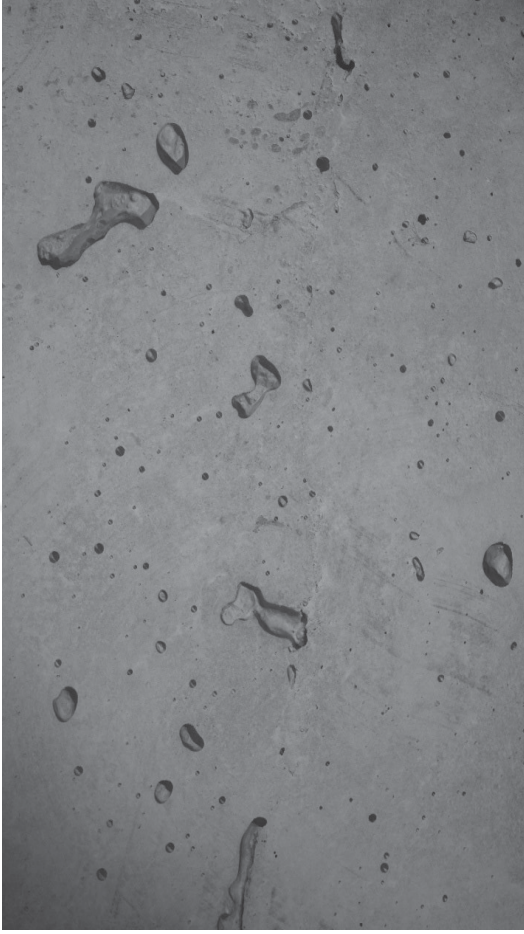

				
D5LO90				
Slice	Count	Total Area (pixel ²)	Average Size (pixel)	%Area
D5LO90.jpg	661	572879	866.685	3.805

Table A.9. Images and results of D5MID45

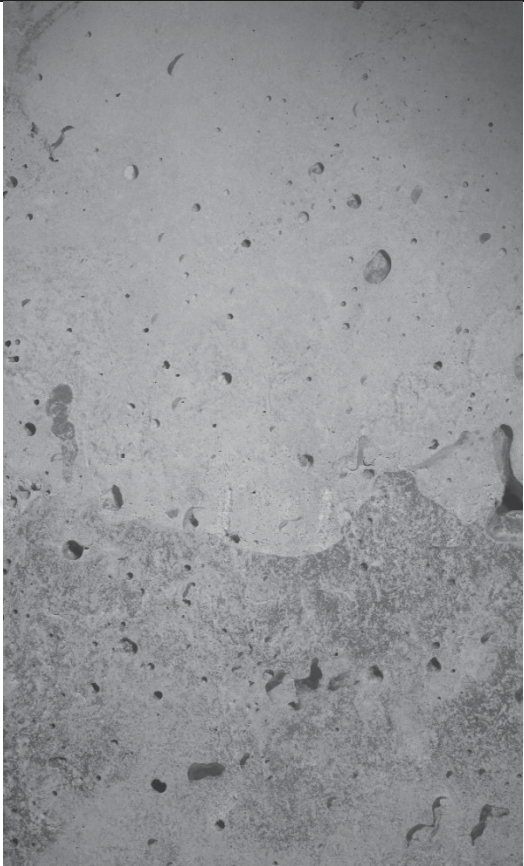

					
D5MID45					
Slice	Count	Total Area (pixel ²)	Average Size (pixel)	%Area	Slice
D5MID45.jpg	331	184208	556.52	1.224	99.889

Table A.10. Images and results of D5MID90

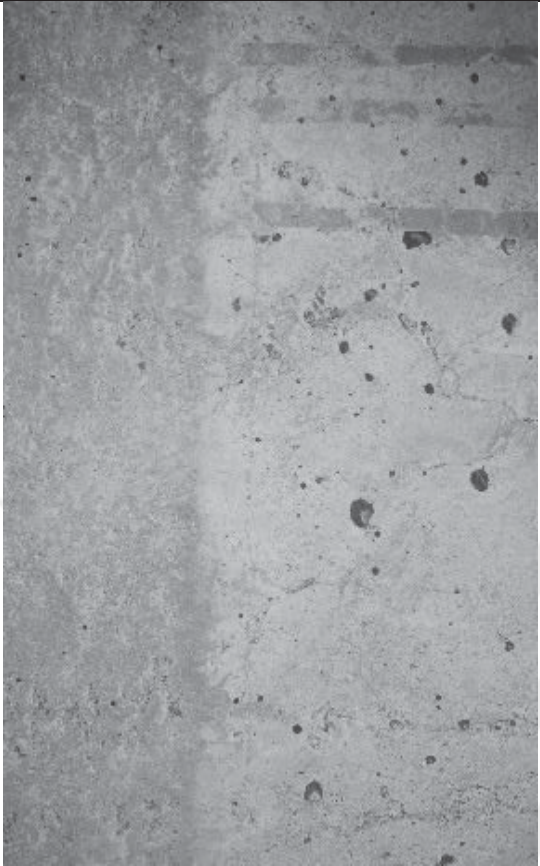

				
D5MID90				
Slice	Count	Total Area (pixel ²)	Average Size (pixel)	%Area
D5MID90.jpg	157	137896	878.318	0.916

Table A.11. Images and results of D4LO45

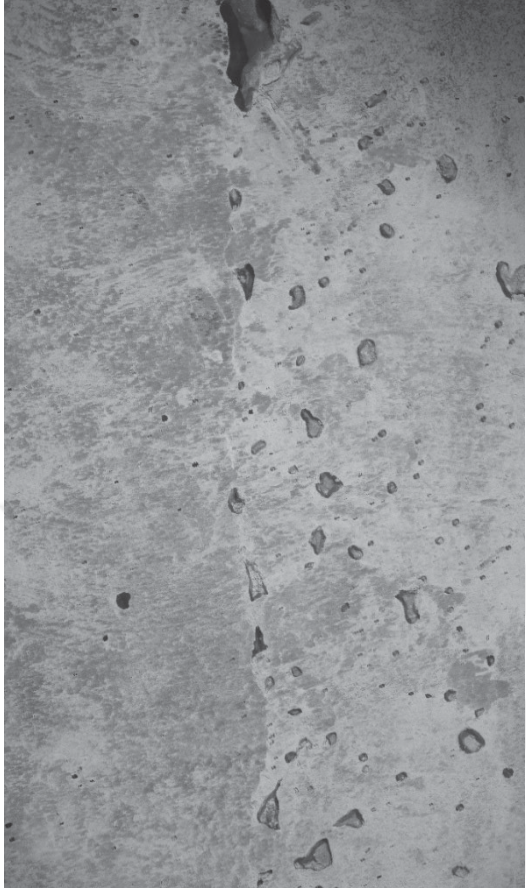

				
D4LO45				
Slice	Count	Total Area (pixel ²)	Average Size (pixel)	%Area
D4LO45.jpg	744	533870	717.567	3.546

Table A.11. Images and results of MONOHI

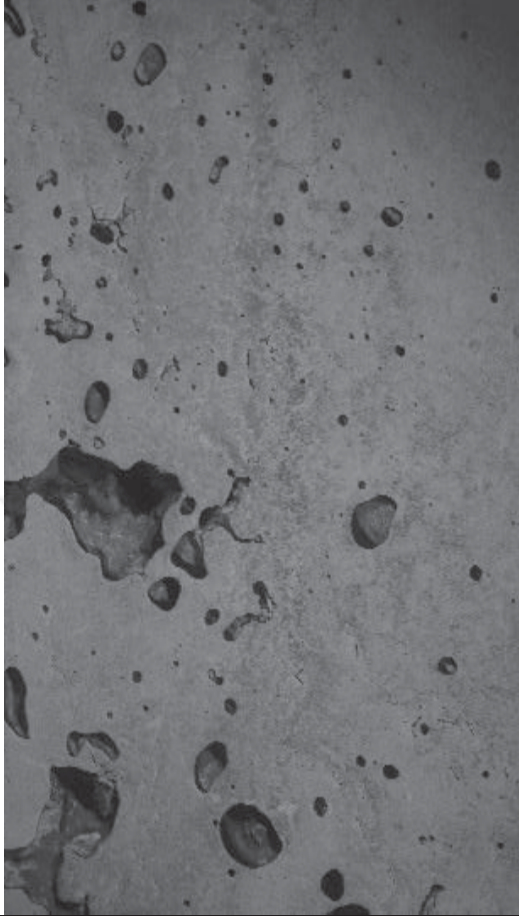

				
MONOHI				
Slice	Count	Total Area (pixel ²)	Average Size (pixel)	%Area
MONOHI.jpg	181	1139069	6293.199	7.566

Table A.12. Images and results of D5MID90

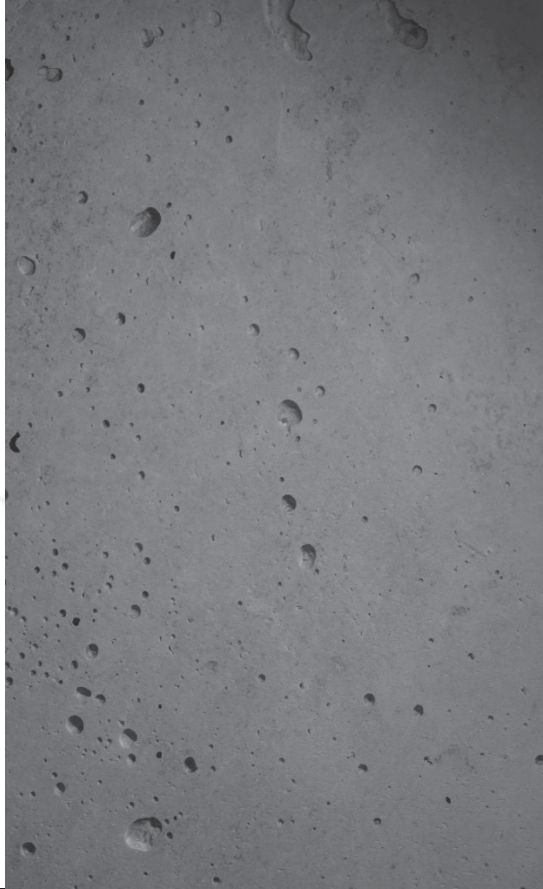
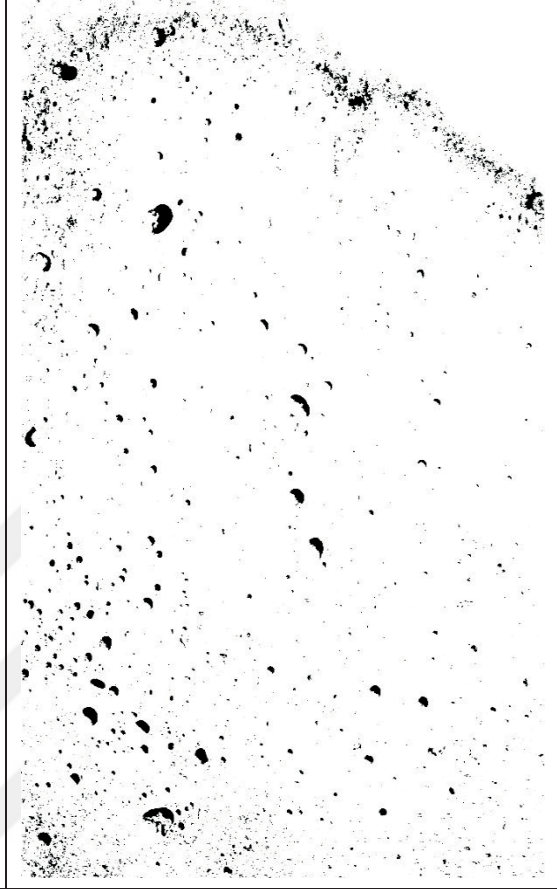
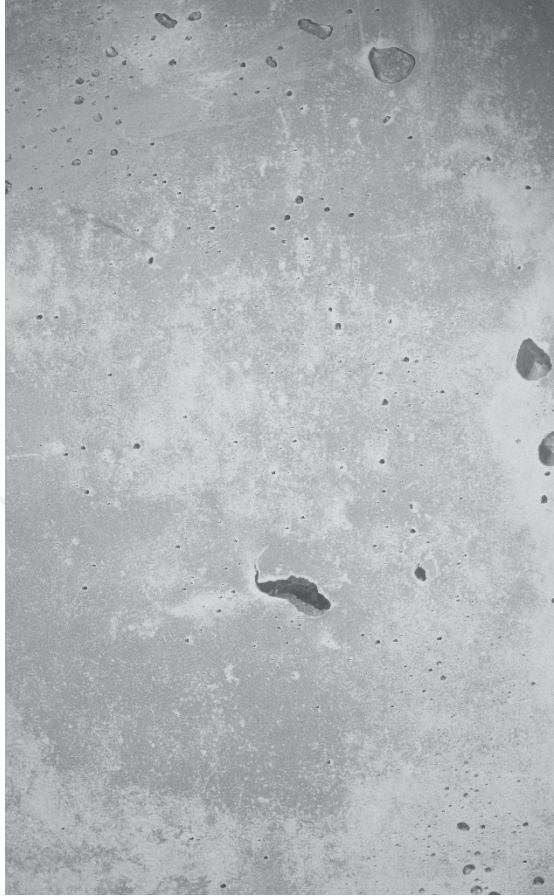
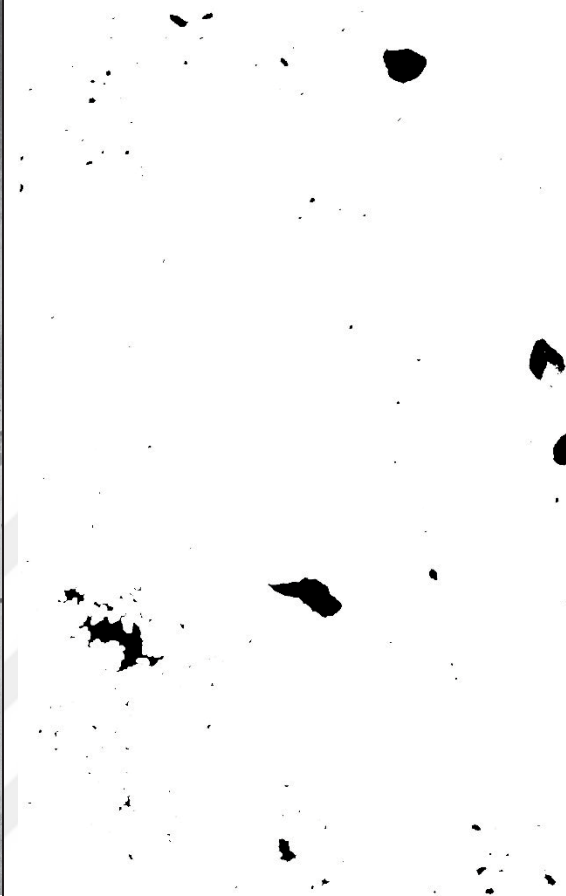
				
MONOMID				
Slice	Count	Total Area (pixel ²)	Average Size (pixel)	%Area
MONOMID.jpg	528	226808	429.561	1.507

Table A.13. Images and results of MONOLO

				
MONOLO				
Slice	Count	Total Area (pixel ²)	Average Size (pixel)	%Area
MONOLO.jpg	154	151315	982	1.005

APPENDIX B

2D Image analysis results are given

Table B.1 2D image analysis results

Surface name	Average area of all voids (pixel ²)	Area fraction	Total void area (pixel ²)	Average of 10 largest void (pixel)
d1hi451	1898.95	0.034	476637	33282.5
d1hi452	608.41	0.012	168530	7948.4
d1hi453	835.91	0.023	327678	18063.3
d1hi454	505.33	0.008	108647	7122
d1hi455	1712.55	0.028	385323	33695.2
d1hi456	1169.06	0.021	298110	26224.7
d1hi901	1200.73	0.036	504305	34632.2
d1hi902	1736.10	0.033	456593	37258.6
d1hi903	2176.58	0.049	679094	59552.5
d1hi904	1951.87	0.030	423556	36041
d1hi905	1398.69	0.032	448981	29152.7
d1hi906	1257.98	0.022	305688	24463
d1lo451	1741.29	0.041	569403	39521.2
d1lo452	1037.40	0.016	230302	17202.3
d1lo453	634.48	0.016	219530	13021.3
d1lo454	2038.44	0.044	609494	45044.3
d1lo455	2409.85	0.050	701267	52492.6
d1lo456	1667.82	0.030	425295	31064.7
d1lo901	4086.41	0.074	1033862	72146.8
d1lo902	1144.70	0.028	398354	30820.5
d1lo903	1117.67	0.027	373302	21812.7
d1lo904	1358.19	0.025	344980	21342.9
d1lo905	2746.72	0.049	689427	62592.3
d1mid451	2137.32	0.044	617685	52638.9
d1mid452	1838.79	0.024	332821	27655.8

Table B.2 2D image analysis results

Surface name	Average area of all voids (pixel ²)	Area fraction	Total void area (pixel ²)	Average of 10 largest void (pixel)
d2mid453	2024.75	0.045	629696	51449.8
d2mid454	2718.07	0.052	725725	55389.9
d2mid455	2277.22	0.063	881286	76918.5
d2mid456	460.21	0.014	194669	9006.9
d2mid901	9930.3	0.165	2303830	223923.3
d2mid902	1827.33	0.055	772959	58255.9
d2mid903	2773.76	0.056	787748	69390.6
d2mid904	1492.88	0.037	513549	39275.2
d2mid905	1539.58	0.035	492664	32728.5
d2mid906	655.07	0.012	174905	10127.5
d3hi451	1469.97	0.024	336622	27800.8
d3hi452	992.96	0.023	324698	15955.9
d3hi453	1451.23	0.044	613869	43798.7
d3hi454	1449.38	0.032	446409	24344.1
d3hi455	1279.62	0.03	424835	35681.7
d3hi456	3114.5	0.051	716335	66053
d3hi901	2764.79	0.063	881968	66929.3
d3hi902	1469.97	0.024	336622	27800.8
d3hi903	1882.92	0.057	796477	56582.5
d3hi904	1615.92	0.032	442762	35701.6
d3hi905	2545.63	0.049	682229	58306.4
d3hi906	1347.52	0.035	485108	29311.4
d3lo451	8614.19	0.162	2265532	218320.6
d3lo452	2618.14	0.047	662389	50203.7
d3lo453	2100.36	0.051	720423	53019.2

Table B.3 2D image analysis results

Surface name	Average area of all voids (pixel ²)	Area fraction	Total void area (pixel ²)	Average of 10 largest void (pixel)
d3lo454	4668.69	0.079	1111149	100955.1
d3lo455	2855.07	0.059	825115	62883.1
d3lo456	1331.78	0.031	428832	30559.9
d3lo901	3264.72	0.064	897797	77092.1
d3lo902	972.61	0.023	318043	18118.2
d3lo903	4234.03	0.069	969592	81149.2
d3lo904	3516.83	0.056	784254	65235.1
d3lo905	3792.4	0.065	906383	82831.7
d3lo906	1266.18	0.035	484948	39828.9
d3mid451	2134.6	0.038	529380	43792.7
d3mid452	904.58	0.027	382638	23981.3
d3mid453	1927.3	0.03	418225	29892.7
d3mid454	1413.11	0.037	512959	35852.5
d3mid455	7183.52	0.093	1300218	127523.1
d3mid456	1052.65	0.032	445271	25751.9
d3mid901	1740.31	0.027	379388	29125.9
d3mid902	6438.62	0.082	1146075	112020.3
d3mid903	2355.19	0.038	532274	40921.9
d3mid904	2355.19	0.038	532274	40921.9
d3mid905	1475.55	0.042	594647	44470.6
d3mid906	998.46	0.024	335482	21237.6
d4hi451	1120.62	0.022	309290	17229.9
d4hi452	456.91	0.01	144839	7579
d4hi453	6112.56	0.092	1289751	119703.2
d4hi454	714.76	0.014	199418	9371.7

Table B.4 2D image analysis results

Surface name	Average area of all voids (pixel ²)	Area fraction	Total void area (pixel ²)	Average of 10 largest void (pixel)
d4hi455	1086.52	0.016	227083	14722.3
d4hi456	907.34	0.014	195985	10263.8
d4hi901	476.83	0.005	73432	3822.7
d4hi902	2917.86	0.039	551475	50046.8
d4hi903	2113.04	0.032	452191	38161.4
d4hi904	470.25	0.006	89817	4014.1
d4hi905	1342.58	0.041	567910	32759.2
d4hi906	985.82	0.026	358838	18170.6
d4lo901	872.13	0.019	261638	14676.3
d4lo902	2179.84	0.033	455587	37718.1
d4lo903	2194.65	0.031	434541	34504.6
d4lo904	1929.51	0.027	378184	30035.1
d4lo905	1176.43	0.023	325870	18377.3
d4lo906	992.26	0.017	236159	16224.2
d4lo451	1336.85	0.04	565489	42677.2
d4lo452	3398.2	0.069	971884	72383
d4lo453	3345.29	0.067	943373	87880.5
d4lo454	1727.12	0.03	414508	36336.3
d4lo455	1894.62	0.039	547544	41143.8
d4lo456	980.89	0.03	414918	25319.3
d4mid451	1309.02	0.026	361290	27780
d4mid452	1960.12	0.04	566476	39307.8
d4mid453	1055.52	0.019	272323	21289
d4mid454	1870.32	0.037	516207	32350.6
d4mid455	1492.19	0.043	608815	40812.3

Table B.5 2D image analysis results

Surface name	Average area of all voids (pixel ²)	Area fraction	Total void area (pixel ²)	Average of 10 largest void (pixel)
d4mid901	1135.67	0.019	272560	19799.2
d4mid902	1942.1	0.059	821508	53375
d4mid903	2553.78	0.049	689521	62207
d4mid904	2291.1	0.046	646091	57586.4
d4mid905	1365.46	0.041	577588	32466.3
d4mid906	6173.4	0.108	1512483	146322.7
d5hi451	1407.28	0.033	458773	23354.9
d5hi452	1790.95	0.034	481766	41271.6
d5hi453	1492.3	0.04	553642	37640.6
d5hi454	3526.9	0.046	641896	48647.6
d5hi455	1831.47	0.038	527463	41227.3
d5hi456	2639.05	0.058	818106	68847.9
d5hi901	483.2	0.01	142061	8366.8
d5hi902	533.96	0.01	140431	8963.9
d5hi903	1316.18	0.023	327728	17684.8
d5hi904	787.92	0.011	159948	9128
d5hi905	1434.31	0.025	355709	24202.4
d5hi906	3507.54	0.064	890916	75341.1
d5hi907	1374.18	0.032	446610	33413.8
d5hi908	533.96	0.01	140431	8963.9
d5hi909	785.34	0.009	124869	8456.6
d5hi910	654.45	0.012	161650	10406.7
d5hi911	2785.76	0.07	986159	85707.8
d5hi9012	1625.83	0.03	416213	33025.7
d5hi9013	675.27	0.011	149911	8660.3

Table B.6 2D image analysis results

Surface name	Average area of all voids (pixel ²)	Area fraction	Total void area (pixel ²)	Average of 10 largest void (pixel)
d5hi9017	1555.57	0.028	395115	32424
d5lo451	3007.73	0.049	679746	57069.9
d5lo452	2997.24	0.058	812253	72507.4
d5lo453	9948.11	0.143	1999570	196518.5
d5lo454	2710.22	0.056	777832	68025.5
d5lo455	457.92	0.01	138749	10237.5
d5lo456	2482.61	0.049	682719	46813.7
d5lo457	574.96	0.017	242060	12650.2
d5lo458	1899.53	0.046	638242	54796.6
d5lo901	1387.32	0.029	410648	29762
d5lo902	1439.83	0.023	328281	25510.7
d5lo903	1891.16	0.031	438749	32128
d5lo904	2823.35	0.052	728424	59052.5
d5lo905	617.65	0.015	207532	11635.9
d5lo906	1825.7	0.033	463729	36596.9
d5lo907	1655.76	0.04	566271	44705.5
d5lo908	1770.54	0.034	474506	34547
d5lo909	1474.72	0.031	436518	33920
d5lo9010	1366.26	0.03	422174	28215.5
d5lo9011	1814.99	0.04	555387	42140.5
d5lo9012	1005.41	0.026	364964	24519.3
d5mid451	3753.81	0.079	1111128	90537.4
d5mid452	2706.36	0.061	860622	70372.1
d5mid453	2302.29	0.057	798893	59878.4
d5mid454	1200.19	0.036	507681	27228.8

Table B.7 2D image analysis results

Surface name	Average area of all voids (pixel ²)	Area fraction	Total void area (pixel ²)	Average of 10 largest void (pixel)
d5mid455	13032.37	0.186	2606474	257353
d5mid456	2925.83	0.08	1123518	100552.9
d5mid457	10600.1	0.187	2618225	255164
d5mid458	4810.67	0.104	1452821	127348.4
d5mid459	4361.75	0.071	990118	94512.4
d5mid901	1406.95	0.032	450223	36475.7
d5mid902	852.6	0.016	223382	18451.8
d5mid903	2389.05	0.067	938897	68000.9
d5mid904	1063.68	0.02	278683	20212.5
d5mid905	890.29	0.025	348102	21029
d5mid906	1078.2	0.03	423733	29969.1
d5mid907	1478.28	0.03	416875	31772.9
d5mid908	668.71	0.018	248091	14405.8
dbhi451	1073.23	0.022	314457	20277.2
dbhi452	1069	0.03	424392	29631.3
dbhi453	1596.11	0.042	584178	37036.4
dbhi454	1949.79	0.032	446502	34714
dbhi455	3217.45	0.037	514792	46074.8
dbhi456	1073.23	0.022	314457	20277.2
dbhi457	898.07	0.025	345756	17424
dbhi901	1244.29	0.025	345914	26519.5
dbhi902	1589.65	0.045	631091	41900.2
dbhi903	4296.42	0.079	1099884	102555.2
dbhi904	2902.37	0.073	1027439	89453.5
dbhi905	1481.2	0.032	453248	30077

Table B.8 2D image analysis results

Surface name	Average area of all voids (pixel ²)	Area fraction	Total void area (pixel ²)	Average of 10 largest void (pixel)
dbhi906	1123.76	0.02	278693	17385.5
dblo451	1682.73	0.036	504818	36115.9
dblo452	1986.07	0.041	570002	44193.5
dblo453	2681.98	0.057	791185	53592.6
dblo454	3072.72	0.068	955615	76509.6
dblo455	999.5	0.028	391804	21765.6
dblo456	1340.48	0.039	548258	35555
dblo901	2503.04	0.055	775943	57092.1
dblo902	1311.36	0.035	486515	36291.2
dblo903	2171.37	0.051	707867	52366.6
dblo904	1184.98	0.031	439628	25633.4
dblo905	626.7	0.019	265096	15472.2
dblo906	1599.88	0.045	628751	45903.6
dbmid451	937.44	0.027	379662	19113.4
dbmid452	3497.27	0.062	870821	70804.2
dbmid453	1932.7	0.043	603002	44977.5
dbmid454	1138.52	0.023	316508	25100.3
dbmid455	5327.12	0.035	1193275	107978.7
dbmid456	4155.26	0.034	1042970	93399.2
dbmid901	6430.73	0.075	1048209	99497.4
dbhi906	1123.76	0.02	278693	17385.5
dblo451	1682.73	0.036	504818	36115.9
dblo452	1986.07	0.041	570002	44193.5
dblo453	2681.98	0.057	791185	53592.6
dblo454	3072.72	0.068	955615	76509.6

APPENDIX C

3D surface depth map examples are given in this section. Dimensions are in pixel and depth bar on the right shows the depth in mm.

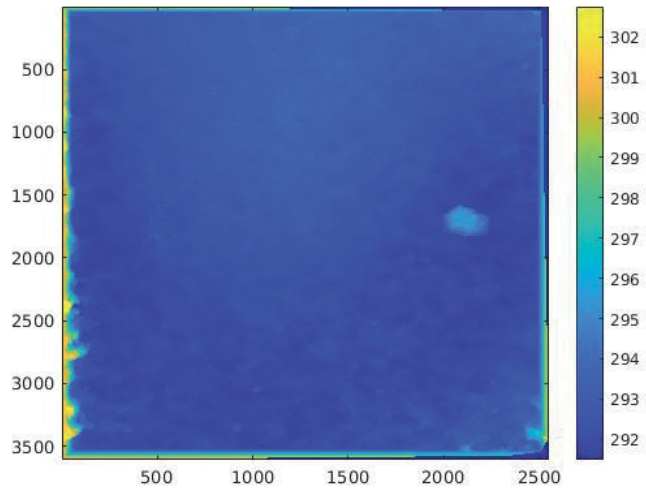


Figure C.1. D1HI45 Depth map

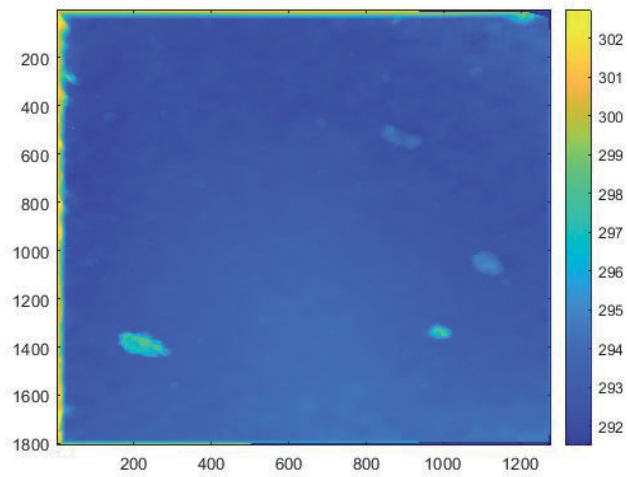


Figure C.2. D1LO90 Depth map

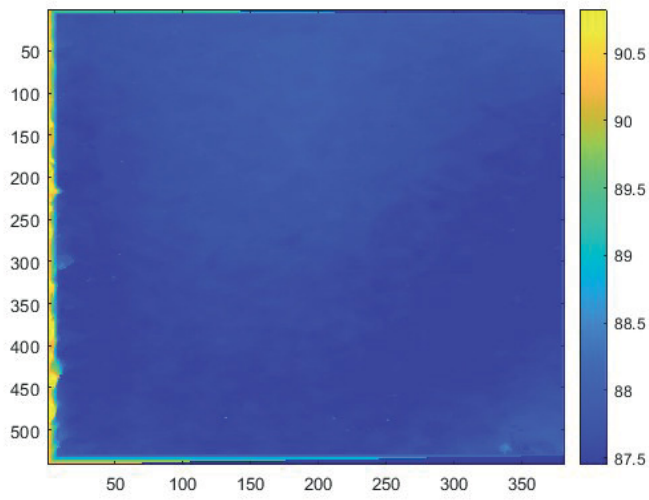


Figure C.3. D2MID90 Depth map

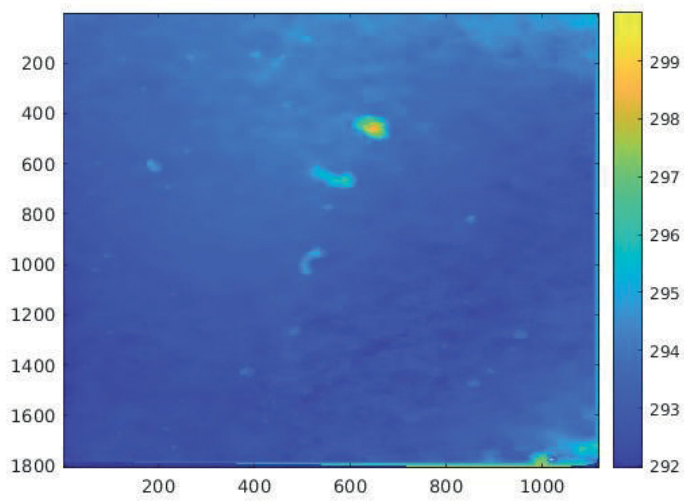


Figure C.4. D2MID45 Depth map

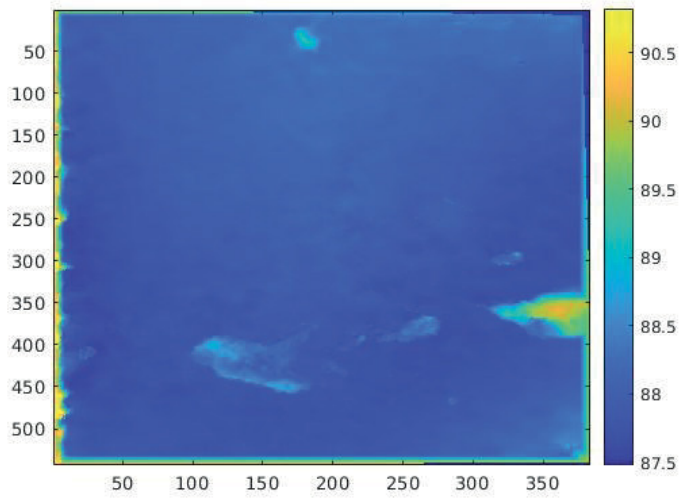


Figure C.5. D3MID90 Depth map

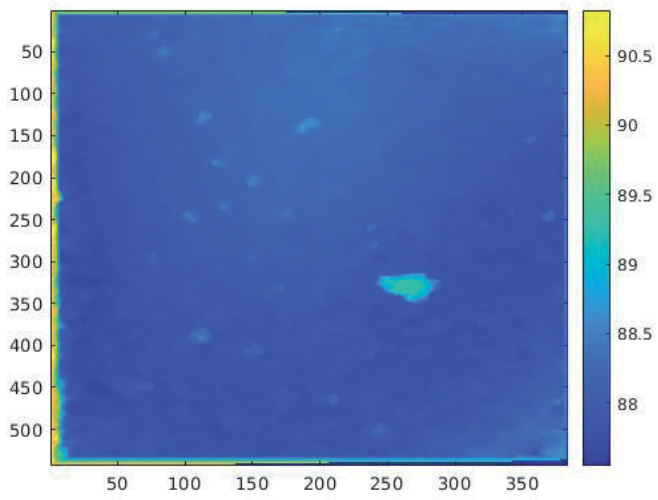


Figure C.6. D4HI45 Depth map

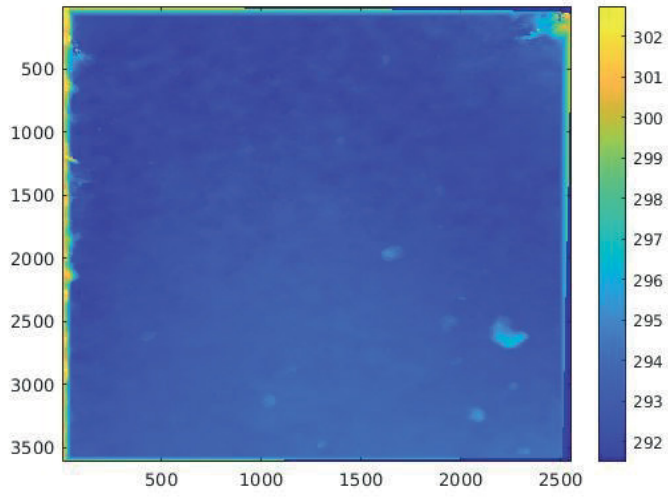


Figure C.7. D5LO90 Depth map

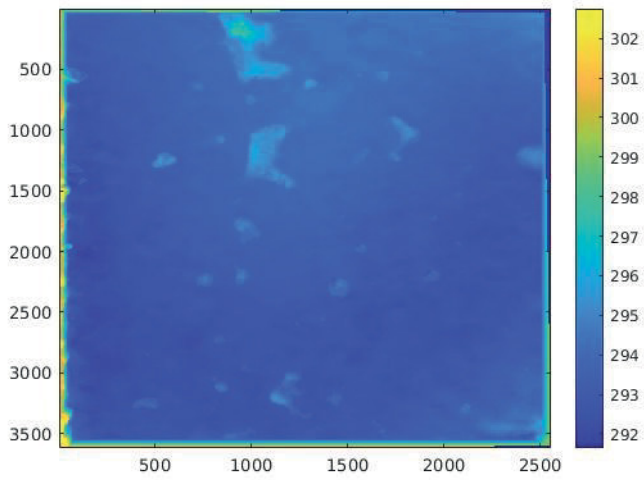


Figure C.8. D5HI45 Depth Map

APPENDIX D

Specimens were tested according to the Slant Shear test method.



Figure D.1. SSMONOMID



Figure D.2. SSMID90



Figure D.3. SSMONOHI



Figure D.4. SSMID45



Figure D.5. SSMONOLO



Figure D.6. SSHI45



APPENDIX E

Specimens were tested according to the Bi-surface Shear test method



Figure E.1 DBMID45



Figure E.2 DBLO90



Figure E.3 DBHI45



Figure E.4 DBHI90

APPENDIX F

Specimens were tested according to Pull-off test method



Figure F.1 KMONOLO3



Figure F.2 KMONOLO4



Figure F.3 KMONOLO6



Figure F.4 KMONOLO7



Figure F.5 KMID901



Figure F.6 KMID909



Figure F.7. KHI9013



Figure F.8. KHI9014



Figure F.9 KLO45



Figure F.10 KLO45



Figure F.11 KHI4520



Figure F.12 KLO4522



Figure F.13 KMID45



Figure F.14 KLO9024



Figure F.15 KLO90



Figure F.16 MONOLO27



Figure F.17 KHI90



Figure F.18 KMID90



VITA

Date and Place of Birth: 1986, İzmir/TURKEY

Education

PhD., Civil Engineering Department | İzmir Institute of Technology, 2020, Thesis Title: “Examination of Bonding Between Successive Lifts of Concretes Having Different Thixotropy Levels by Surface Scanning “

M.Sc. Civil Engineering Department | İzmir Institute of Technology, 2013, Thesis Title: “Effects of Thixotropy on Self-Consolidating Concrete Surface Properties”

B.Sc. Civil Engineering Department | Celal Bayar University, 2009.

Work Experience

Researcher | 109M615 coded Tubitak project | 2010-2012

Research Assistant | İzmir Institute of Technology, Civil Engineering Department | 2012-2020

Publications

Effects of Thixotropy Formwork Type and Release Agent on Self-Consolidating Concrete Surface Defects ACE 2016 Boğaziçi University, İstanbul Turkey, [First author]

Değişik Kompozisyonlarda Üretilen Kendiliğinden Yerleşen Betonların Reolojik ve Tiksotropik Özelliklerinin Belirlenmesi 8. Ulusal Beton Kongresi İzmir 2011, [Third author]

Determination of Rheological Parameters and Thixotropic Properties of Fresh SCC Mixtures with Varying Compositions 9th International Congress on Civil Engineering · Isfahan, Iran 2012, [Third author]

Effects of Fly Ash Aggregate on the Rheology and Compressive Strength of Self-Consolidating Concrete ACE 2018 Ege University, İzmir Turkey, [Third author]

Projects

109M615 coded Tubitak project | 2010-2012

ERASMUS IP Archaeological Landscapes Erythrai/Ildırı: Archaeological Landscapes: Preservation, Design, Use 2013 İzmir

BAP project, Effects of Fly Ash Aggregate on the Rheology and Compressive Strength of Self-Consolidating Concrete, 2018 İzmir

E.U. Project: UIP-2017-05-7113 J.J. “Development of Reinforcement Concrete Elements and Systems with Waste Tire Powder”- ReCoTiP Josip Juraj Strossmayer University Of Osijek / Croatia (2019, Spring semester)